

# X-ray photoelectron spectroscopy of size selected copper clusters on silicon

vorgelegt von  
Diplom-Physikerin  
Nicoletta Ferretti  
aus Ravenna

von der Fakultät II - Mathematik und Naturwissenschaften  
der Technischen Universität Berlin  
zur Erlangung des akademischen Grades  
Doktor der Naturwissenschaften  
Dr.rer.nat.

**genehmigte** Dissertation

Promotionsausschuss:

Vorsitzender: Prof. Dr. rer. nat. M. Dähne  
Berichter/Gutachter: Prof. Dr. rer. nat. Dr. h.c. W. Eberhardt  
Berichter/Gutachter: Prof. Dr. rer. nat. T. Möller

Tag der wissenschaftlichen Aussprache: 15.12.2008

Berlin 2009  
D 83



# Contents

<b>1</b>	<b>Introduction</b>	<b>1</b>
<b>2</b>	<b>Metal clusters</b>	<b>3</b>
2.1	Electronic structure: the Jellium model . . . . .	3
2.2	Metal to insulator transition . . . . .	5
2.3	1/R behaviour and liquid drop model . . . . .	6
2.4	Deposited clusters and cluster diffusion . . . . .	8
2.5	Soft landing . . . . .	10
2.6	Copper cluster: electronic structure and geometry . . . . .	10
2.7	X-ray absorption measurements on copper . . . . .	12
<b>3</b>	<b>X-ray spectroscopy techniques</b>	<b>15</b>
3.1	X-ray spectroscopy on clusters . . . . .	15
3.2	XPS . . . . .	16
3.2.1	XPS principle . . . . .	17
3.3	XANES . . . . .	20
3.4	Auger . . . . .	23
<b>4</b>	<b>Experimental apparatus</b>	<b>25</b>
4.1	Cluster deposition . . . . .	25
4.1.1	Vacuum system . . . . .	25
4.1.2	Cluster production . . . . .	26
4.1.3	Mass selection . . . . .	31
4.1.4	Ion optic system . . . . .	32
4.1.5	Cu cluster deposition . . . . .	34
4.1.6	Defined cluster size optimisation . . . . .	35
4.1.7	UHV suitcase . . . . .	37
4.2	Synchrotron radiation . . . . .	39
4.2.1	Beamline . . . . .	39
4.2.2	The experimental station SURICAT . . . . .	40

<b>5</b>	<b>Experimental results and discussion</b>	<b>45</b>
5.1	Introduction . . . . .	45
5.2	XPS . . . . .	45
5.2.1	Survey . . . . .	45
5.2.2	Silicon substrate . . . . .	47
5.2.3	Cu 2p . . . . .	48
5.2.4	Cu 3p . . . . .	53
5.2.5	Cu 3d . . . . .	54
5.2.6	Comparison of the levels and 1/R plot . . . . .	57
5.3	XANES . . . . .	63
5.3.1	XANES on deposited Cu clusters . . . . .	63
5.3.2	Band gap approximation . . . . .	72
5.4	Auger . . . . .	77
5.4.1	Auger parameter . . . . .	77
5.4.2	Initial and final state effects . . . . .	79
5.4.3	Hole-hole interaction in Auger final state . . . . .	81
<b>6</b>	<b>Summary and outlook</b>	<b>85</b>
	<b>Bibliography</b>	<b>87</b>
<b>A</b>	<b>List of publications</b>	<b>97</b>

# Chapter 1

## Introduction

The field of nanotechnology has been opened by Richard Feynman in 1959 with a lecture in which he predicted that *"when we have some control of the arrangement of things on a small scale we will get an enormously greater range of possible properties that substances can have"* [1]. In this sense clusters are extremely small nanoparticles which are strongly affected by quantum size effects. They are constituted of a number of atoms which can range from few to thousands (up to 1-2 nm). The study of clusters covers a fundamental role as these ultrasmall particles constitute a link between the atom and the macroscopic bulk. Experiments and calculations have shown that isolated clusters possess many interesting features, quite different from those known from surface and solid-state physics or from atomic and molecular physics. Of particular interest is the analysis of the development of the geometric and electronic structure as well as the chemical and physical properties as function of cluster size. For sizes smaller than 1-2 nm quantum size effects dominate the cluster properties. In this size range each atoms counts and an appropriate mass selection is absolutely necessary in order to achieve an exact understanding and control on the properties of the clusters. Small mass selected clusters have the potential to be used to functionalise ultimate small nanodevices, as for example in optoelectronic and semiconducting industry. Therefore clusters could change in a non predictable way today's nanotechnology which still operates in the scalable regime ( $\sim 100$  nm).

In particular metal clusters are of interest for their potential use as new semiconductors, in catalysis and to study the evolution of their magnetic properties with cluster size. Most has been learned from experiments on free, undisturbed clusters. However for any kind of application the clusters have to be brought into contact with an environment and thus the cluster-surface interaction becomes a major concern. Therefore, in this work the electronic structure of deposited metal clusters has been investigated as function of exact cluster size.

Methods for the production of supported clusters include aggregation by atom diffusion and self-organisation on surfaces [2–6]. However, soft landing of thermodynamical stable clusters from a molecular cluster beam on a solid surface is the most straightforward way for an exact control of the cluster size [7–12]. Technical challenges for low energy deposition of mass selected clusters from a cluster beam arise from the difficulty to accumulate a cluster density of  $\sim 1\%$  monolayer (i.e.  $10^{12} - 10^{13}$  clusters/cm<sup>2</sup>). In the frame of this thesis an experimental cluster apparatus has been updated and optimised in order to perform soft landing deposition of mass selected metal clusters with sufficient coverage density. To study the development of the electronic energy levels with cluster size and to elucidate the basic interaction between the deposited copper clusters and the silicon surface, the techniques of X-ray photoelectron spectroscopy, X-ray absorption and Auger spectroscopy have been combined.

Synchrotron radiation provides the most intense X-ray radiation with tunable and highly monochromatic energy. The possibility of varying the photon energy permit to probe any electronic level of interest with maximum intensity and to perform absorption spectroscopy studies. Of particular interest in this thesis is the evolution of the electronic core levels with cluster size. In fact, even if the wave function of core levels are highly localised, small changes induced by the local atomic environment become reflected in the core level spectra. Thus X-ray spectroscopy is a leading technique to investigate clusters in contact with a surface.

The Thesis is structured as follows: Chapter 2 introduces the main properties of metal clusters and describes the development of these properties with cluster size. Also, the behaviour of the clusters upon adsorption on the surface have been discussed. In Chapter 3 the basic concepts of the spectroscopic techniques such as XPS, XANES and AES have been elucidated. Chapter 4 illustrate the experimental apparatus for clusters production, mass selection and soft landing deposition. Beamline PM4 at the synchrotron light source BESSY in Berlin and the experimental station SURICAT for X-ray spectroscopy investigations have been also described. In Chapter 5 the photoelectron spectroscopy results have been analysed and interpreted. Chapter 6 summarises the results.

# Chapter 2

## Metal clusters

Metal clusters are of high current interest due to their potential use in nanotechnology. The cluster size is an important parameter for tuning properties such as magnetism, electrical conductivity and catalytic activity. In order to understand this behaviour the study of the evolution of the electronic structure with increasing cluster size is of fundamental and technological interest.

### 2.1 Electronic structure: the Jellium model

A discovery that gave strong impetus for the development of the field of metal clusters was reported in 1984 by Knight *et al.* [13] due to the observation of magic cluster size in the mass spectrum of sodium clusters, i.e. an enhanced intensity of clusters with a certain number of atoms. The presence of the magic cluster sizes has been successively explained by the Jellium model [14]. In this model a quantum mechanical treatment of the cluster gives rise to discrete electronic states and closed shell of particular stability. In the spherical Jellium model a metal cluster is modelled by a uniform charged sphere filled with an electron gas which is formed by the delocalised valence electrons. The Schrödinger equation is solved for an electron constrained to move within the cluster sphere under the influence of an attractive mean field potential formed by the ionic cores (spherical box). This leads to a discretized density of states, the so called electron shell structure [15]. With increasing cluster size these shells gets filled (see Fig. 2.1). Sizes for which the uppermost shell is completely filled are particularly stable and therefore these clusters are called "magic". As an additional electron has to occupy the next higher shell, these magic clusters exhibit a significant band gap in the DOS.

The valence electron structure of free mass selected clusters has been well

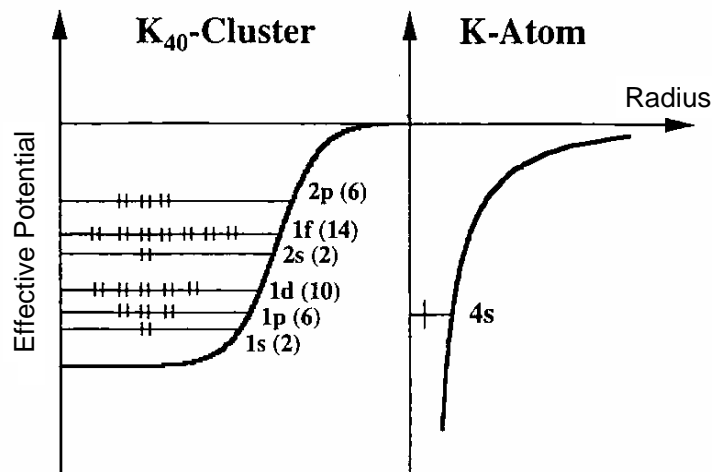


Figure 2.1: *Effective core potential and occupancy of the valence levels in a  $K_{40}$  cluster and in the  $K$  atom [16]. For  $K_{40}$  the potential in the Jellium model is rather flat when  $R$  converge to zero due to effective screening of the ionic core.*

documented by photoelectron spectroscopy with lasers in the work of K. J. Taylor *et al.* [17] on Cu, Ag and Au free clusters, C. -Y. Cha *et al.* [18] on free Cu clusters, J. Morenzin *et al.* [19] on Ni, Cu and Co clusters, O. Kostko *et al.* [20] on Na and Cu clusters, Kietzmann *et al.* [21] on free Nb clusters and G. Ganteför *et al.* [22] who studied the electronic structure of Ag, Cu, Na clusters. As the wavelength of lasers, however, is fairly restricted the inner valence shell and the core levels are not accessible by optical lasers but demands for UV and X-ray radiation as delivered by a synchrotron.

Approximating a metal cluster by a sphere is best justified for closed-shell clusters. From the Jahn-Teller theorem it follows that open-shell clusters must distort for potential energy lowering. This smears out the ideal shell structure in the density of states, causing a lift of the degeneration of the energy levels. Such effect can be described by deformable models, of which the simplest is the Clemenger-Nilsson model which allow spheroidal distortions, so that subshells are formed. This effect is evident in the even-odd alternation of the observed ionisation potential and electron affinity of simple metal clusters [14].

## 2.2 Metal to insulator transition

For clusters of metallic elements a main concern is at which cluster size metallic conductivity and metallic screening are observed. Metallic properties presuppose the existence of a partially occupied band with level spacing sufficiently small so that upon application of infinitely low static electrical fields electrical charges are conducted. This definition implies the existence of extended states at the Fermi energy ( $E_F$ ). However because of the finite size of clusters the energy levels are rather discrete and some band gap always exist at  $E_F$ .

Fröhlich [23] and Kubo [24] discussed the consequences of the band gap evolution when going from the solid matter to smaller and smaller particles.

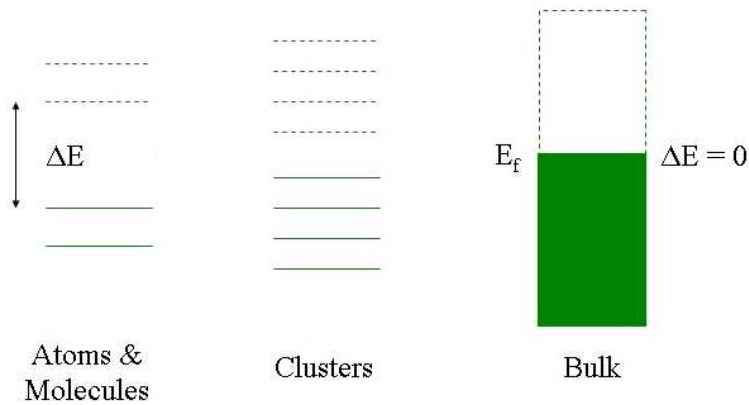


Figure 2.2: *Size dependent variation of the electronic energy levels. Full lines represent filled levels at 0 K while dashed lines are empty levels [25].*

The energy spacing between adjacent levels for an  $N$ -atom particle is of the order of  $E_F/N$ , where  $E_F$  is the Fermi energy of the bulk metal. Following the Kubo criterion, metallic properties presuppose the existence of a partially filled band with level spacing sufficiently small near the Fermi level so that a thermal activation can create electron-hole pairs, allowing a flow of current. The energy gap  $\Delta E$  (the so called Kubo gap) at  $E_F$  is given by

$$\Delta E \approx E_F/N \quad (2.1)$$

Smaller particles will have larger gap values. Fig. 2.2 represents the size dependent transition from metallic to non-metallic behaviour. As the full Fermi distribution width (10%-90%) is  $\sim 4kT$  i.e. 100 meV at room temperature, where  $k$  is the Boltzmann constant, smaller particles will require higher temperatures

to display metallic properties. The discretization of electronic levels, which leads to the suppression of the metallic behaviour when  $\Delta E > 2kT$ , is responsible for quantum size effects. The Fröhlich-Kubo definition of metallicity applies well to transition metals clusters, which are characterised by narrow  $d$  bands and hence high density of electronic states. The band gap of free mass selected copper cluster anion was measured with photoelectron spectroscopy by Pettiette *et al.* [26] and Ganteför *et al.* [22]. A clear semiconducting electronic structure has been found by those authors. In the present thesis we estimated the energy gap of mass selected copper clusters deposited on silicon in order to see the effect of the interaction with the substrate.

### 2.3 1/R behaviour and liquid drop model

One of the most important question is "*How large must a cluster be before its properties resemble those of the bulk element?*". This critical size depends on the nature of the constituent atoms and the kind of properties which are considered. Also the convergence to the bulk behaviour is different for various properties [27].

Important cluster properties are the ionisation potential (IP), the electron affinity (EA), the melting temperature ( $T_m$ ) and the cohesive binding energy ( $E_b$ ). For large nanoparticles ( $> 10$  nm) this properties show a scalable variation with the cluster size.

To derive scaling laws for the variation of these properties as a function of cluster size in the large cluster regime, a classical electrostatic model, the Liquid Drop Model (LDM), is used. In this model the particles are approximated by a uniform conductive sphere and atomic positions and internal electronic structure are ignored. Under this approximation the smooth variation of the cluster properties with size can be described for an N-atom cluster by a simple scaling law [25, 27]

$$G(R) = G(\infty) + aR^{-\alpha} \quad (2.2)$$

where  $G(\infty)$  is the value of the observable G in the bulk and the exponent is generally  $\alpha=1$ .

At low nuclearity the cluster properties show strong deviations from the liquid drop model (see Fig. 2.3) that are mainly attributed to quantum size effects (QSEs), like electronic shell closing, or geometrical effects. As an example of the application of scaling laws, the IP of a cluster of radius R is given by [28]

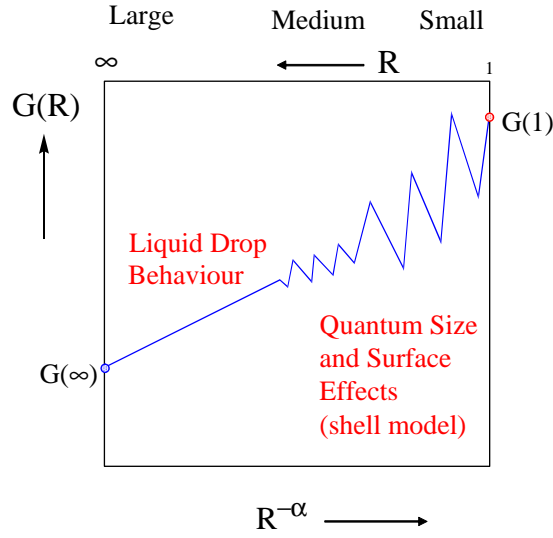


Figure 2.3: Schematic behaviour of a general cluster property  $G$  versus the inverse cluster radius  $R$  [25].

$$IP = W + \left( A \times \frac{e^2}{4\pi\epsilon_0 R} \right) \quad (2.3)$$

where  $e$  is the charge on the electron,  $W$  is the work function of the bulk metal and  $A$  is a factor that has been found to vary between 3/8 and 1/2.

By definition, the IP of a cluster corresponds to the energy difference of the neutral and the ionised clusters in their ground states. The EA, given by the energy difference of the negative and neutral clusters, is

$$EA = W - \left( B \times \frac{e^2}{4\pi\epsilon_0 R} \right) \quad (2.4)$$

where  $B$  is a factor which can vary from 1/2 and 5/8 [29,30]. Taylor *et al.* [17] measured the electron affinity of free mass selected copper clusters. Except for deviations in the small cluster regime, the prediction of the liquid-drop model (eq. 2.4) fits well the results for  $B=0,55$ . As  $1/R \rightarrow 0$ , the IP and EA both tend toward the bulk work function  $W$  (see Fig. 2.4).

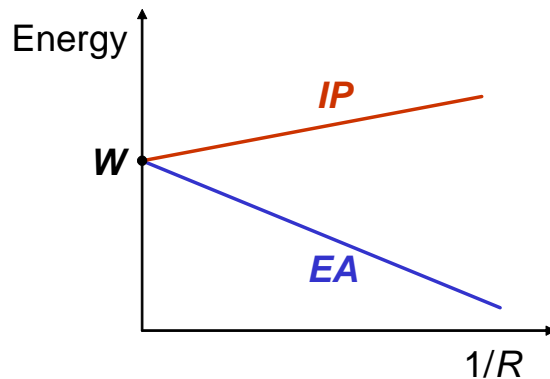


Figure 2.4: *Liquid-drop model for the variation of ionisation energy and electron affinity of a metal cluster versus the inverse cluster radius  $R$ .*

## 2.4 Deposited clusters and cluster diffusion

Free clusters are studied in order to understand the evolution of the electronic and geometric structure of the undisturbed, non interacting clusters. Since most applications involve supported clusters it is of fundamental importance to understand how the support affects the deposited particles.

The strength of the interaction between clusters and surface depends on the potential energy barrier as shown in Fig. 2.5. This strength determines the changes in geometrical and electronic properties of the clusters with respect to the unsupported case. For low interacting substrates, like carbon or  $MgO$ , the potential energy barrier keeps high and the electronic structure of the free clusters is mainly conserved. Instead, when the interaction of the clusters with the support is strong, as for the case of metallic surfaces, the highest occupied level of the clusters gets pinned to the Fermi level of the substrate. In that case the electronic structure of the clusters might dramatically change.

Fig. 2.6 shows a dynamical study of  $Be_{55}$  interacting with a Be (0001) surface at 0 K [32]. As in this case the cluster substrate interaction is quite strong there is a significant perturbation of the cluster geometry.

When the clusters are deposited at low impact energies on substrates at room temperature, they are often able to diffuse across the surface of the substrate. It has been found [33] that the most compact clusters diffuse faster with respect to the non-compact ones. Moreover, the cluster diffusion depends on the lattice mismatch between the cluster and the surface, since a good match leads to a

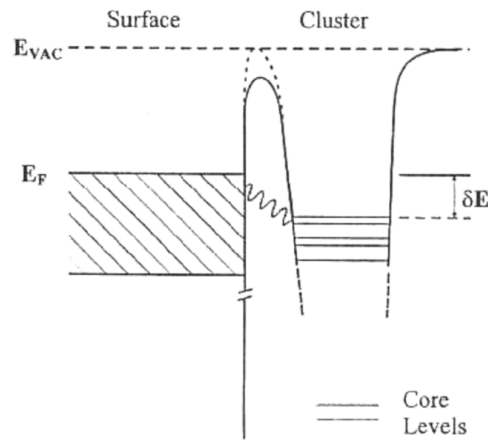


Figure 2.5: A metal cluster in contact with a conductive surface. The electronic level structure will be influenced by the presence of the surface [31].

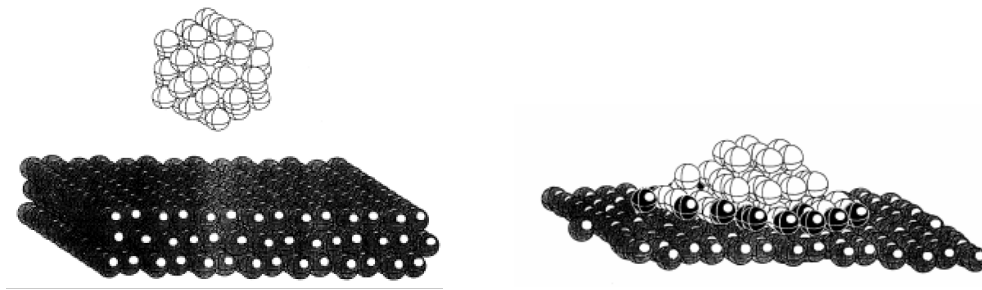


Figure 2.6: Interaction of  $Be_{55}$  with  $Be$  (0001) surface at 0 K due to molecular-dynamics calculation [32].

stronger cluster-substrate bounding and lower diffusivity.

Even if the clusters are mass-selected prior to deposition, they can afterwards aggregate on the surface. In order to aggregate, the interacting clusters must overcome an energy barrier. Therefore cluster coalescence depends on the material of which the particles are composed, on the size and shape and on the temperature. The aggregation of the deposited particles can be reduced by using an interacting substrate such as silicon, having dangling bonds. In fact, the interaction of copper with silicon is predicted to have a covalent character [34] which could be the reason that we have no indication of agglomeration at room temperature for copper clusters on a silicon surface (see chapter 5). The aggre-

gation of the deposited particles can be also reduced by pinning the clusters to the surface by the application of high deposition energy [7] which, however, easily leads to fragmentation of the clusters.

## 2.5 Soft landing

Cluster deposition is a process that can be performed at high or low ion kinetic energy, giving rise to different kind of phenomena that results from the cluster-surface collision. When the deposition energy is too high or the cluster-surface interaction is too strong there can be a plastic deformation of the particles, a fragmentation or an implantation into the surface, which cause an intermixing of the cluster atoms with the substrate. Structural deformation becomes less important for bigger cluster sizes because of the higher number of internal degrees of freedom. For higher cluster kinetic energies the particles can also be reflected (backscattered) or the substrate can be sputtered so that surface atoms are ejected.

Different methods can be used in order to avoid all these effects. The clusters can be deposited in a noble atom matrix [35] or clusters can be landed onto the surface with low kinetic energy, i.e. soft landing. In the case of soft landing, the particles are slowed down as much as possible in order to keep the clusters intact upon deposition. In order to deposit the clusters without fragmentation or implantation, molecular dynamics studies have shown that an impact energy less than 1 eV/atom should be used, regardless of the cluster-substrate system in use [36]. For a better control of the deposition energy the width of the kinetic energy dispersion has to be as small as possible.

In our experiment we ensured that the copper particles were softly landed by electrostatic deceleration after mass selection in order to avoid particle fragmentation.

## 2.6 Copper cluster: electronic structure and geometry

In this work the electronic structure of deposited Cu clusters have been investigated. Generally, noble metal clusters are highly interesting due to their closed  $d$ -shell, increasing  $sd$ -hybridization and 2D-dimensionality from  $Cu \rightarrow Au$ , as well as their chemical and catalytic activity [31, 37–39]. Furthermore, a semiconducting-like density-of-states makes small coinage metal clusters interesting objects to be used as tunable optical single-quantum emitters and sensors [40].

Copper, in particular, is a material of broad interest due to its diverse chemical and physical properties used in technology and fundamental science, e.g. superconductivity, catalytic properties or pronounced heat and electrical transport properties. Copper clusters, for example, can be used as catalysts in different processes. They can be applied for ammonia slipstream treatment after DeNOx selective catalytic reduction [41]. Size selected copper clusters can also catalyze at 330 K the polymerization of acetylene with butadiene as product [42] or they can be used for the dissociative chemisorption of  $H_2$  [43].

The electronic structure of free, mass selected Cu clusters has been intensively studied by laser photodetachment spectroscopy ( $h\nu = 1 - 7eV$ ) [18, 44]. Cheshnovsky *et al.* [44] recorded photoelectron spectra of free copper anions up to  $Cu_{410}$ , following the electronic structure from the atom to the bulk. Two bands were clearly discerned, one that grows out of the atomic  $4s$  levels and gradually transforms into the conduction band, and a second narrower band that emerges from the atomic  $3d$  levels and converges to the bulk  $3d$  bands. The uppermost electron density of states for free copper clusters is interpreted to be predominantly like that of a simple  $s^1$ -metal, and in fact the measured electron affinities were in agreement with the shell model predictions. Also Pettiette *et al.* [26], measuring the electron affinities of negative copper clusters, has found that the electron affinities are enhanced in the case of particles with a number of 2, 8, 20, 40 etc. (magic numbers which indicate filled electron shells) valence electrons as expected from the shell model. The authors observed also significant HOMO-LUMO band gaps for the magic clusters. On the other hand, the  $3d$ -binding-energy onset of copper clusters as a function of  $1/R$ , as measured by de Heer and Cheshnovsky [14, 44], shows a linear trend without any even-odd alternation. This means that the  $3d$  electrons of free Cu clusters are not delocalised but rather localised on the ionic core.

Predictions of the geometrical structure of free copper clusters have been made by several *ab initio* studies. For sizes  $N < 10$  first-principles based calculations have been used [45–47], while Kabir *et al.* applied tight-binding methods [48] for sizes up to  $N = 55$ . It has been found that copper clusters become exclusively three dimensional for sizes bigger than  $Cu_7$ . Moreover Kabir *et al.* has calculated that most of the clusters in the size range  $10 \leq N \leq 55$  adopt an icosahedral geometry. Doye *et al.*, using a Monte Carlo minimization approach, has found that the icosahedral structure is predominant for clusters size up to 100 atoms.

In this work mass selected copper clusters supported by an etched silicon wafer have been analysed with X-ray photoelectron spectroscopy, UPS, X-ray absorption and Auger spectroscopy. We used silicon as substrate as the interaction of semiconducting small copper clusters with silicon is of high interest for func-

tionalizing electronic devices in the semiconducting industry [49–51]. Moreover, several STM measurements revealed that on silicon substrates metal clusters do not diffuse or coalesce [9, 52, 53], while on graphite the clusters are mobile and easily aggregate [2]. In particular we are interested in understanding how the electronic energy levels of the copper clusters are affected by the silicon substrate and if the semiconducting nature found for free clusters [22, 26] is maintained upon deposition.

## 2.7 X-ray absorption measurements on copper

X-ray absorption studies on transition metals have received much interest since the  $L$ -edge absorption spectrum is very sensitive to the number of empty  $d$  or  $s$  valence states. In fact, in X-ray absorption from a core  $2p$  level ( $L_{2,3}$  absorption), dipole selection rules restrict the final state to either an  $s$  ( $l=0$ ) or  $d$  ( $l=2$ ) orbital. While X-ray studies of mass-selected Cu clusters are not available, bulk copper and many Cu-compounds with  $Cu^{I+}$  and  $Cu^{II+}$  electron configurations have been explicitly studied by X-ray spectroscopy including UPS and Auger spectroscopy [54–56]. Also, X-ray absorption spectroscopy has been done for matrix-embedded Cu-clusters [35]. Fig. 2.7 displays the absorption spectra of atomic copper from Arp *et al.* [57] and of Cu *fcc* crystal, solid  $Cu_2O$  and solid  $CuO$  from Mihai Sorin [58].

The differences between the Cu atomic and bulk absorption spectra are due to changes in the electronic distributions among  $s$  and  $d$  states. The general accepted electronic configuration of Cu atoms is  $(Ar)3d^{10}4s^1$ . The atomic Cu spectrum displays clear features corresponding to  $2p_{3/2,1/2} \rightarrow 4s$  and  $4d$  transitions, with a spin orbit splitting of about 20 eV, whereas there is no experimental evidence of  $2p_{3/2} \rightarrow 3d$  transitions.

The post-edge features are assigned to Rydberg transition such as  $2p_{3/2,1/2} \rightarrow 5s, 4d, 5d$  transitions or to discrete doubly excited states [57]. The absorption curve of Cu *fcc* crystal (Fig. 2.7) is mainly due to  $2p \rightarrow 3d$  transitions; even though no white line is observed, as it is for open  $d$ -shell metals, merely a small edge is observed for Cu bulk. The spectra calculated by Ebert *et al.* [59] show that the contribution of the  $s$ -absorption channel is only 5% of the total absorption intensity. This is mainly due to the fact that the relation of the radial matrix elements is  $\langle 2p|r|3d \rangle^2 / \langle 2p|r|4s \rangle^2 \approx 400$ , favouring transitions to the  $3d$  states.

The post edge fine structure in the  $L_3$  absorption spectrum of Cu bulk has been explained by single-scattering Bragg reflection [60], multiple scattering XANES theory such as Feff [61] or van Hove singularities of a *fcc*-crystal structure [59].

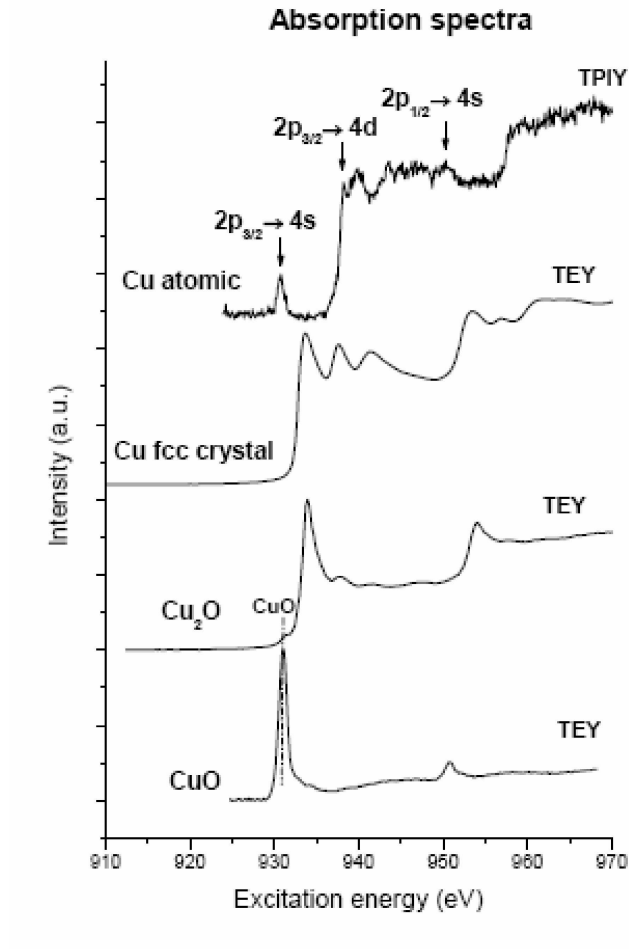


Figure 2.7: XANES spectra of atomic copper from Arp *et al.* [57] and of Cu fcc crystal, Cu<sub>2</sub>O bulk and CuO bulk from Mihai Sorin [58]. The XANES spectra of the copper atom is measured by the total photoion yield while the other spectra represent the total electron yield. In the single atom the 3d level is completely occupied, so the 2p electron is excited into the 4s level. For the pure Cu-metal a slight hybridization between d and s levels is apparent while for CuO the charge transition from Cu 3d to O 2p leads to an excitonic peak below the 2p<sub>3/2</sub> binding energy.

The influence of oxidation on solid Cu was extensively studied by Grioni *et al.* [54, 62] by investigating the Cu  $L_3$  absorption spectrum. It has been observed that the copper compounds and oxides, which have valence configuration  $Cu^0$  (Cu bulk),  $Cu^I$  (Cu<sub>2</sub>O) and  $Cu^{II}$  (CuO), do not have the respective ideal configuration (Ar)3d<sup>10</sup>4s<sup>1</sup>, (Ar)3d<sup>10</sup>4s<sup>0</sup> and (Ar)3d<sup>9</sup>4s<sup>0</sup>. Due to its strength, the

absorption edge of  $Cu_2O$  (Fig. 2.7), in fact, cannot be exclusively attributed to the  $2p \rightarrow 4s$  transition and part of its intensity must have also a  $3d$  character as a result of  $3d/4s$  hybridization. In the case of  $CuO$  instead, the near-edge region is concentrated in an intense narrow peak that is shifted from the one of pure copper by about 2 eV to lower energy. In this compound, in fact, a hole in the  $Cu d$  band provides favourable conditions for the formation of a bound excitonic state [54]. This means that the interaction between the core hole and the photoexcited electron in a  $d$  orbital is so strong that the electron is bound by the core-hole potential, and a "core exciton" is formed. The intensity of this peak is related to the total amount of  $Cu 3d$  character in the unoccupied states and the proof that it cannot be described as a density of state feature is given by the fact that the excitonic peak occurs at an excitation energy that is lower than the XPS threshold of the  $Cu 2p_{3/2}$  orbital.

# Chapter 3

## X-ray spectroscopy techniques

Over the years, X-ray photoelectron spectroscopy (XPS), X-ray absorption spectroscopy (XAS) and Auger electron spectroscopy (AES) have been found to show great applicability as element specific and local probe for the investigation of the electronic structure of atoms, molecules and bulk materials. In this work all these techniques are applied in order to study the evolution of electronic core levels of supported clusters and to deduce the metallicity, geometrical structure and interaction with the substrate.

### 3.1 X-ray spectroscopy on clusters

Several X-ray spectroscopy experiments have been performed on non mass selected clusters in the gas phase. Generally, a red shift of the X-ray absorption line with respect to the atomic line has been observed. This shift has been interpreted as due to a higher coordination number, i.e. better screening from the valence electrons of the neighboring atoms. Also, bulk and surface components could be resolved in the X-ray photoabsorption and ionisation spectra. The ratio surface-to-bulk is clearly enhanced for the clusters with respect to bulk. Knop *et al.* analysed the structure of free Ar clusters [63] and Kr clusters [63] by X-ray absorption (EXAFS, NEXAFS). Björneholm *et al.* studied free noble metal clusters by core level photoelectron spectroscopy and XAS [64, 65]. Feifel *et al.* analysed by photoelectron spectroscopy the inner valence levels of Ar, Kr and Xe clusters [66]. Tchapyguine *et al.* presented resonant photoemission and partial electron yield studies of free Ar clusters [67]. Piseri *et al.* studied by XAS free titanium clusters in a supersonic molecular beam [68]. Note, that a first NEXAFS measurement on mass selected metal clusters has been recently done by T. Lau *et al.* on mass selected free transition metal clusters [69].

X-ray investigations have been done also on deposited clusters [6, 8, 70–72]. In these experiments the particles have been obtained by vapour deposition of atoms on the surface [73–77], which means that the “clusters” represents rather islands of agglomerated atoms instead of well aggregated clusters formed in a supersonic beam. Mass selected clusters deposited from a cluster beam have been first studied by X-ray spectroscopy from the following groups: Eberhardt *et al.* [75] studied platinum clusters on silicon wafer covered by natural oxide, O’Shea *et al.* [78] investigated by XPS deposited silver clusters on a Xe covered  $Al_2O_3$  surface, Siekmann *et al.* [79] analysed Pb and Au clusters on *Si*,  $SiO_2$  and on polycrystalline silver, DiCenzo *et al.* [8] studied mass selected gold clusters on amorphous carbon, D. C. Lim *et al.* [80, 81] analysed by XPS the oxidation of mass selected deposited Au clusters and Roy *et al.* characterized by XPS and UPS mass selected Pt and Pd clusters deposited on Ag [10]. T. Lau *et al.* [82, 83] performed soft landing deposition of mass selected iron clusters for X-ray absorption spectroscopy and X-ray magnetic circular dichroism investigations.

In most of the above studies the size-dependent energy shifts of the electron energy levels have been investigated. In general, it has been found that the electron binding energy is larger in the clusters with respect to the bulk metal and that the binding energy decreases with increasing cluster size.

To our knowledge, mass-selected deposited Cu clusters have not been analysed by X-ray spectroscopy so far. Several work have been published about Cu clusters deposited on different surfaces, but in no case there has been used an exact control of the cluster size [4–6, 73, 76, 84–86]. Core levels as well as valence bands have been studied by XPS and UPS. In most of the studies carbon, a weakly interacting material, has been used as substrate except for the “clusters” measured by Pászti *et al.* [73] which have been deposited on silicon. In some cases the binding energy shifts of particles deposited on different surfaces have been compared. A positive binding energy shift has been generally observed, bigger for the valence band than for the core levels. Lai *et al.* has found a negative binding energy shift for the core levels of Cu “clusters” on Ni [86].

## 3.2 XPS

XPS is a common tool to investigate atoms, molecules, surfaces and solids. On mass selected deposited clusters there is still a lack of XPS measurements due to intensity reasons. On free clusters it is still not possible to perform XPS by synchrotron light, only some recent measurements on Pb clusters at an FEL source (Free Electron Laser, FLASH Hamburg) have been done [87]. Neverthe-

less, on deposited clusters synchrotron radiation can be applied by accumulating individual clusters from a beam up to 1% surface coverage. A very important information resides in the core binding energy shift, i.e. the ESCA (Electron Spectroscopy for Chemical Analysis) shift of the core orbital binding energy with respect to a reference material [88]. For the deposited clusters we considered the chemical state with respect to the Cu-bulk value.

Upon investigating clusters in the gas phase by photoelectron spectroscopy it is possible to detect the undisturbed electronic structure of the pristine clusters. On the other hand for any kind of application such as catalysis, optoelectronics or magnetism, the particles have to be deposited onto a surface. For supported clusters it is thus important to understand how the electronic levels and the geometry of the clusters are altered by the interaction with the substrate [4, 6, 73, 84, 89, 90].

XPS is generally used to investigate the inner shell orbitals. In fact, the photoelectric cross section in the soft X-ray regime is larger for the core electrons than for the valence electrons. As core level peaks are usually quite sharp and element specific [91] they can be used to get information on the chemical state of the clusters [92]. Especially when the clusters are in contact with a support. In fact, the small chemical changes induced by the local atomic environment become reflected in the core-electron binding-energy shift  $\Delta BE$  also called ESCA shift.

Nevertheless, XPS measurements of mass-selected clusters on a surface are still sparse due to the difficulties to gain a high enough target density in a reasonable time. For this ca. 0,1-1 nA deposition current is necessary to receive a cluster coverage density of 1% within 10 to 30 min. This coverage is sufficient to carry out synchrotron studies on individual, non-agglomerated clusters as will be shown throughout this thesis.

### 3.2.1 XPS principle

XPS has its origins in the investigations of the photoelectric effect (discovered by Hertz in 1887 [93] and explained by Einstein in 1905 [94]). ESCA was developed in the mid-1960's by K. Siegbahn and his group at the University of Uppsala, Sweden [92] as quantitative tool to study the chemical state of atoms, molecules and solid matter. The scope of photoelectron spectroscopy is to shine monochromatic radiation onto a sample and to measure the energy distribution of the photoemitted electrons (see Fig. 3.1). The measured kinetic energy is given by

$$KE = h\nu - BE - \phi_s \quad (3.1)$$

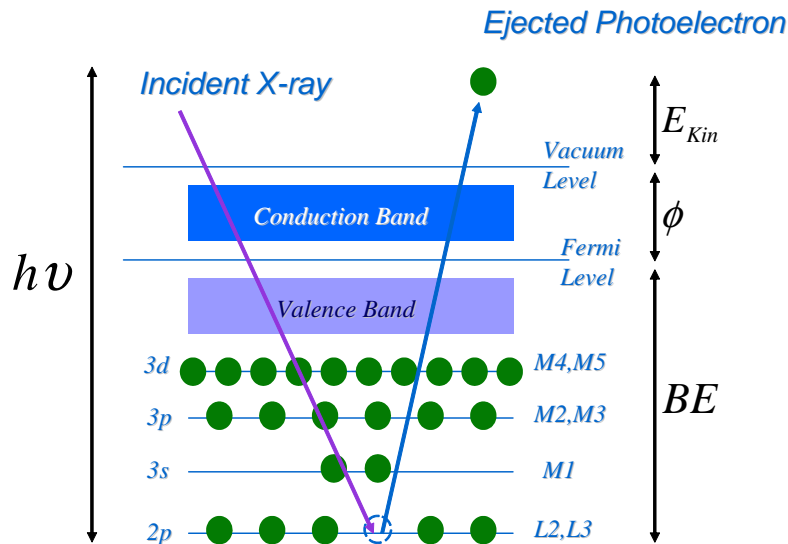


Figure 3.1: XPS process. An incoming photon causes the ejection of the photoelectron.

where  $h\nu$  is the photon energy,  $BE$  is the binding energy of the atomic orbital from which the electron originates, and  $\phi_s$  is the sample work function. The binding energy is defined as the energy difference between the initial and the final state. As the sample is grounded to the spectrometer, the Fermi levels of the sample and the spectrometer coincide (see Fig. 3.2). The ejected photoelectron has to overcome the work function of the sample, but when it enters the spectrometer its kinetic energy is adjusted to the work function of the spectrometer. It is then only needed to know the spectrometer work function to calculate the binding energy, which is measured relative to the Fermi level of the spectrometer [95]. Core level shifts are considered relative to the binding energy of a reference material usually the corresponding bulk metal, determined by measurements on a thick metal layer or a single crystal.

The basic parameter that governs the relative intensities of core-level photoionisation peaks is the atomic photoemission cross-section,  $\sigma$ . The differential cross section, given by the sum over all possible initial states which satisfy energy conservation, is expressed in the single particle approximation by the *golden rule* expression [96]:

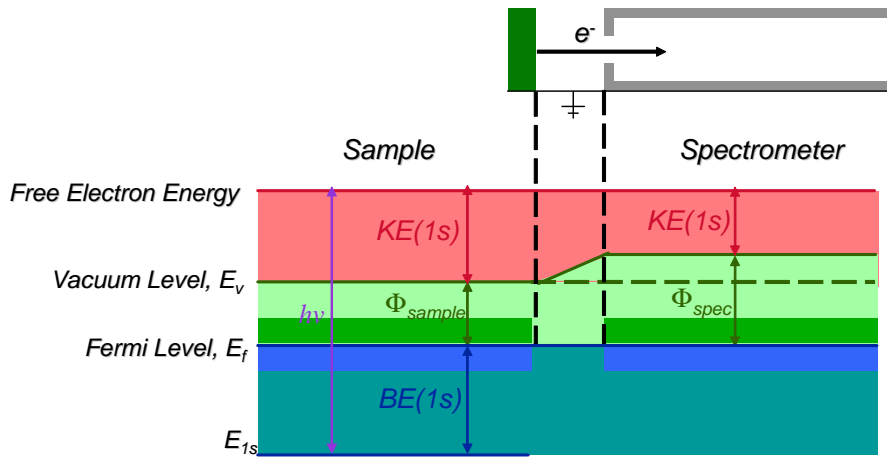


Figure 3.2: Alignment of the Fermi levels of the sample and the spectrometer in the case of a conducting sample.

$$\frac{d}{d\Omega}\sigma(E_f, \hbar\omega, A) \sim \kappa \sum_i |\langle \Psi_f | p \times A | \Psi_i \rangle|^2 \delta(E_f - E_i - \hbar\omega) \quad (3.2)$$

where  $E_f$  and  $E_i$  are the final and initial energy of the electron,  $A$  the photon field,  $\kappa \sim \sqrt{E_f}$  the density of final states,  $\Psi_i$  and  $\Psi_f$  the initial- and final-state wave function of the electron and  $p$  the momentum operator.

The peak width  $\Delta E$ , defined as the full width at half-maximum (FWHM), is a convolution of several factors [97]:

$$\Delta E \approx (\Delta E_n^2 + \Delta E_p^2 + \Delta E_a^2)^{1/2} \quad (3.3)$$

where  $\Delta E_n$  is the natural lifetime width of the ionised core level,  $\Delta E_p$  is the width of the photon source (monochromator resolution) and  $\Delta E_a$  the electron analyser resolution.

Due to the much stronger scattering cross section of electrons with respect to photons the XPS method is very surface sensitive. The sensitivity can be varied by varying the kinetic energy of the escaping photoelectron by tuning the exciting photon energy as shown in Fig. 3.3.

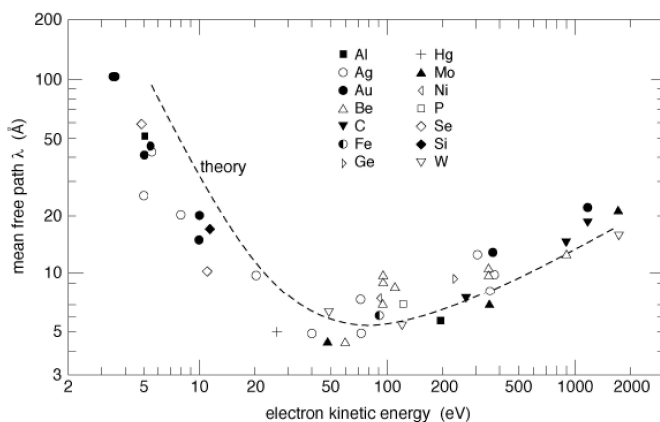


Figure 3.3: *Universal curve representing the kinetic energy dependence of the inelastic mean free path of photoelectrons [98]*

### 3.3 XANES

X-ray absorption spectroscopy measures the absorption of X-rays by the sample as a function of X-ray energy [99]. If the absorption coefficient is plotted as a

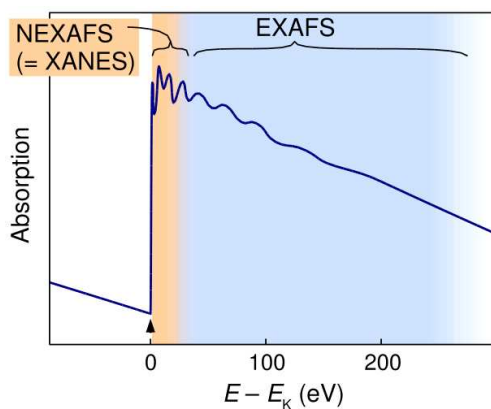


Figure 3.4: *Schematic representation of an X-ray absorption spectrum. The spectrum is divided into three main regions: the pre-edge, the near edge structure XANES and the fine structure range EXAFS (Extended X-ray Absorption Fine Structure) [100].*

function of the photon energy  $E$  (Fig. 3.4), the experimental data shows a sharp rise at a certain energy called absorption edge, which is superimposed by a series of wiggles or oscillatory structure. Beyond the edge an overall decrease of the

X-ray absorption signal with increasing energy follows.

Each absorption edge is related to a specific atom present in the material and, more specifically, to a quantum-mechanical transition that excites a particular atomic core-orbital electron to an unoccupied state, i.e. into an empty orbital above the Fermi energy (Fig. 3.5). Thus, the near edge region is sensitive to the unoccupied density of states. The transition from the initial to the final state is subject to dipole selection rules. Therefore, the  $L$  edge in transition metals,

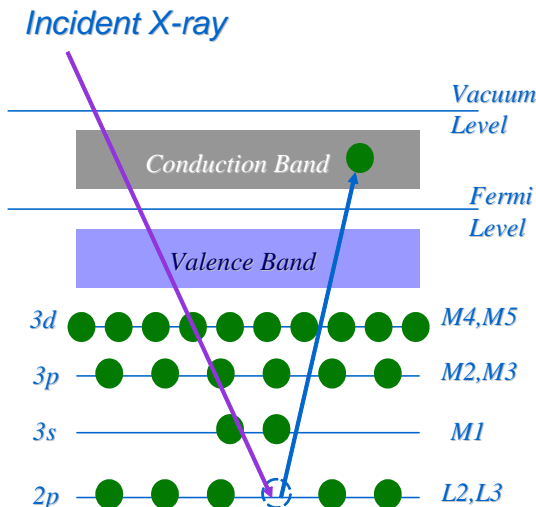


Figure 3.5: *Schematic representation of an X-ray absorption process in case of condensed matter. The core electron that absorbs the photon is projected into the conduction band.*

as this of Cu, is sensitive to the presence of low-lying  $s$  and  $d$  empty states due to dipole selection rules. The strong peak at the  $L_3$  edge of transition metals is called "white line". Its large intensity is due to the atomic like character of the  $d$  resonance in open shell transition metals. This name has its origin when this phenomenon was first observed on a photographic film on which the large absorption peak appeared as an unexposed "white line" on the negative.

The modulations shortly above the core ionisation threshold arises from the alternating constructive and destructive interference between the outgoing electron wave and the electron wave that is scattered back by neighboring atoms. The amount of interference depends on the internuclear distance and on the strength of the scattering from the neighboring atoms and the number of scatters [99].

The full series of structures extending within the first  $\sim 30$  eV above the absorption edge (NEXAFS) have been identified as multiple scattering resonance of the excited photoelectron scattered by neighbour atoms. Multiple-scattering is informative on the relative positions of neighbour atoms (coordination geometry and bond angles). In contrast to diffraction techniques, the local structure can be obtained by NEXAFS without the need of a long range crystallographic order.

At energies higher than 40 eV above the absorption edge, the scattering of the excited electron is so weak that the main contributions to the final state wave function in the vicinity of the absorbing atom originates from single scattering process, in which the relatively fast photoelectron is scattered by only one neighbour atom. Therefore EXAFS gives information about the local structure in terms of the atomic radial distribution function (interatomic distances and coordination numbers).

Several techniques for measuring the absorption spectra have been developed and can be classified by either transmission or yield detection mode [101]. In the transmission mode the relative intensity of the incoming and transmitted beams are measured. In the yield mode either the emitted X-ray photons or the Auger electrons (see paragraph 3.7) which are emitted after the decay of the core hole are detected. A comparison of the amount of the Auger with fluorescence decays

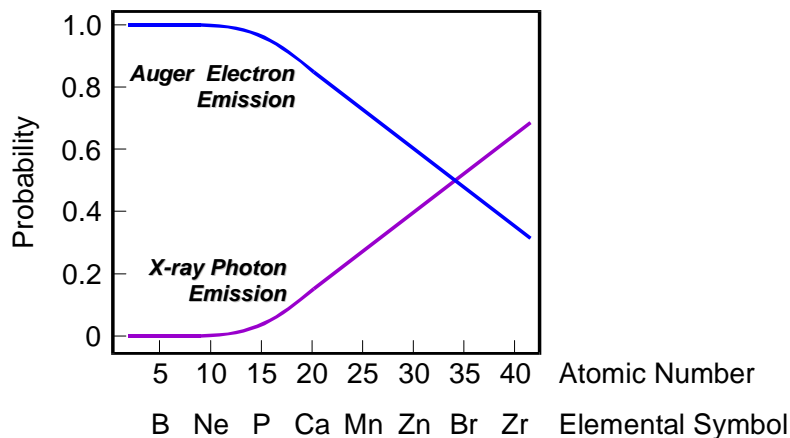


Figure 3.6: *Relative probabilities of relaxation of a K-shell core hole by emission of an Auger electron and an X-ray photon of characteristic energy. The light elements have a low cross section for X-ray emission [97].*

shows that the Auger decay dominates for light elements (Fig. 3.6).

In this thesis the absorption measurements of the deposited clusters were

performed in total yield mode by measuring the total photocurrent on the sample by an electrometer.

### 3.4 Auger

Due to the involvement of core-hole states, the Auger process is an element specific spectroscopy technique. Following the photoionisation of a core hole, an electron from a valence level fills the core hole under the simultaneous ejection of a second electron (Auger electron) into the continuum (see Fig. 3.7).

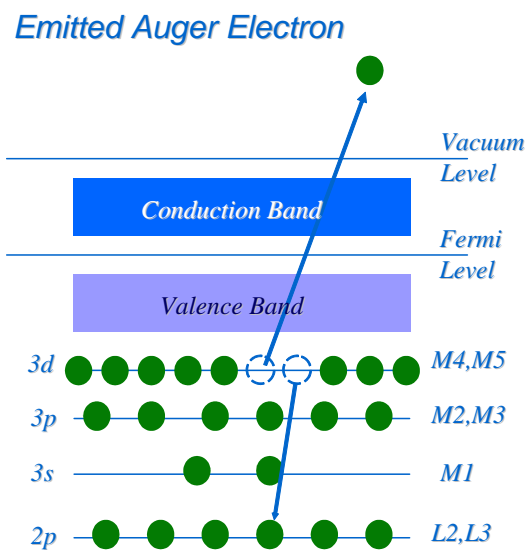


Figure 3.7: *Schematic diagram of Auger electron emission. The hole in the L shell is filled by an electron from  $M_{4,5}$  releasing an amount of energy ( $E_L - E_{M_{4,5}}$ ) that can be given to another electron. In this example the Auger electron stems from the same shell as this which fills the core hole. The system is left with a final state charge +2.*

The initial state of the Auger process is characterised by a core hole, while in the final state two electrons are missing in the valence shell. The ejected Auger electron will have a kinetic energy given by the energy difference of the initial and final state. The Auger energy is independent to the photon energy of the incoming beam. For light elements ( $N < 35$ ) the Auger emission is dominant over

the competing X-ray emission process (see Fig. 3.6).

The Auger transition represented in Fig. 3.7 is called  $LM_{4,5}M_{4,5}$ . The kinetic energy of the ejected Auger electron is given by the following expression:

$$KE = E(L) - E(M_4) - E(M_5) - U(M_4, M_5) \quad (3.4)$$

where  $E(L)$ ,  $E(M_4)$  and  $E(M_5)$  are the binding energies of the respective core and valence states and  $U(M_4, M_5)$  is the Coulomb interaction of the two remaining holes. The Auger process can be explained as a nonradiative core-hole relaxation process which is governed by the Coulomb operator.

As in the case of XPS spectra, the energy of the Auger peak is affected by the chemical environment of the atoms. Fine structures in Auger spectra are normally seen in any kind of material and can have their origin either in chemical effects (initial state) or in final-state effects (multiplet splitting).

When a core electron is photoexcited to a resonant bound state and not to the continuum, the subsequent core-hole relaxation process is called resonant Auger (Fig. 3.8 *left*). In contrast to the normal Auger process an extra electron is

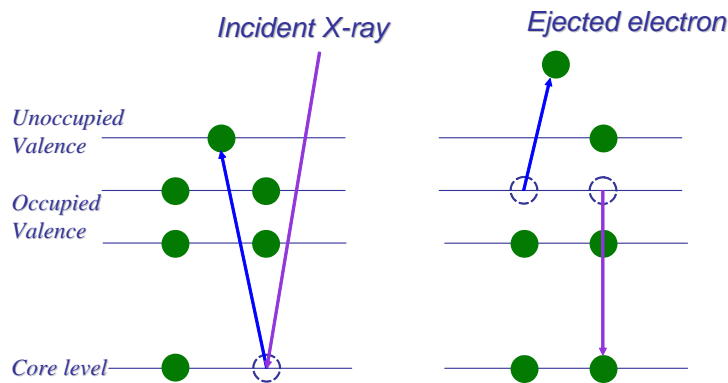


Figure 3.8: *Left: Photoexcitation of a core electron to a resonant bound state. Right: Auger decay after resonant excitation. The system is left with a charge +1.*

present in the final state of a resonant Auger process. Thus the system is left in a valence-excited final state with a charge of +1 (Fig. 3.8 *right*). Usually the cross section for the resonant Auger is higher than for the normal Auger process. This fact can be explained by the Kramers-Heisenberg formula [102], as the denominator converges towards zero at resonance.

# Chapter 4

## Experimental apparatus

### 4.1 Cluster deposition

Figure 4.1 shows an overview of the cluster deposition apparatus installed at BESSY. The clusters are produced by a combination of magnetron sputtering and atom agglomeration within a supersonic beam. After passing a biased skimmer and first focusing lens installed between the first and second skimmer, the cluster ions (cations) are accelerated by electrostatic lenses to -4000 V. After acceleration the cluster cations are focused onto the entrance slit of a dipole sector magnet by a system of electrostatic lenses. Due to their different momentum the clusters are spatially dispersed by the bending magnet and are focused onto the exit slit. Finally the clusters are decelerated and focused in order to get softly landed onto a biased substrate. The deposition is performed under UHV conditions. With the help of a mobile vacuum chamber the samples are transferred from our laboratory to the beamline where the samples are loaded into the photoemission chamber.

#### 4.1.1 Vacuum system

As in the source chamber during cluster production a pressure of the order of  $10^{-4}$  mbar exists, five differential pumping stages are used [103] in order to keep a pressure in the deposition chamber better than  $10^{-9}$  mbar. The source chamber is pumped by a 2200 l/s turbopump (Pfeiffer TPU 2200) connected to two prepumps, a 280 l/s roots blower (Pfeiffer WKP 1000 A) and a 36 l/s rotary pump (Pfeiffer DUO 120 A). Between the two skimmers is used a 920 l/s turbo drag pump (Pfeiffer TMU 1001 D) and before the mass analyser a 180 l/s turbopump (Pfeiffer TPU 180). Due to the low cross section ( $50 \times 30 \text{ mm}^2$ ) and 50 cm length of the bending magnet ion tube, that cause a high flow resistance, it is possible to keep after the mass selection a pressure of the order of  $10^{-8}$  mbar.

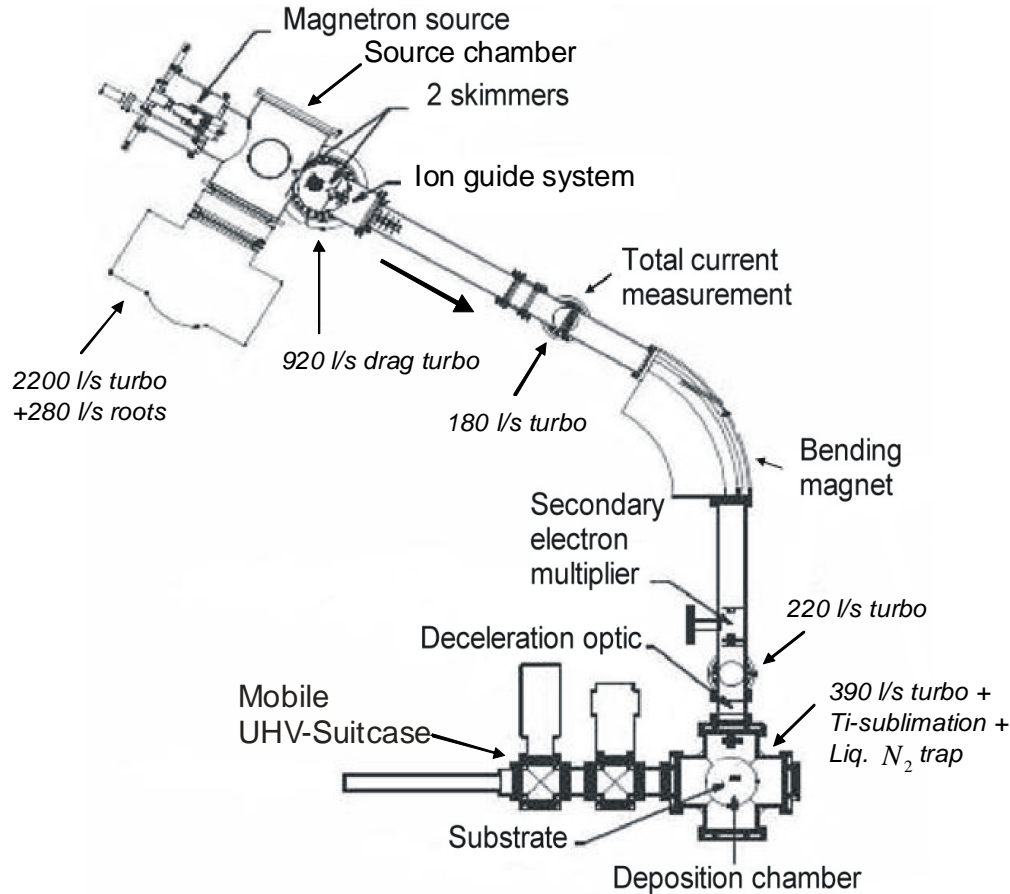


Figure 4.1: *Experimental setup for cluster deposition at BESSY.*

Here the chamber is pumped by a 220 l/s turbopump (Pfeiffer TMU 260) while the deposition chamber by a 390 l/s turbopump (Pfeiffer TPU 450 H), a liquid nitrogen trap and a titanium sublimation pump (which is not used during cluster deposition). In the transfer system to keep UHV condition a battery-driven ion getter pump is used (Fig. 4.1) .

### 4.1.2 Cluster production

The home-build magnetron sputtering cluster source [104], represented in Figure 4.2, is essentially similar to the one constructed by Haberland's group [105] and is a combination of a gas discharge sputter source with an inert gas condensation technique [104]. This source has the advantage of generating a continuous

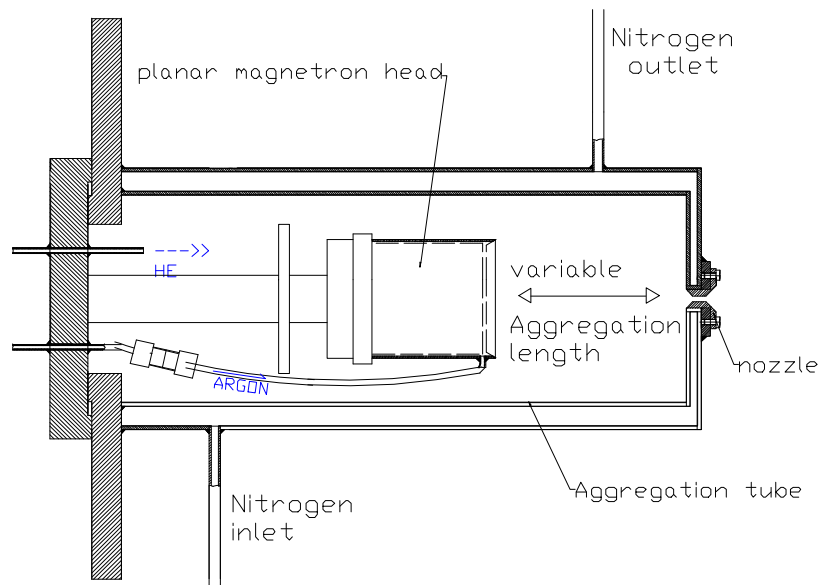


Figure 4.2: *Cluster source composed by a planar magnetron sputtering head (2 inch) placed inside a liquid nitrogen cooled aggregation tube.*

beam of clusters having a size distribution that can be adjusted within broad limits. Moreover with the magnetron ion cluster source it is possible to vapourise a wide range of materials, such as metals and semiconductors [14]. As shown in Fig. 4.2, a commercial planar magnetron sputtering head (Thin Film Consulting, ION'X-2UHV) controlled by a power stabilized DC-generator (HUTTINGER, PFG 1500 DC) is located inside a stainless steel tube cooled by liquid nitrogen. The target is sputtered by argon and the ejected atoms aggregate in collision with the surrounding gas atoms (He and Ar). The measured pressure inside the condensation zone ranged between 0.5-1 mbar. The gas sweeps the clusters from the aggregation region towards the aperture at the end of the aggregation chamber [104]. The vapour mixture is then subject to an adiabatic expansion, which cools the gas and gives a forward direction, into a vacuum region of  $10^{-3} - 10^{-4}$  mbar. The expanding gas passes through a skimmer which collimates the central portion and deflects the rest of the gas.

### Magnetron sputtering source

Plasma confinement on the target surface is achieved by locating a permanent magnet structure behind the target surface (Fig. 4.3). The resulting magnetic

field forms a closed-loop annular path acting as an electron trap that shapes the trajectories of the secondary electrons ejected from the target into a spiral path. This greatly increases the probability of ionisation of the sputtering gas within the confinement zone. The magnets enhance the electron density near the surface and increase the sputter yield even at low operating pressures. Since the ion bombardment takes place mainly where the magnetic field lines are parallel, the sputtered region of the target is an annular ring. The copper targets are 4 mm thick, have a diameter of 2 inch and last for about 20 hours (Fig. 4.4).

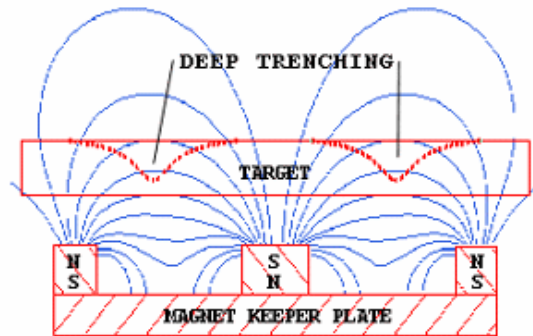


Figure 4.3: *Magnetic field lines (blue) of the magnetron sputtering source [106].*

As most of the power applied for sputtering ends up as heat into the target material, the cathode has to be water cooled. In normal working condition we have a water flux of 2 l/min.

### Gas-aggregation source

The sputtered atoms and ions are swept into the condensation region by the He and Ar gas flow (Fig. 4.5). Here they are cooled and condensed through collisions with the cold gas atoms leading to the formation of electrically charged clusters [7].



Figure 4.4: *Sputtered Cu-target, diameter=2".*

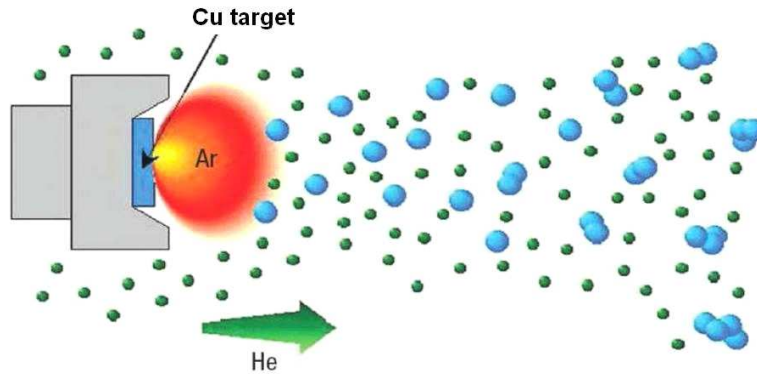
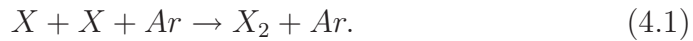


Figure 4.5: *Clusters formation by sputtering and aggregation [7].*

- *Clusters formation*

As at the beginning only atoms are present, the agglomeration has to start with the dimer formation. For this process, due to the energy and momentum conservation laws, it is necessary a three body collision [107]. If  $X$  is a sputtered atom and we consider a collision with an  $Ar$  gas atom we have



In the first stage, when the density of single atoms still dominates with respect to larger clusters, the dimers grow by addition of monomers cooling by collisions with the rare gas [108]



When the density of clusters increases they continue to grow by cluster-cluster agglomeration:



The inverse process is called evaporation and compete to give the final cluster distribution.

- *Ionization*

The ionisation of the clusters is an efficient process. In fact even if sputtered atoms from a metal surface are predominantly neutral, a high ratio

of charged and electronically excited species are originated in the plasma near the magnetron source.

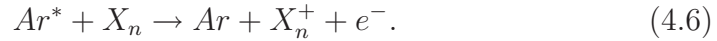
If only one sputtered atom is charged, and this coalesce with a neutral cluster, the resulting cluster will be charged as well:



Anyway near the magnetron cathode the predominant charged species is the argon, that can transfer its charge to the metal atoms and clusters



In this case the reverse process cannot occur as the Ar has an ionisation energy much higher than that of any metal. The argon atom, following a collision with an electron in the plasma region, can also be excited. In this case positive ions will be formed with a mechanism that is called Penning ionisation:



The asterisk is denoting the excited electronic state. In the plasma, besides positive and excited Ar atoms, there is also a high concentration of electrons, which can generate negatively charged clusters:



This electrons can cause also a recombination process, that leads to a charge loss



The cluster size can be varied by adjusting several parameters such as the rate of the gas flow, the power supplied to the magnetron, the temperature of the aggregation region, the aperture diameter and the distance between the magnetron and the aperture. The cluster size is increasing as long as clusters remain in the condensation region before passing the aperture. This means that with higher aggregation length, smaller aperture, lower He flow, it is possible to produce bigger clusters. The cooling of the source with liquid nitrogen reduces the internal

energy of the clusters, thus limiting the re-evaporation of atoms from the clusters due to accumulation of condensation heat.

### 4.1.3 Mass selection

A magnetic field analyser (AMD Intectra) is used for mass selection of the cluster ions. After electrostatic acceleration and collimation by a system of electrostatic lenses, the clusters enter a magnetic sector field. Because of the presence of a homogeneous magnetic field (up to 1.2 Tesla) directed perpendicular to the ion flight direction, the cluster beam is deflected by the Lorentz force in the horizontal plane of the laboratory. The angle of deflection is  $58^\circ$  and at the end of the sector field a narrow slit selects clusters with a particular momentum  $p = mv$ . Scanning the magnetic flux density of the magnet and keeping a constant acceleration voltage (-4000 V), a typical mass spectrum is shown in Fig. 4.6.

As seen in Fig. 4.6, the cluster intensities are a quite smooth function of the cluster size which shows the proper expansion conditions of the cluster source.

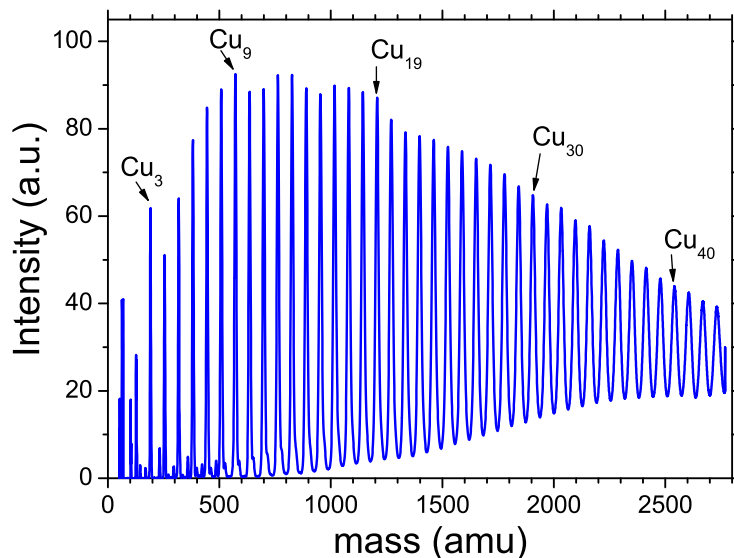


Figure 4.6: *Mass spectrum of cationic Cu clusters up to Cu<sub>43</sub>.*

The resolution  $m/\Delta m$  depends on the size range. It starts at  $\sim 60$  (see Fig. 4.7) for low masses and reaches a resolution of  $\sim 300$  between 1000 and 2000 amu [103]. In Fig. 4.7 the isotope pattern of the  $Cu_2$  dimer is shown. The

isotopic splitting is nicely resolved, with atomic mass unit of 63 and 65. The first peak represents the dimer constituted by two  $^{63}\text{Cu}$  isotopes, the second peak is a combination of the two different isotopes and the peak at 130 a.m.u. is due to two atoms of  $^{65}\text{Cu}$ .

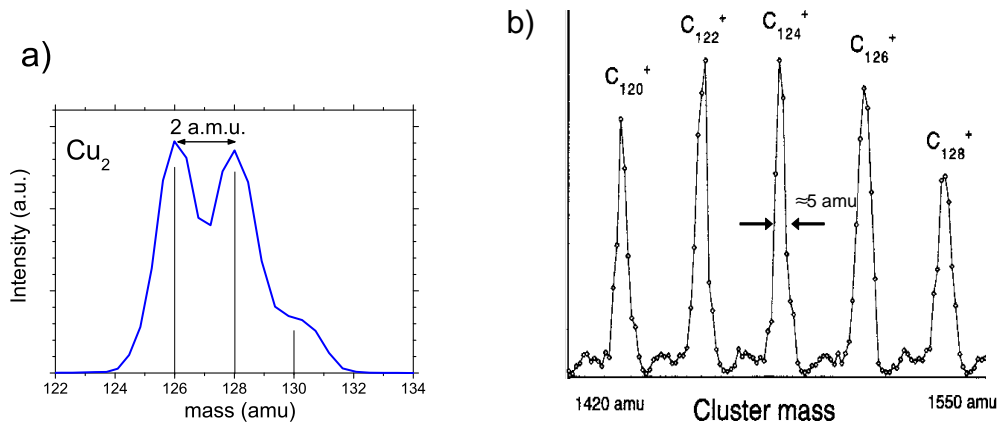


Figure 4.7: a): Isotope mass spectrum of  $\text{Cu}_2$  from which a resolution of  $\sim 60$  is deduced at low masses. b): Mass spectrum of carbon clusters [103] from which a resolution of  $\sim 300$  is deduced for masses  $\sim 1500$  amu.

#### 4.1.4 Ion optic system

Figure 4.8 schematically shows the system of electrostatic lenses used to guide the ions through the apparatus from the source to the deposition chamber. A first skimmer with an orifice of 5 mm diameter, placed 20 cm behind the cluster source nozzle (opening=4 mm), collimates the beam and keeps back the main part of the carrier gas. A slight attractive voltage ( $< -100$  V) is usually applied on the first skimmer. On their way through a differential pumping stage (length=30 cm), the clusters are focused by an Einzel lens before the cluster beam passes a biased second skimmer with an aperture of 6 mm. Before entering the mass spectrometer the cluster ions are accelerated to 4 keV by a system of Einzel lenses that focus and deflects the beam. The ion optics utilise electrostatic forces on charged particles to modify ion trajectories. The position of the focus depends on the ion kinetic energy, so a strong initial acceleration is applied to reduce the relative energy spread. The ion current before the bending magnet is measured with an electrically isolated metal plate. This can be moved in and out the beam (Fig. 4.8) and is connected to a battery driven analog electrometer (Keithley

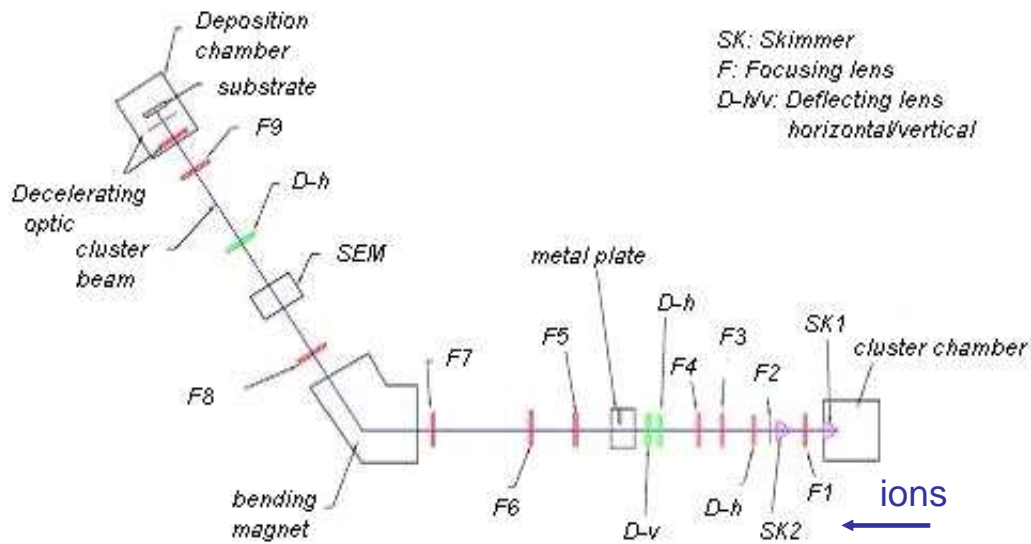


Figure 4.8: Arrangement of ion optics.

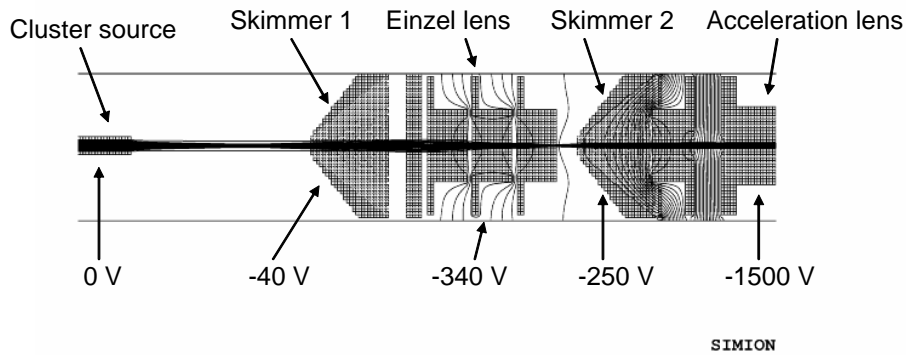


Figure 4.9: Initial skimmer/lens system and equipotential line.

601). A typical value for the total ion current is  $\sim 10$  nA. The focusing lenses F1, F3, F4, F5, F6, F9 (see Fig. 4.8) have additionally been inserted after performing ion trajectory simulations carried out with the ion optic simulation program SIMION (SIMION 3D, Version 6.0). The initial skimmer/lens system is

shown in Fig. 4.9 where also equipotential lines are represented. In this picture the cluster ions coming out from the nozzle are passing through the two skimmers and then become accelerated to high voltage (-4000 V).

To test the transmission of the whole machine we used a Caesium oven for generating a beam of  $Cs^+$  atoms by resistive heating. In front of the magnet we measured a current of  $\sim 30$  nA, while at the secondary electron multiplier (SEM), placed behind the magnet, we measured about 5 nA, a factor of 1/6 [104]. Finally, at the substrate, we had a current of about 2 nA, i.e. a total transmission of ca. 5-10%.

### 4.1.5 Cu cluster deposition

After passing the exit slit of the bending magnet the cluster ions are refocused and deflected before entering the deposition chamber. To allow for a non destructive deposition of the cluster, the 4 keV kinetic energy of the ions is reduced using three subsequent electrostatic lenses that focus the beam through a final circular aperture of 6 mm diameter (Fig. 4.10). This is placed about 2 mm in front of the substrate. To keep a more homogeneous electric field between the aperture and the substrate a gold mesh with transmission of 80% is fixed to the final orifice.

The substrate voltage can be varied from -100 V and +100 V and is applied by a electrometer (Keithley 617) which measures the ion current. Fig. 4.10 represents the deposition ion optics. This consists of a combination of decelerating and accelerating lenses in order to slow down and refocus the clusters ions into a narrow spot. To allow for a non destructive deposition the cluster ions are decelerated to a final kinetic energy  $< 1$  eV per atom.

The total number of clusters reaching the surface has been measured by continuously recording the ion current during deposition (see Fig. 4.11). Note that the deposition energy is measured under soft-landing conditions, i.e. after decelerating the clusters.

The temporary sharp drops to zero in Fig. 4.11 are due to an increase of the deposition bias voltage until a zero ion current on the substrate is reached. In this way the initial kinetic energy of the cluster ions can be evaluated, as it corresponds to the potential at which the ion current drops to zero. Then a value smaller than 1 eV/atom is subtracted to this zero current potential in order to perform soft landing deposition. As the kinetic energy of the cluster ions can slightly change during the deposition process this check must be regularly done.

To determine the density distribution of the clusters on the silicon surface the photocurrent has been measured at the  $L_3$  absorption edge maximum (see paragraph 5.3.1) while moving the sample position (see Fig. 4.11). It results that

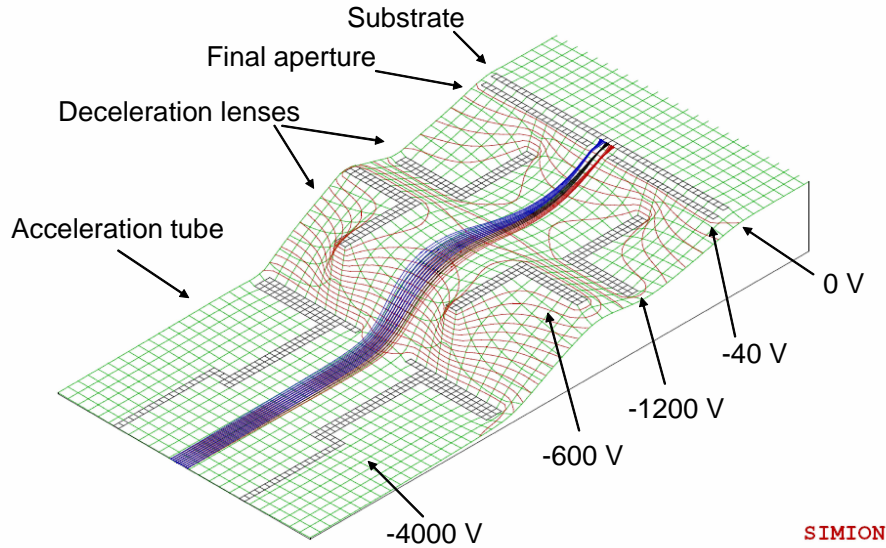


Figure 4.10: *Deposition lenses: view of the applied voltages (green), of the equipotential lines (red) and of the ion beam trajectories (blue, black, red). The three colours for the trajectories indicate three different initial angles.*

the diameter of the deposited area is ca. 7 mm, i.e. similar to the final aperture of 6 mm. From the measured total ion current and the spot size, we estimate as typical cluster coverage density  $1,3 \times 10^{12}/\text{cm}^2$  (see Fig. 4.12). Hensel *et al.* [109] estimated for the Si(100) surface that an area of  $2\sqrt{2}a_0 \times 2\sqrt{2}a_0$  contains  $4 \times 4$  atoms ( $a_0 = 5.4 \text{ \AA}$  is the lattice constant). As this corresponds to  $8 \times 10^{14}$  Si atoms per  $\text{cm}^2$ , we calculated the deposited copper atoms of  $\text{Cu}_7$  to be  $\sim 1\%$  of a silicon monolayer (see also paragraph 5.1).

#### 4.1.6 Defined cluster size optimisation

To optimise the current intensity of a single cluster size, the conditions of operation of the cluster source are varied, such as the aggregation length, source power, gas pressure and aperture of the nozzle. Increasing the residence time of the particles within the aggregation tube by increasing the distance magnetron head-to-nozzle bigger cluster are generally produced.

For example, for the deposition of  $\text{Cu}_8$  we used a power of 70 Watt, an aggregation length of the condensation tube of 9 cm, a helium pressure of 1 mbar

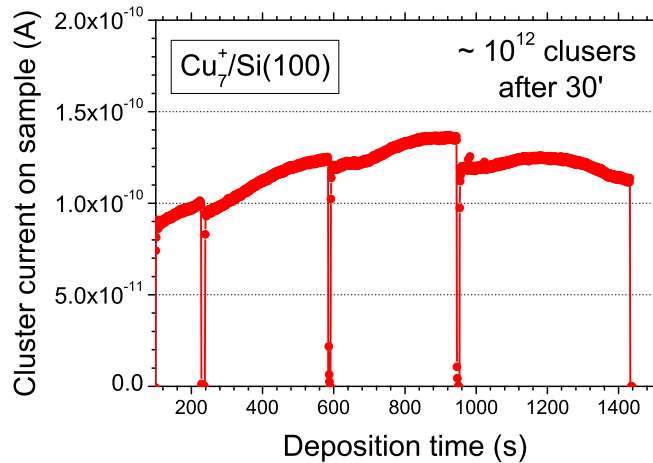


Figure 4.11: *Deposition intensity recorded for  $\text{Cu}_7^+$ ; a total amount of  $10^{12}$  clusters are deposited within 30 min. The sudden intensity drop is artificially generated by deflecting-off the cluster beam electrostatically to check the value of the sample voltage for which the cluster ion current is zero.*

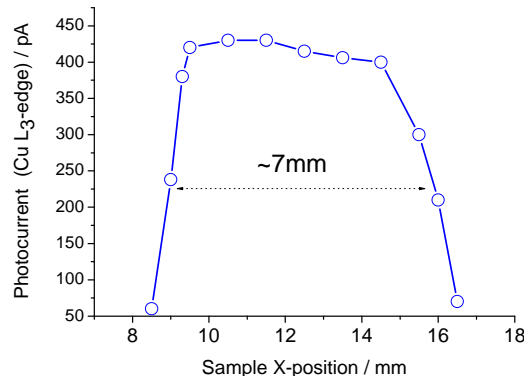


Figure 4.12: *Density distribution of the deposited clusters obtained by measuring the maximum of the  $\text{Cu L}_3$  absorption intensity while moving the sample with respect to the X-ray beam.*

and an argon pressure of 6 mbar. At this conditions we measured a total cluster current of 8 nA at the metal plate before the mass selection and 80 pA of  $\text{Cu}_8$  at the substrate using a deposition energy of 3,5 eV/cluster. In the case of  $\text{Cu}_{50}$ , keeping the same nozzle with an aperture diameter of 4 mm, we used a power of 80 Watt, an aggregation length of 11 cm and a pressure of helium and argon

of 0,3 and 6,5 mbar, respectively. At the substrate we measured 15 pA applying a deposition energy of 4 eV/cluster. The Ar and He pressure are controlled by UHV dosing valves.

#### 4.1.7 UHV suitcase

The cluster-covered samples are transferred to a battery driven UHV suitcase that is mobile (Fig. 4.13) and that can be connected to diverse investigation machines at BESSY, such as our deposition chamber and the SURICAT photoelectron chamber at the optics beamline. The silicon substrate, having the

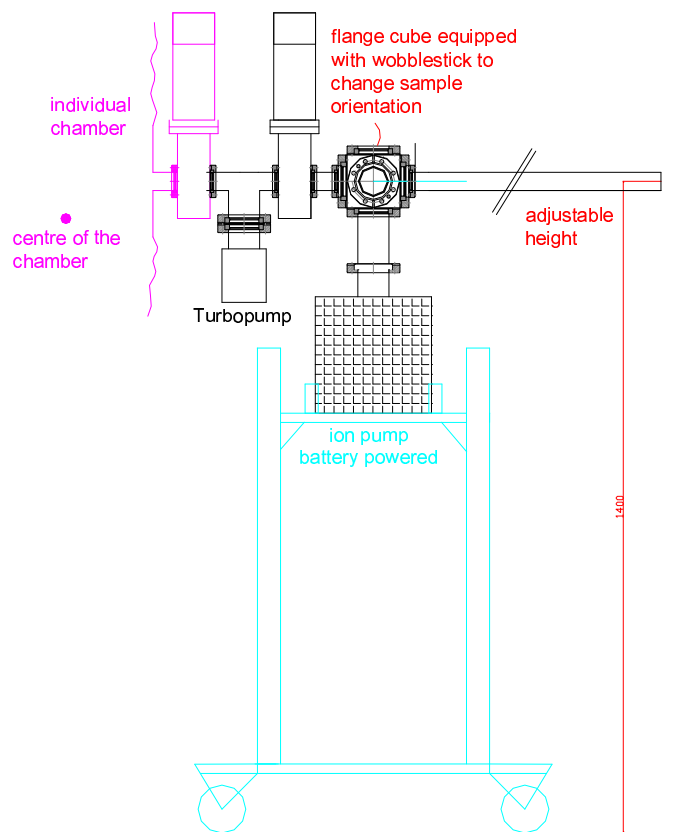


Figure 4.13: *UHV suitcase used to transfer our samples to the beamline [110].*

dimension of a square of  $1 \text{ cm}^2$ , is glued with a silver paste to a standard stainless steel Omicron sample plate. With a manipulator in the deposition chamber

the deposited samples are moved to a magazine (Fig. 4.14) that is fixed to the transfer rod of the suitcase. Closing the two valves which connect the deposition chamber with the transfer system and venting the vacuum tube in between, the suitcase can be removed and brought to the synchrotron to analyse the samples. In the suitcase the vacuum is made by a turbomolecular pump (Pfeifer TMU 071P, 601/s) placed between the two valves that gives a base pressure of  $10^{-9}$  mbar. During transportation the vacuum is kept by a Ion getter pump (Varian VacIon Plus 20) connected to a Pb-battery.

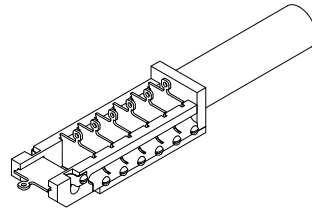


Figure 4.14: *Sample store*

## 4.2 Synchrotron radiation

### 4.2.1 Beamline

X-ray experiments on the deposited samples were performed at the Optics beamline PM4 at the synchrotron light source BESSY in Berlin. Synchrotron radiation has several advantages over conventional sources such as X-rays tubes (metallic anodes) or discharge lamps. The wavelength of synchrotron radiation is tunable and highly polarised (linear, circular). It allow to measure X-ray absorption spectra (NEXAFS, EXAFS) and to tune the photon energy in order to have an high photoionisation cross section for the core level of interest. Moreover the radiation is characterised by high brilliance, useful to study dilute samples. Synchrotron radiation is produced when a charged particle, with an energy  $E \gg m_0c^2$  (i.e. relativistic electrons), is deflected in a magnetic field. Different type of magnets are used in synchrotrons to generate radiation. Dipole magnets bend the electron path and generate X-rays along the tangent. Insertion devices (ID), a periodic structure of small magnets of alternating polarity, force the electrons to oscillate leading to a rise in X-ray intensity by several orders of magnitude. Depending on the magnetic field strength the ID is named either undulator or wiggler.

BESSY II has 240 m circumference with a total current in the storage ring of 250 mA and a final operation energy of maximal 1.7 GeV. In order to use the produced X-rays, optical elements direct and focus the radiation into the beamline and finally to the experimental end station. The wavelength can be selected by optical gratings.

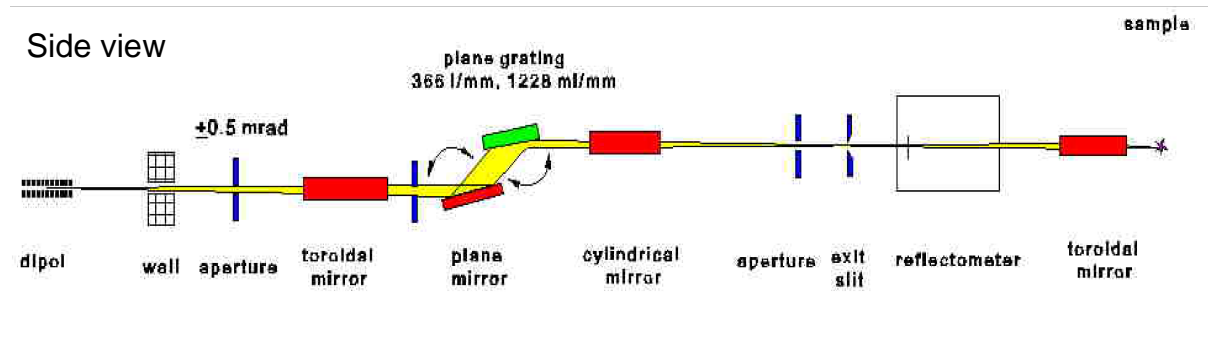


Figure 4.15: *Side view of the Optics beamline.*

Beamline PM4 (see Fig. 4.15) is a dipole beamline delivering photon energies between 25 and 1800eV. The first optical element is a water cooled toroidal mirror which is followed by a collimated plane grating monochromator, constituted of a plane mirror and a plane grating (1228 l/mm). The monochromatized light is vertically focussed by a cylindrical mirror onto the exit slit, that we fixed to an aperture of 400  $\mu\text{m}$ . After passing the reflectometer, the beam is horizontally focussed onto the sample plate in the experimental station SURICAT. The spot size is  $300 \times 90 \mu\text{m}^2$  and the photo flux at the sample is in the range of  $\sim 10^{10}$  phts/sec at 400  $\mu\text{m}$  slit width and 100 mA current.

## 4.2.2 The experimental station SURICAT

Photoemission and absorption experiments were performed at the end-station SurICat (Surface Investigation and Catalysis) shown in Fig. 4.16 located at the Optics beamline. The ultrahigh vacuum (UHV) system consists of a load lock (A in Fig. 4.16, base pressure:  $< 10^{-8}$  mbar) and of interconnected sample preparation (B, base pressure:  $< 2 \times 10^{-10}$  mbar) and analysis (C, base pressure:  $< 2 \times 10^{-10}$  mbar) chambers. An internal valve separates the chamber B from the C which is the  $\mu$ -metal shielded analyser chamber. Chamber A, that is also separated from B by a valve, serves as a load lock. In chamber A samples can be prepared without polluting the UHV chamber.

### loadlock and prep-chamber: the IGEL (A)

Chamber A is pumped by a 270 l/s turbo which has as roughing a membrane pump. It includes a manipulator for sample transfer (M1 in Fig. 4.17), a Cu-evaporator, a leak valve and a sample storage up to 3 samples. The pressure is  $3 \times 10^{-10}$  mbar. The IGEL is separated from the main prep-chamber by a gate valve that opens and closes with compressed air by turning a screw manually.

### main prep-chamber (B)

Chamber B is pumped by a 400 l/s turbo followed by a 70 l/s turbo and a roughing membrane pump, and by a Ti sublimation pump (no LN2 shield). The manipulator labelled M2 in Fig. 4.17 has differentially pumped rotation feedthrough (fed into the pumping system between the 2 turbos) and a second rotation. A Balzers Quadrupol mass-spectrometer up to 200 amu and a leak valve are included in this chamber.

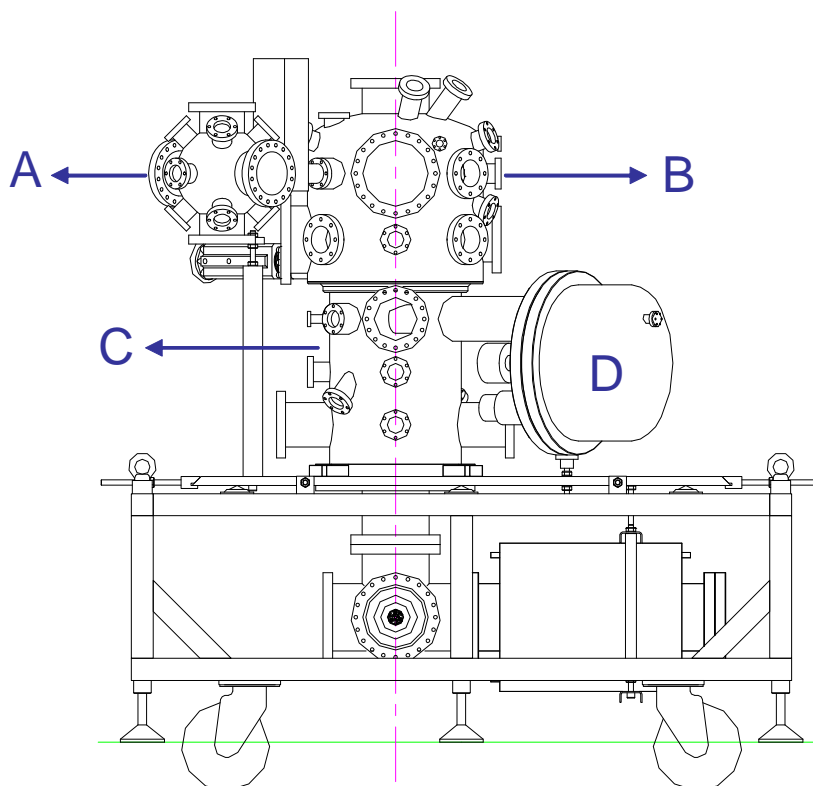


Figure 4.16: *Design of the SurICat chamber, A: Load lock and preparation chamber for possibly reactive or contaminating materials; B: "clean preparation" chamber with several analytical tools separated from B and C by valves, and C: analyser chamber with a Scienta SES100 electron energy analyser D.*

### **Analyser chamber (C) and electron spectrometer (D)**

In chamber C the standard pressure obtained with an ion getter pump without cooling is better than  $2 \times 10^{-10}$ . This chamber is equipped with the high resolution electron spectrometer Scienta SES 100 [111] (see Fig. 4.18) which measures the kinetic energy of the photoelectrons and is labeled with D in Fig. 4.16. The photoelectrons coming from the sample are collected and focused by an electrostatic lens system onto the entrance slit of the hemispherical energy analyser. The electron analyser is the part of the spectrometer which perform the electron energy dispersion. It is constituted of two concentric hemispheres

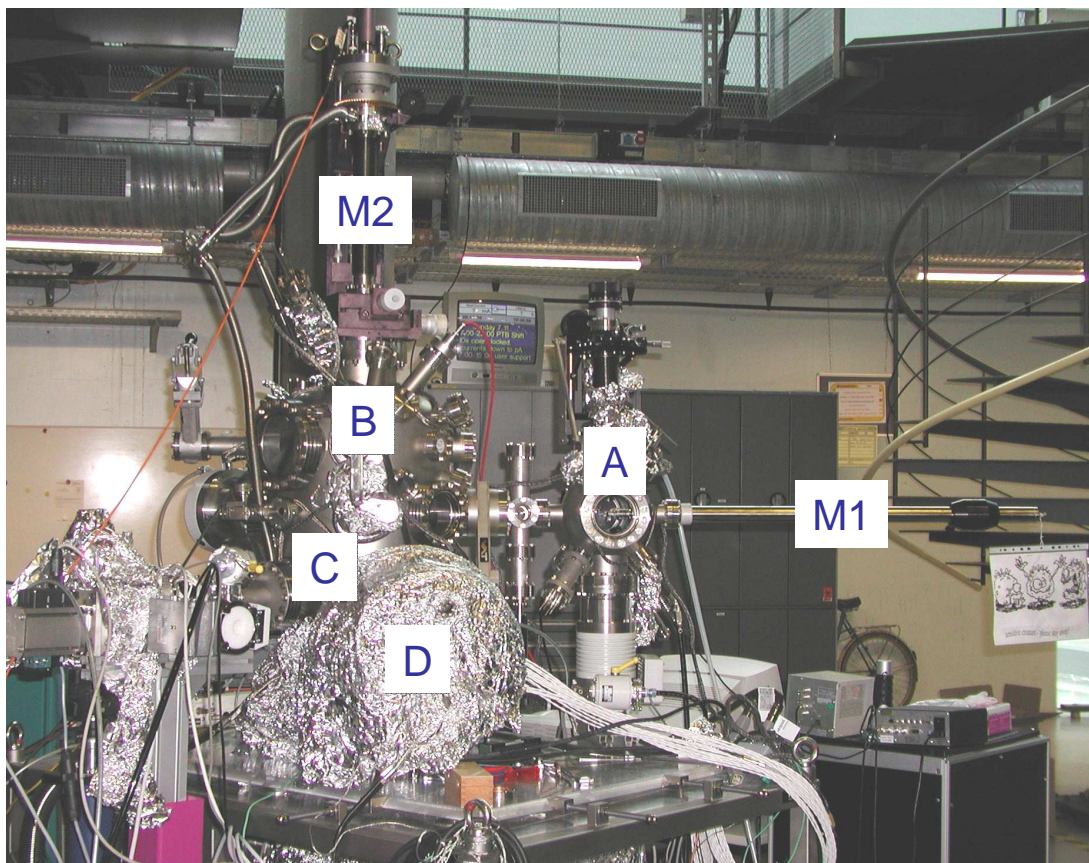


Figure 4.17: *Picture of the experimental station SURICAT. The two manipulators for samples transfer are labelled M1 and M2.*

with a mean radius of 100 mm and separated by 40 mm. A fixed voltage difference is applied between the two spheres (pass energy) during the acquisition of a spectrum. In this work we used a pass energy of 50 eV. The photoelectrons entering the analyser are bent with a bending radius which depends on the initial electron kinetic energy. Only the electrons with energy corresponding to the pass energy will be detected by the detectors at the exit slit of the analyser. By using the system of lenses placed before the entrance slit to accelerate or retard the photoelectrons, it is possible to scan a chosen energy interval. The detector system gives a two-dimensional image of the electrons. It is constituted by a field termination mesh placed immediately in front of the detector, two Multi-Channel Plates (MCP) and a phosphor screen. The MCP pair multiplies each incoming electron about a million times. This electron pulse is accelerated to the phosphor screen producing a light flash detectable by a camera. The electrical signal is then converted into an optical signal and passed with the help of optical fiber

on to a receiver. The pulses are counted and processed and the electron energy spectrum is displayed on the computer monitor.

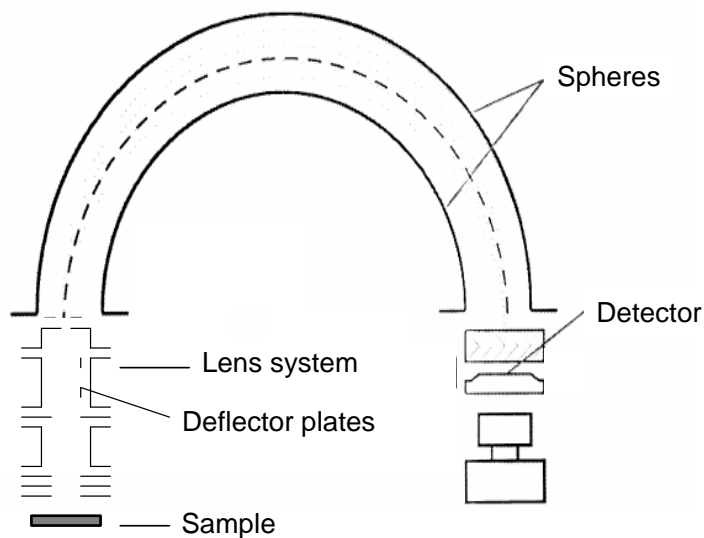


Figure 4.18: *Schemating drawing of the SES 100 electron spectrometer [111].*

### Sample transfer

The deposited samples prepared in our laboratory were transferred with the UHV suitcase to the experimental station by the use of an Omicron standard sample system. The suitcase was connected to the load lock and by using two manipulators, the one of the suitcase and the one labelled M1 in Fig. 4.17, the samples were transferred into the chamber A. With the manipulator M1 the samples were then transferred into the manipulator M2. This one was then moved down in order to reach the height of the analyser. The samples were measured with an angle of incidence of the light of  $45^\circ$ .



# Chapter 5

## Experimental results and discussion

### 5.1 Introduction

X-ray spectroscopy is particularly useful for the investigation of clusters in contact with a surface due to its element specificity. In this chapter we will present XPS and UPS results of the *Cu 2p*, *Cu 3p* and *Cu 3d* levels of various mass-selected copper clusters up to *Cu*<sub>70</sub> which were softly-landed onto a Si substrate. Additionally, XANES (*L*<sub>3</sub> edge) has been performed on the deposited clusters. Using a combination of XPS, NEXAFS and UPS data, the band gap of the deposited copper clusters has been approximated. Finally, in order to separate the contributions of the initial and final state effects as well as to determine the on-site Coulomb interaction energy, Auger measurements were performed.

### 5.2 XPS

#### 5.2.1 Survey

Figure 5.1 shows an XPS survey spectrum of a silicon substrate on which *Cu*<sub>7</sub> clusters were deposited. This spectrum has been taken with a nominal photon energy of 1150 eV and an electron analyser  $E_{pass}$  of 50 eV ( $\Delta E_{kin}=50$  meV). At  $h\nu=1150$  eV the monochromator resolution of beamline PM4 amounts to 1,4 eV at an exit slit width of  $400 \mu\text{m}^{-1}$  (screws setting 13,5 mm).

---

<sup>1</sup>It turned out that the experimental monochromator resolution at PM4 was double as well as the calculated nominal resolution given by the monochromator software. After rechecking and according to R. Follath (Bessy) the software in fact used an exit slit width which is a factor of two too large.  $400 \mu\text{m}^{-1}$  is now the corrected value, i.e.  $1/2$  the nominal software value.

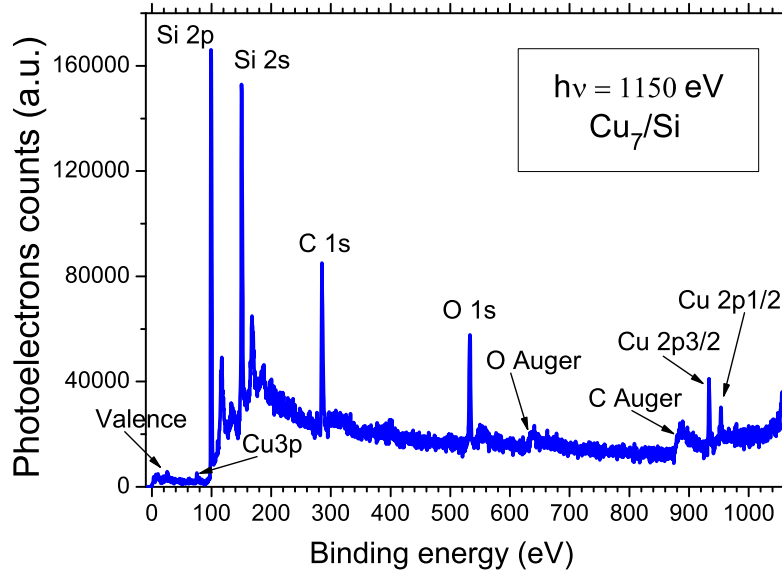


Figure 5.1: XPS survey plot of  $\text{Cu}_7/\text{Si}$  acquired with a photon energy of 1150 eV.

Probabilities of electron interaction with matter far exceed those of the X-ray photons, so while the mean free path length of the photons is of the order of micrometers, that of electrons is of the order of Ångström's only. Thus, while ionisation occurs to a depth of a few micrometers, only those electron that originate a Ångström below the solid surface can leave the surface without energy loss. These electrons produce the peaks in the spectra. Secondary electrons resulting from inelastic photoemission increasingly dominate the background at lower kinetic energy, i.e. at higher binding energy.

The relative intensity of the photoelectron peaks depends on the photoemission cross-section and the abundance of the element. Comparing the relative intensity of the  $\text{Si } 2p$  and  $\text{Cu } 2p$  peaks and considering that the photoionization cross section of  $\text{Cu } 2p$  at 1150 eV is about 30 times higher with respect to  $\text{Si } 2p$ , we estimate that the amount of Cu is about 1% of Si. More precisely, taking also into account the inelastic mean free electron path in Si at 1050 eV kinetic energy ( $\sim 2$  nm) [112], and an X-ray incidence angle of  $45^\circ$ , it results that the amount of deposited Cu is 7% of a Si (100) surface monolayer. This evaluated minimum (1%) and maximum coverage value (7%) agrees well with the cluster coverage independently deduced from the measured deposition current ( $\sim 1\%$ ) as

described in paragraph 4.1.5.

### 5.2.2 Silicon substrate

As substrate we used a p-type Si(100) wafer etched in HF solution before deposition. The doping of the silicon minimises charging problems of the clusters after photoemission. The effectiveness of the etching procedure is evident from Fig. 5.2, where the *Si 2p* peak at  $h\nu=1150$  eV is shown. The *Si 2p* peak of oxidised silicon at  $\sim 103$  eV is 100 times smaller than that of pure silicon. Considering that at this energy the inelastic mean free electron path is  $\sim 2$  nm, the thickness of the oxidised silicon is small enough to prevent macroscopic charging problems [73]. The green lines of Fig. 5.2 are two fitted Gaussian curves representing the spin-orbit split peaks  $2p_{3/2}$  and  $2p_{1/2}$ , respectively. During fitting the peak maxima have been fixed to the literature values 99,2 and 99,8 eV [113,114]. The area of the *Si 2p<sub>3/2</sub>* peak amounts to two times that of the *Si 2p<sub>1/2</sub>* peak. The resulting fitting curve fits well to the experimental data reproducing a maximum of the non-resolved *2p* peak at 99,5 eV in accordance with Himpsel *et al.* [115].

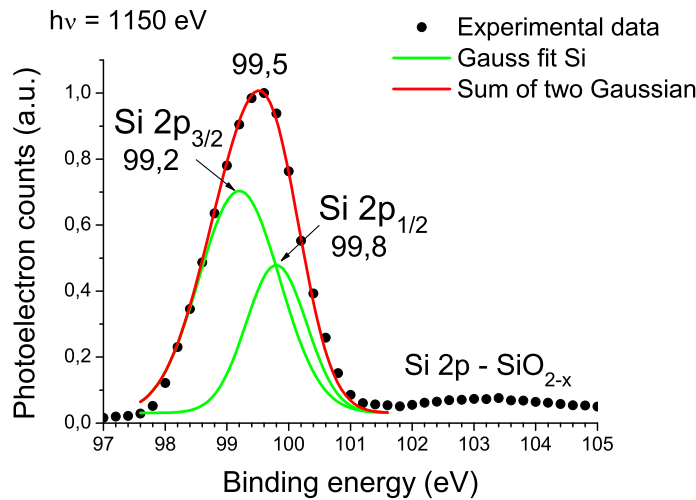


Figure 5.2: *Si 2p* peak (dots) acquired with a photon energy of 1150 eV. The green line shows a fit of the two spin orbit split peaks  $2p_{1/2}$  and  $2p_{3/2}$ , respectively. The sum of the fit is shown as red line.

Fig. 5.3 shows the valence band of the HF-etched Si-sample (blue line) taken at a photon energy of 200 eV with a monochromator resolution of  $\sim 0,3$  eV (exit

slit width  $400 \mu\text{m}$ )<sup>2</sup>. The pass energy of the electron analyser was  $E_{pass}=50 \text{ eV}$  ( $\Delta E \sim 50 \text{ meV}$ ). Between 1-2 eV the surface states  $S_1$  and  $S_2$  are clearly visible which are attributed to the surface states of the Si-dimers [116]. These peaks are sensitive to oxidation and are not seen for  $\text{SiO}_2$ . Still, some  $\text{O}_2$ -contamination of our etched Si-surface can be recognized by peak  $A_1$  and  $A_2$  which hints to about 1 ML adsorbed oxygen [116]. Note that the spectrum of our etched Si sample (blue line) is clearly different from a  $\text{SiO}_2$  layer for which no valence states are seen up to 5 eV (red spectrum).

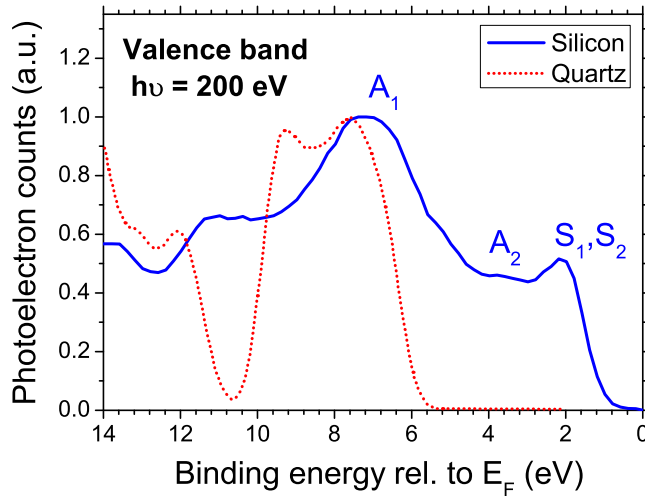


Figure 5.3: *Blue: Si valence band acquired with an X-ray energy of 200 eV. Red: Valence band spectrum of a  $\text{SiO}_2$  sample [117].*

### 5.2.3 Cu 2p

Fig. 5.4 a) exemplarily shows the  $\text{Cu } 2p$  photoemission spectrum of  $\text{Cu}_{10}$  in comparison with the spectrum of an evaporated Cu-bulk film. Both spectra were taken at a photon energy of 1150 eV. For the clusters the energy scale is calibrated using the simultaneously measured  $\text{Si } 2p$  peak of the substrate. The binding energy of the  $\text{Si } 2p$  maximum is calibrated with respect to the literature value of 99,5 eV [115]. The Cu bulk photoemission peak is calibrated with respect to the literature value of 932,5 eV [118].

<sup>2</sup>see footnote in paragraph 5.2.1

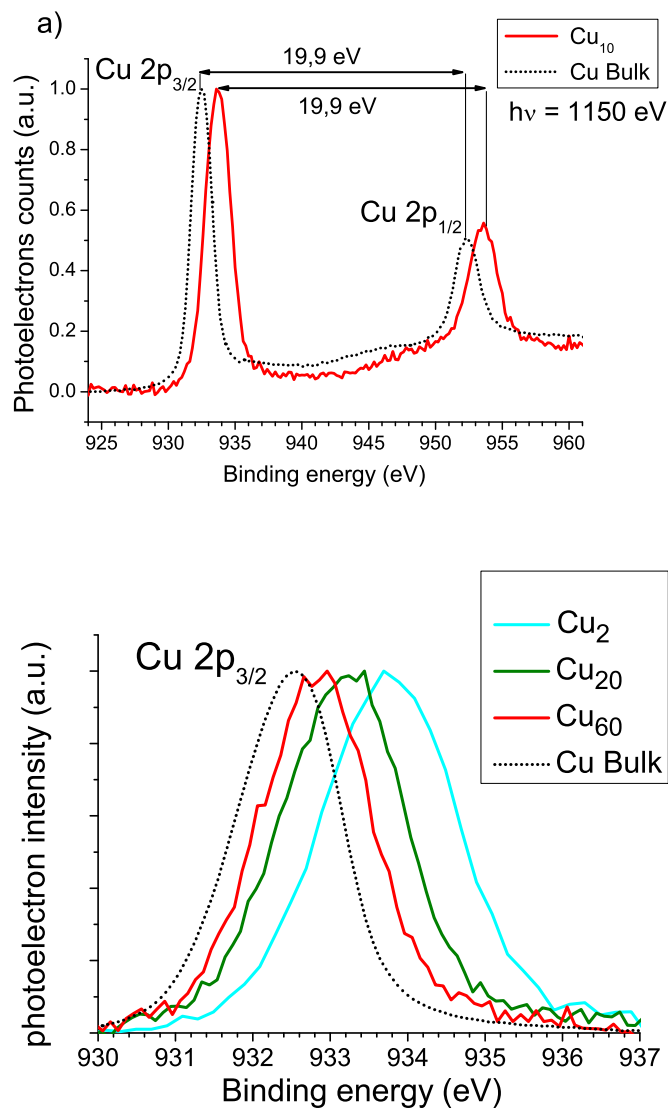


Figure 5.4: a):  $Cu\ 2p_{3/2}$  and  $Cu\ 2p_{1/2}$  peaks of  $Cu_{10}$  on Si and Cu Bulk. b):  $Cu\ 2p_{3/2}$  peak of some deposited copper clusters and of the bulk metal. A blue shift with respect to the bulk peak is observed for all clusters.

The two peaks of the  $Cu\ 2p$  level arise through spin orbit coupling with  $l = 1$  and  $s = \pm\frac{1}{2}$  (the total angular momentum is given by  $j = l + s$ ). The degeneration for each state is  $(2j + 1)$ . As  $j = \frac{1}{2}, \frac{3}{2}$ , the degeneration of the  $Cu\ 2p_{3/2}$  level is two times that of  $Cu\ 2p_{1/2}$ . This is the origin of the relative intensities of the two  $Cu\ 2p$  peaks. Note that the  $2p_{1/2}$  peak is broader than the  $2p_{3/2}$  peak

because of the occurrence of a  $L_2L_3M_{45}$  Coster-Kronig process which shortens the lifetime of the  $2p_{1/2}$  hole [119]. In this event, the  $L_2$  photohole is filled by an electron from the  $L_3$  shell accompanied by the emission of a  $M_{45}$  Auger electron. The spin-orbit coupling is identical to the bulk value, i.e. 19,9 eV, and does not change with cluster size, showing the atomic origin of the spin-orbit coupling. The small peak at  $\sim 946$  eV could be due to a shake-up effect, by which the cluster is left in an excited final state. This lowers the kinetic energy of the emitted core photoelectron.

As can be seen from Fig. 5.4 a) the XPS binding energy of  $Cu_{10}$  is clearly blue shifted with respect to Cu bulk. This is also true for all other clusters as shown in Fig. 5.4 b). Figure 5.4 b) shows the normalised  $Cu$   $2p_{3/2}$  peaks of several clusters in comparison with copper bulk. A clear blue shift of the binding energy with respect to the bulk metal is observed as well as a decrease of the binding energy with increasing cluster size.

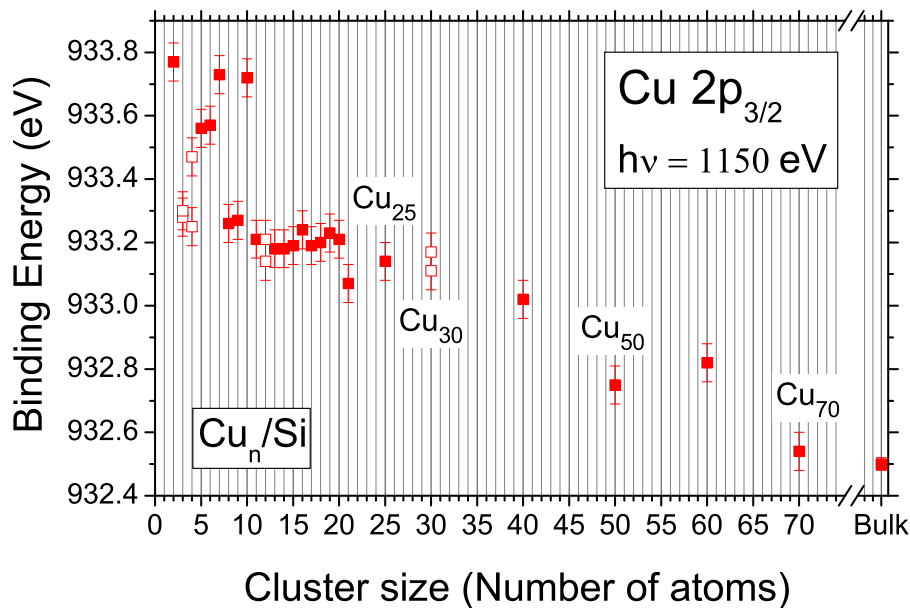


Figure 5.5:  $Cu$   $2p_{3/2}$  binding energy as function of cluster size. A general trend with increasing cluster size is obvious. Open squares indicate the values of two independent measurements on two different samples of equal cluster size.

Fig. 5.5 summarises the  $2p_{3/2}$  peak maximum of all measured clusters as

function of cluster size. The error bars are due to uncertainty in the evaluation of the  $Cu\ 2p$  and  $Si\ 2p$  peak maximum. The  $Cu_3$ ,  $Cu_4$ ,  $Cu_{12}$ , and  $Cu_{30}$  clusters

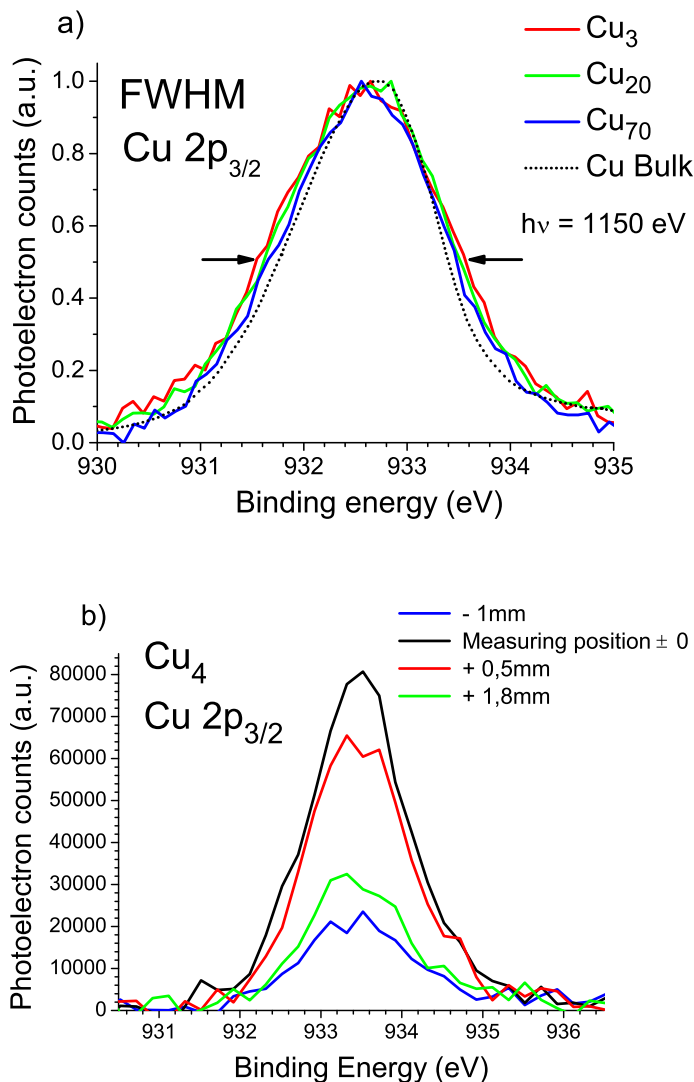


Figure 5.6: a):  $Cu\ 2p_{3/2}$  peak of  $Cu_3$ ,  $Cu_{20}$ ,  $Cu_{70}$  on  $Si$  and  $Cu$  bulk. The full width at half maximum decreases from 2 eV for  $Cu_3$  to 1,65 eV for the bulk. b):  $Cu\ 2p_{3/2}$  peak of  $Cu_4$  measured at different sample positions. Note that the binding energy does not change with decreasing cluster density. Only the intensity of the peak decreases with decreasing cluster density.

(open squares) have been measured for two different samples. Generally, the core binding energy tends towards the copper bulk value, in particular for clusters

>20 atoms. For smaller clusters no unique evolution is obvious and the binding energy changes arbitrarily from one cluster to the next. For clusters with more than 20 atoms the binding energy gradually decreases towards the bulk value. The bulk value is reached at a size  $> 70$  atoms. Unfortunately, the evolution for bigger clusters could not be studied during this work.

The increasing blue shift of the binding energy with decreasing cluster size is attributed to the change of the electron-hole Coulomb interaction and of the screening relaxation energy (see paragraph 5.2.6). The Coulomb interaction for an isolated metallic sphere of radius  $R$ , which is proportional to  $e^2/2R$  [120], decreases with increasing cluster size (see paragraph 5.2.6). Also the relaxation energy decreases with the size, as for a lower coordination number there is a reduced number of valence electrons available for screening the core hole.

Fig. 5.6 a) compares the line width of the  $Cu\ 2p_{3/2}$  peak of some clusters with the  $Cu\ 2p$  peak width of Cu-bulk. For a better comparison the peaks have been all shifted to the binding energy maximum of the bulk. The full width at half maximum (FWHM) of these peaks is for all clusters larger than the bulk value (1.66 eV). Up to  $Cu_{40}$  the width is 2 eV. For cluster sizes bigger than  $Cu_{40}$  the FWHM decreases slightly to 1,8. Similar to our observation, Jirka *et al.* [76] observed for copper clusters on carbon an increase of the FWHM of the  $Cu\ 2p_{3/2}$  peak with decreasing cluster size and they attributed this effect to a reduced screening of the core hole. Mason *et al.* [89] proposed as interpretation for the increased linewidth different absorption sites as reason for broadening. The high symmetry of the  $Cu\ 2p_{3/2}$  peak indicates that only neutral clusters are investigated. The charge left on a cluster after photoionisation is then neutralized before the next photoemission event. This means that the clusters are well coupled to the substrate.

Fig. 5.6 b) shows the  $Cu\ 2p$  peak of  $Cu_{12}$  which has been taken at four different spatial positions with respect to the center of the cluster deposition spot. This was achieved by moving the sample with respect to the X-ray beam. Considering that the cluster coverage changes from the center of the deposition spot to the periphery in a Gaussian-like manner, the XPS spectra were taken at different cluster densities when the sample was moved. As no change of the binding energy is observed as function of coverage density, we believe that the clusters are not agglomerated and are well separated from each other even in the center of the deposition spot. Only the intensity decreases when the X-ray beam hits a region of lower cluster density. The interaction of Cu with Si is predicted to be mainly covalent [34,121]. Therefore the bonding seems to be strong enough so that at room temperature the clusters stick on the surface and do not migrate and agglomerate.

### 5.2.4 Cu 3p

Fig. 5.7 a) shows the  $Cu$  3p peaks for  $Cu_{17}$  and Cu-Bulk. The spectra

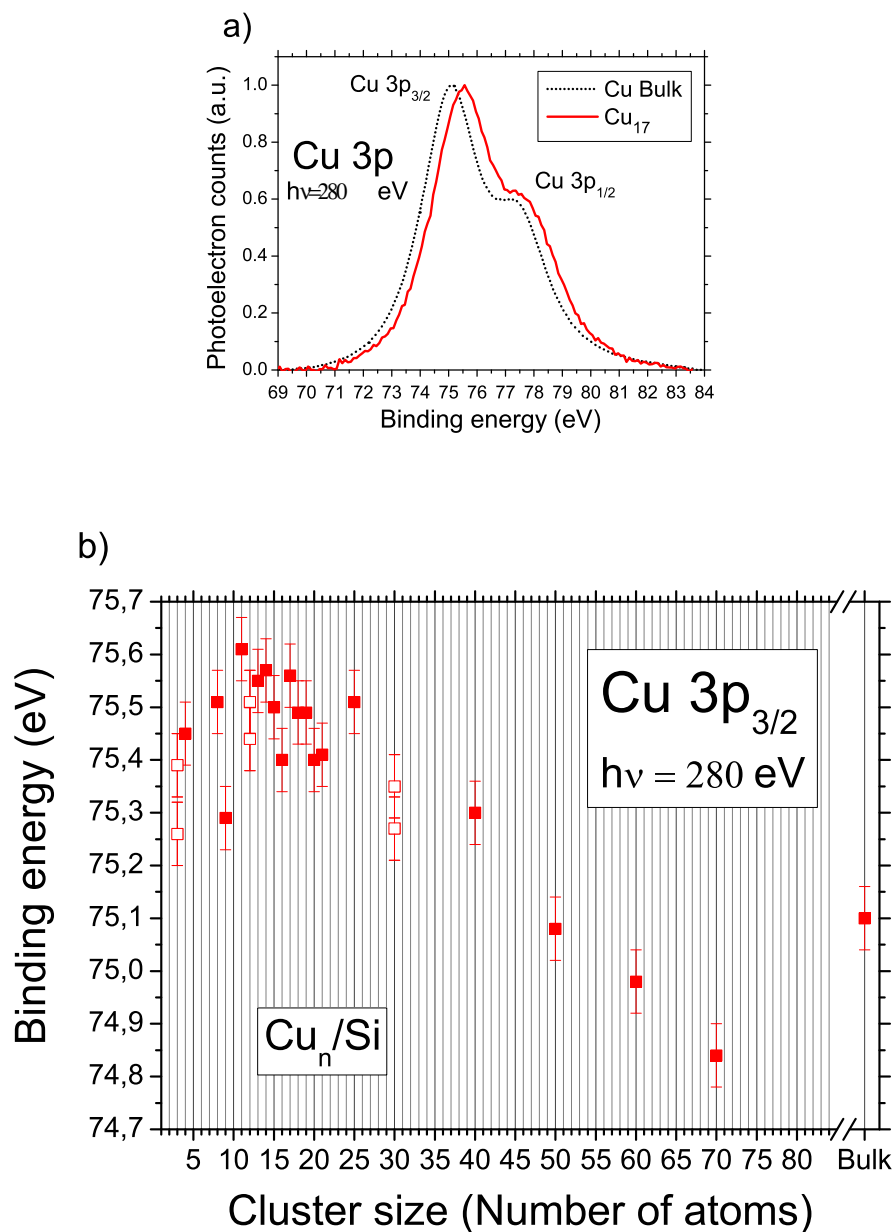


Figure 5.7: a): The  $Cu$  3p peak of  $Cu_{17}$  on  $Si$  in comparison with  $Cu$ -bulk. b):  $Cu$  3p<sub>3/2</sub> binding energy as function of cluster size. The empty squares show the results for two different samples.

have been taken with an analyser  $E_{pass}$  of 50 eV ( $\Delta E_{Kin} \sim 50$  meV) and a photon energy of 280 eV, as at this energy the cross-section is about one order of magnitude higher than at  $h\nu=1150$  eV [122]. At  $h\nu=280$  eV and exit slit width of  $400 \mu\text{m}$ <sup>3</sup> the beamline resolution is  $\sim 0,4$  eV.

For the energy calibration we refer to the *Si*  $2p_{3/2}$  peak at 99,2 eV [113]. The *Cu*  $3p_{3/2}$  value for copper bulk (75,1 eV) has been taken from Fuggle *et al.* [118]. Similar to the  $2p$  level, a positive ESCA shift is observed for all measured clusters. The shift is larger (ca. 0,5 eV) and non scalable for sizes up to 15 atoms and steadily decreases with increasing cluster size (see Fig. 5.7 b)). The binding energy approaches the bulk value at around 50 atoms and becomes even smaller for bigger sizes. This effect could be attribute to the interaction of the clusters with the substrate, i.e. an initial state effect and/or extra atomic relaxation. The spin-orbit splitting of the *Cu*  $3p$  peak is clearly resolved and is identical to the bulk, i.e. it does not depend on the cluster size (see Fig. 5.7 a)).

### 5.2.5 Cu 3d

A *Cu*  $3d$  valence photoelectron spectrum is exemplarily shown in Fig. 5.8 a) (red full line) together with the valence band spectrum of Cu-bulk (dotted line). Due to the low cluster coverage the Si valence bands are superimposed with the cluster spectrum. Therefore the valence band spectrum of a clean Si-sample is shown for comparison as blue line. All spectra have been recorded at  $h\nu=200$  eV with an analyser  $E_{pass}$  of 50 eV. At an exit slit width of  $400 \mu\text{m}$  the beamline resolution is  $\sim 0,3$  eV while the kinetic energy resolution of the energy analyser amounts to  $\sim 50$  meV. The Si spectrum and the  $3d$  cluster spectrum have been normalised to the intensity of the  $A_1$  peak (see Fig. 5.8 a)). The binding energy refers to the Si-peak  $A_1$  which has a binding energy of 7,3 eV [116]. The binding energy of the copper bulk spectrum is directly given by the difference between the Fermi level and the maximum of the  $3d$  band of the measured Cu-bulk sample.

The valence states of the Cu-clusters are clearly enhanced between 2-5 eV with respect to the valence band features of Si. We attribute the enhanced signal to the *Cu*  $3d$  band which is blue shifted by ca. 1,5 eV with respect to Cu-bulk. In Fig. 5.8 b) the difference spectra of *Cu*<sub>20</sub> is shown in comparison with the bulk spectrum, i.e. VB(Cu)-VB(Si).

In Fig. 5.9 the *Cu*  $3d$  binding energies of all measured clusters are compiled as a function of cluster size. Two main regions can be distinguished. For cluster sizes smaller than *Cu*<sub>30</sub> no obvious trend is discernible. For bigger clusters the binding energy slowly decreases with increasing cluster size. Interpolating the

---

<sup>3</sup>see footnote of paragraph 5.2.1

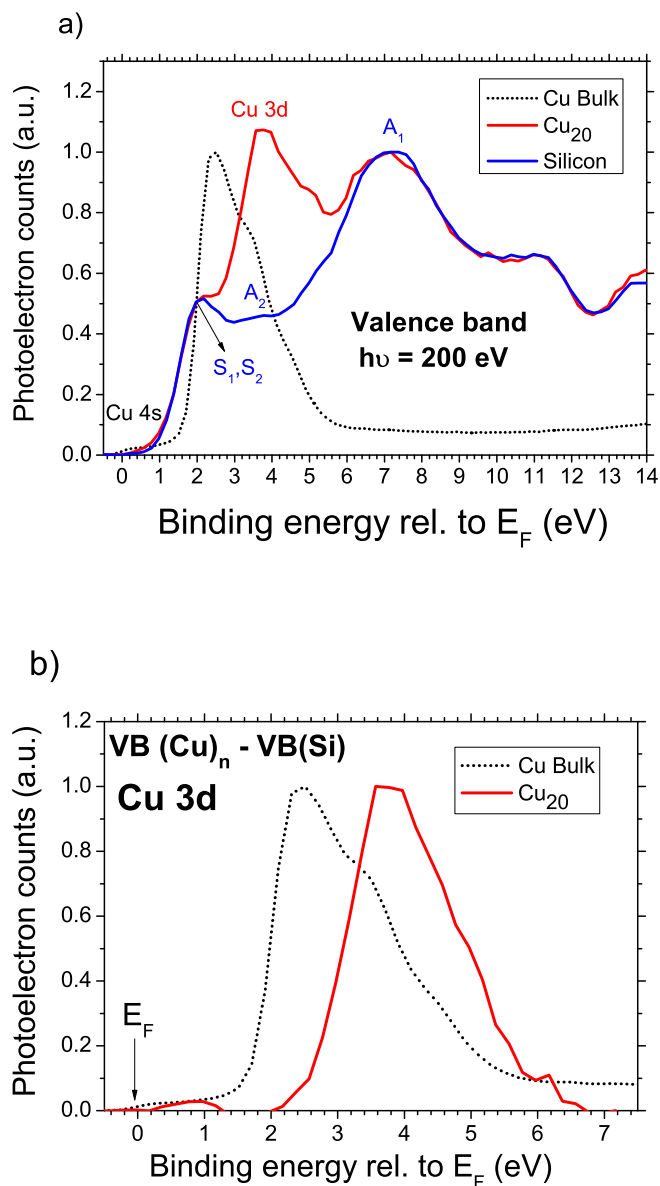


Figure 5.8: a): Valence band spectrum of Cu<sub>20</sub> (red), Cu-bulk (dotted) and the Si substrate (blue). b): The Cu 3d valence peak of Cu<sub>20</sub> after the subtraction of the substrate signal in comparison with the valence band spectrum (VB) of Cu-bulk.

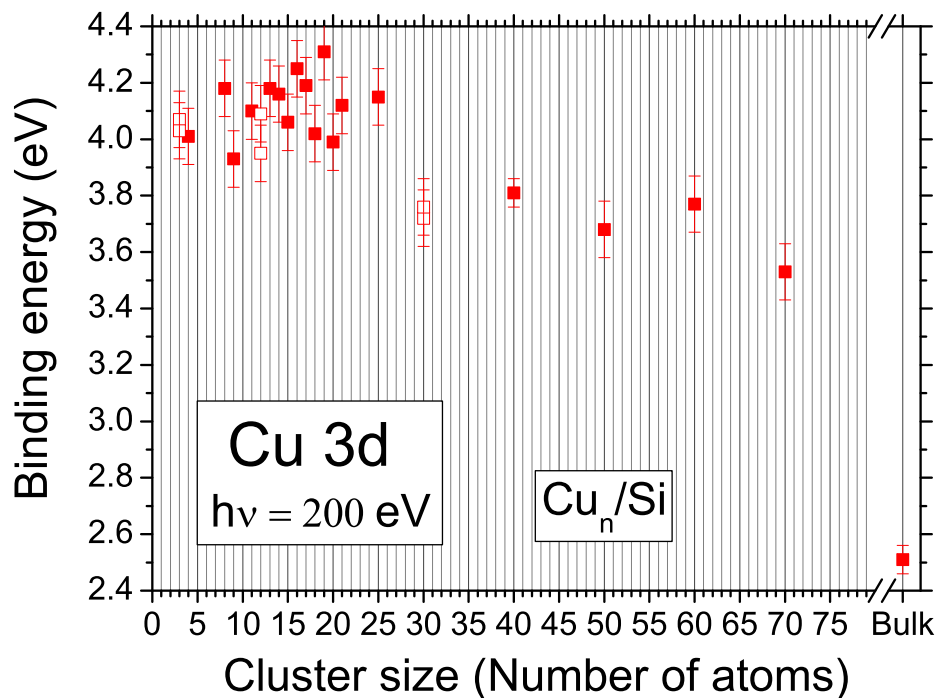


Figure 5.9: *Cu 3d binding energy as a function of cluster size. The open squares represent the results for two different samples of equal cluster size.*

data with a line starting at  $Cu_{30}$  we find that the bulk value is approximately reached at a cluster size of ca. 230 atoms. Photodetachment spectra of free Cu-cluster anions show a similar trend for the 3d band. The binding energy of the 3d level converges towards the bulk value with increasing cluster size and convergence for free Cu clusters is reached at ca. 250 atoms [17]. In contrast to the deposited clusters, however, the convergence starts at very small clusters while for the deposited clusters the 3d binding energy is nearly constant up to 25 atoms. This hints to an interaction of the substrate and a partial hybridisation with the Si-substrate which seems to pin the 3d level to a particular binding energy.

### 5.2.6 Comparison of the levels and 1/R plot

Fig. 5.10 summarises the binding energy shift of the clusters with respect to Cu-bulk, i.e. the ESCA shift, for the levels  $Cu\ 2p$ ,  $Cu\ 3p$  and  $Cu\ 3d$  as function of size. Common to all three levels is that all orbitals show a blue shift with respect to the bulk.

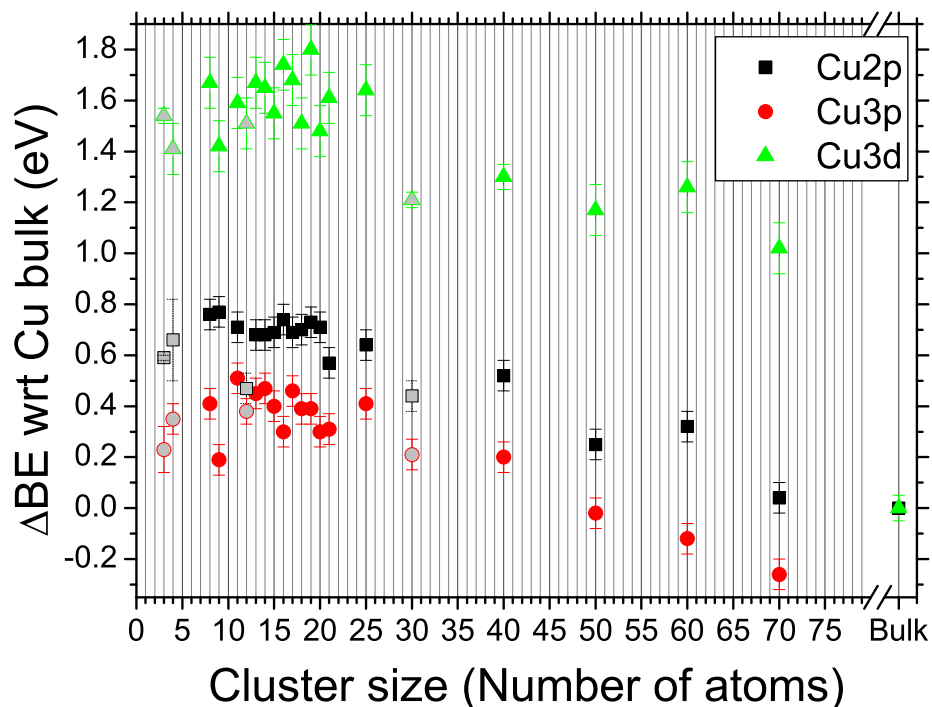


Figure 5.10: *Difference of the orbital binding energy  $BE$  of the clusters with respect to (wrt) Cu-bulk for the  $Cu\ 2p$ ,  $Cu\ 3p$  and  $Cu\ 3d$  level, respectively, where  $\Delta BE = BE_{cluster} - BE_{bulk}$ . The grey filled symbols show the mean values of two measurements on two distinct samples. The error bars are evaluated by error propagation.*

While the evolution of the core binding energy shift is similar to each other they behave clearly different with respect to the evolution of the valence band shift ( $3d$ ). For the latter the shift is not only much larger (up to 1,5 eV), but the convergence towards the bulk is much less pronounced as that of the core orbitals. The smaller shift of the core orbital is attributed to the core hole

screening. Moreover, the core binding energy shift converges towards the bulk value somewhere between 50 and 100 atoms while for 3d it is approximately reached at 230 atoms only (see paragraph 5.2.5).

The binding energy is defined as the difference energy between the initial and final state, i.e. the difference of the neutral cluster and the singly charged cluster left after photoemission. On the other hand, the ionisation potential  $IP$  is defined as the energy required to remove an electron from the cluster to infinity. Thus the ionisation potential of a particular state is given by the sum of the electron binding energy  $E_B$  and the work function  $W$ :

$$IP(R) = E_B(R) + W_R. \quad (5.1)$$

$$IP(\infty) = E_B(\infty) + W_\infty. \quad (5.2)$$

where  $E_B(\infty)$  and  $W_\infty$  are the binding energy and the work function relative to the bulk material, respectively. Within the liquid drop model the clusters are approximated as conductive spheres ( $R$ =radius of cluster sphere) on which a charge is smeared out over an infinitesimal thin surface. For a metallic sphere it follows [28]:

$$IP(R) = W_\infty + \left( A \times \frac{e^2}{4\pi\epsilon_0 R} \right) \quad (5.3)$$

$A$  is a factor which has been found to be 1/2 in classical electrostatic and 3/8 if quantum effects are considered [123]. Equation 5.3 has been reported to be in agreement with experimental measurements on free sodium, silver and potassium clusters [29, 124, 125].

If we generalise eq. 5.3 to the case of core electrons we get

$$IP^{Core}(R) = E_B^{Core}(\infty) + W_\infty + \left( A \times \frac{e^2}{4\pi\epsilon_0 R} \right) \quad (5.4)$$

For electrons at the Fermi level eq. 5.4 is equal to eq. 5.3 as there  $E_B^{core}(\infty) = E_B^{Fermi} = 0$ . It follows in analogy to eq. 5.1

$$IP^{Core}(R) = E_B^{Core}(R) + W_R. \quad (5.5)$$

If we replace in eq. 5.5 the relation between the work function  $W_R$  of a particle of size  $R$ , and the one of the bulk  $W_\infty$  as given by Halas [28],

$$W_R = W_\infty - \left( \frac{1}{8} \times \frac{e^2}{4\pi\epsilon_0 R} \right) \quad (5.6)$$

we get the following expression for the ionisation potential:

$$IP^{Core}(R) = E_B^{Core}(R) + W_\infty - \frac{1}{8} \times \frac{e^2}{4\pi\epsilon_0 R}. \quad (5.7)$$

In our experiment the clusters are deposited on a substrate which itself is in electrical contact with the spectrometer. Thus the electron binding energy is measured instead of the IP. Subtracting eq. 5.7 from 5.4 it results for the binding energy:

$$E_B(R) = E_B(\infty) + (A - \frac{1}{8}) \times \frac{e^2}{4\pi\epsilon_0 R}. \quad (5.8)$$

If the cluster radius  $R$  is in  $\text{\AA}$  and  $E_B$  in eV then eq. 5.8 becomes:

$$E_B(R) = E_B(\infty) + \frac{C}{R(\text{\AA})}. \quad (5.9)$$

where  $C=9$  for  $A=1/2$  and  $C=7,2$  for  $A=3/8$  ( $=0.375$ ). The term  $C/R(\text{\AA})$  represents the increase of the electron binding energy of the particle with respect to the bulk. This is due to the Coulomb interaction between the photoelectron and the positive charge left behind on a spherical cluster droplet. Thus plotting  $E_B(R)$  versus  $1/R$  a linear dependence results which converges towards the binding energy of the bulk with increasing  $R$ .

Fig. 5.11 shows the binding energy of the measured  $3d$ ,  $2p$  and  $3p$  orbitals as function of  $1/R$ . The dashed red and blue lines represents the calculated binding energy as deduced from the liquid drop model. The red line has been calculated using as coefficient  $A=1/2$ , the blue with  $A=3/8$ , respectively.  $R$  is the radius of a spherical Cu cluster and is given by  $R = N^{1/3} \times r$  [17], where  $r = 1,4 \text{\AA}$  is the Wigner-Seitz radius of bulk copper (fcc) [126].

The binding energy of the  $3d$  valence band is in reasonable agreement with the liquid drop model for a size  $\geq 13$  atoms (panel *a*). The general deviation towards lower binding energies can be explained by the fact that the clusters are in contact with a rather conducting surface while the drop model is deduced for a perfectly isolated metallic sphere in vacuum. So, in our experiment, the ionic charge left after photoemission is partially compensated by the substrate. Moreover the bonding of the copper with the silicon atoms is calculated to be largely covalent with a higher electron density on the metal atoms [34]. In other words the photoelectron does not see the full positive charge left after photoemission and due to the partial negative electron density around the metal atoms the electron binding energy in the Cu atoms in contact with the Si-surface should be reduced.

Fig. 5.12 compares the  $3d$  detachment energies of free Cu-clusters with the

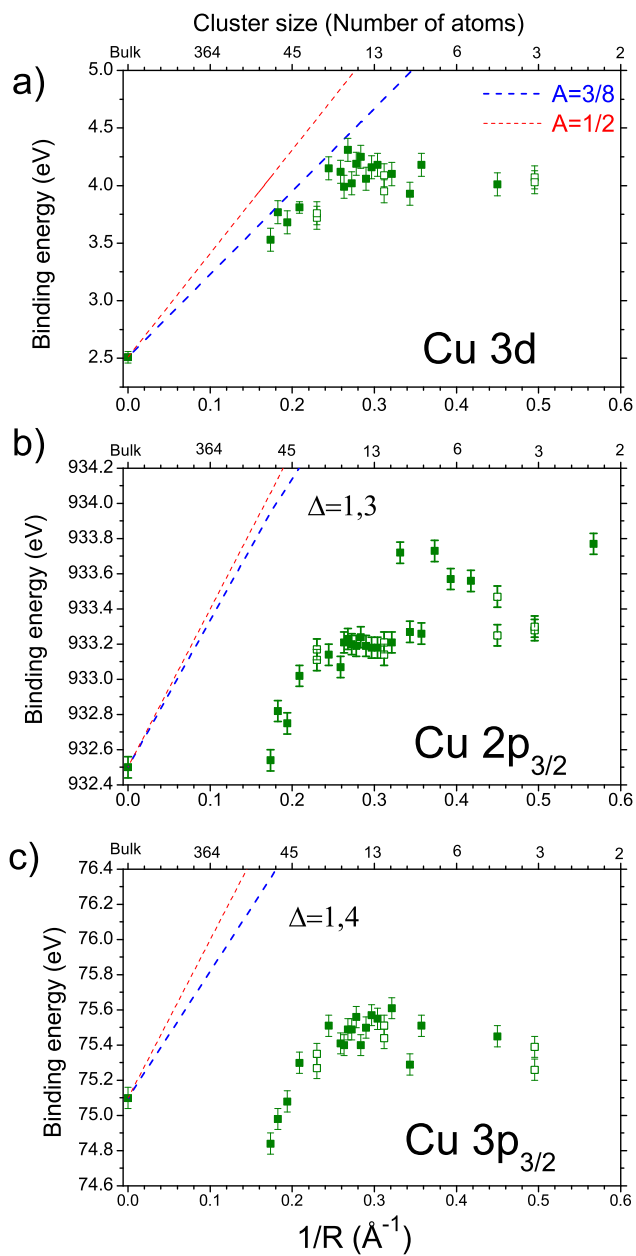


Figure 5.11: The binding energy of valence (a) and core orbitals (b,c) of deposited Cu clusters versus  $1/R$ . The dashed blue line represents the ionisation potential versus inverse clusters radius as calculated by the liquid drop model considering the maximum (red) and minimum (blue) value of  $A$  as found in literature for free clusters.

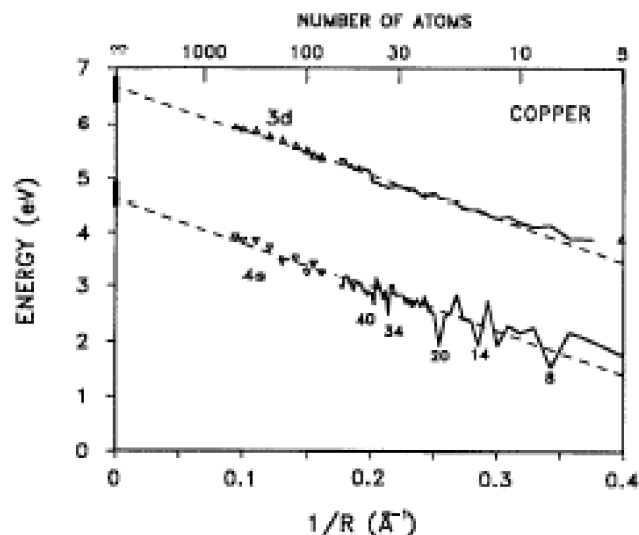


Figure 5.12: Comparison of the 3d binding energies of free copper clusters with the liquid drop model. Adapted from Taylor et al. [17].

liquid drop model [17, 44]. For gas phase Cu-clusters the liquid drop model fits perfectly the 3d binding energy of the clusters assuming a value of  $A=0,55$  [17]. That in our measurements the model fits only for larger cluster can be explained by the fact that a spherical geometry is formed for a size  $\geq 13$  atoms (see also paragraph 5.3.1) while smaller are nearly distorted by the interaction with the substrate [36, 53], e.g. the clusters might form flat objects.

In contrast to the 3d valence orbital the binding energy of the core orbitals are clearly off the line representing the liquid drop model (panel b), c)). This is due to the fact that the liquid drop model assumes a well delocalised charge distributed over the surface of a sphere. This, of course, is valid for the 3d orbital rather than the 2p and 3p core orbital, respectively. The latter are well localised which leads to a strong screening of the corresponding core hole. Therefore the binding energy of the core orbitals is reduced by strong final state effects which are negligible for the valence orbitals. Nevertheless the evolution should tend towards the bulk value for  $R \rightarrow \infty$ . For the core levels, however, the bulk value is reached at much smaller R-value than expected from the liquid drop model (see dashed line in Fig. 5.11). The Cu 3p<sub>3/2</sub> binding energy of Cu<sub>60</sub> and Cu<sub>70</sub> is even lower than the bulk value. This is a strong hint for extra-atomic relaxation and/or initial state interaction by the substrate which is not present in the pure Cu-metal. Therefore the evolution of the core binding energy in the medium size range tends towards a certain Cu-Si binding energy which is lower than the

pure Cu-bulk value. This hints to a partial charge transfer from Si to Cu which confirms the predictions by Pacchioni *et al.* [34].

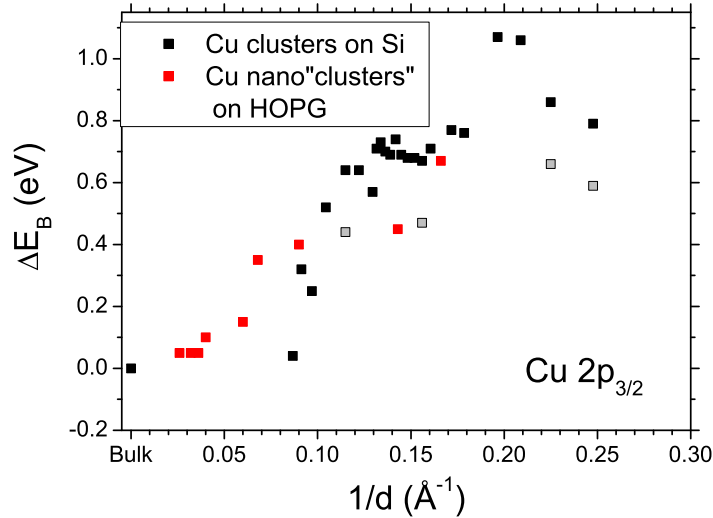


Figure 5.13:  $Cu\ 2p_{3/2}$  binding energy shift relative to the bulk value as function of  $1/d$ , where  $d$  is the cluster diameter. The black and grey squares are the results of this work while the red data points are from Yang *et al.* [85] (The grey squares indicate the  $Cu\ 2p$  mean binding energy of the clusters  $Cu_3$ ,  $Cu_4$ ,  $Cu_{12}$  and  $Cu_{30}$  given as the average of two independent measurements).

With increasing cluster size, of course, the relative influence by the substrate must become smaller so that the binding energy is expected to progress through a minimum before it converges towards the bulk value for clusters  $>70$  atoms.

Fig. 5.13 compares our ESCA shift ( $BE(2p)_{cluster} - BE(2p)_{Bulk}$ ) of the  $Cu\ 2p_{3/2}$  level with the data of Yang *et al.* [85]. In the work of Yang *et al.* agglomerated atomic nano islands are obtained through copper evaporation onto highly-ordered-pyrolytic-graphite (HOPG). Our data continue the data of Yang *et al.* towards smaller cluster sizes, especially in the range  $d < 1$  nm. Both Yang *et al.* [85] and our data show a positive ESCA shift which converges towards the bulk value with increasing cluster size. However, on Si the binding energy of the clusters converge more rapidly towards the bulk value than on HOPG. This hints to a stronger interaction of the Si-substrate with the clusters, e.g. the substrate helps to screen the core hole and/or neutralizes more efficiently the Coulomb charge of the photohole than HOPG does.

## 5.3 XANES

### 5.3.1 XANES on deposited Cu clusters

Fig. 5.14 shows the X-ray absorption spectra (Cu- $L_3$  edge) of some representative Cu-clusters in comparison with copper bulk. All spectra were measured by collecting the total photocurrent of the sample using a picoammeter (Keithley). Each spectrum represents a sum of five scans with a total acquisition time of about half an hour (151 channels, 2 sec per channel). At an exit slit of  $400 \mu\text{m}$ <sup>4</sup> the monochromator resolution at 935 eV is  $\sim 1,2$  eV.

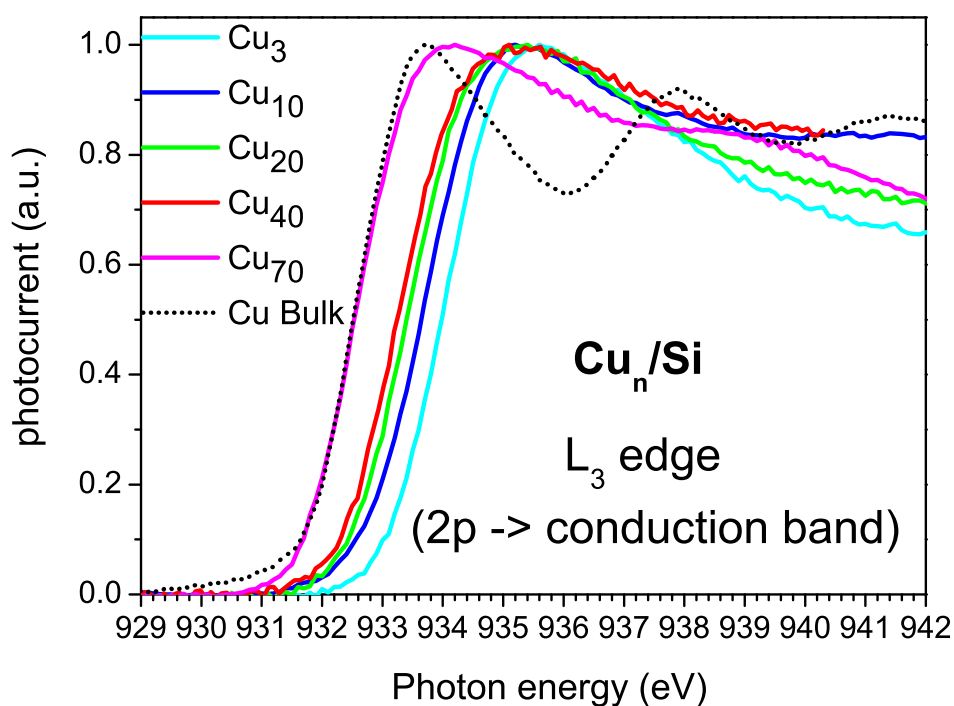


Figure 5.14:  $L_3$  absorption edge of deposited Cu-clusters compared to that of Cu-bulk. In the case of the clusters the  $L_3$  edge appears at a higher absorption energy and with increasing cluster size the  $L_3$  absorption edge converges towards the position of the bulk.

The spectrum of the bulk was measured on a freshly prepared Cu-film. In

<sup>4</sup>see footnote of paragraph 5.2.1

order to compare the various absorption spectra the sample current was divided by the photocurrent of the last beamline mirror in front of the sample to correct against possible absorption features by the beamline and irregularities of the ring current. As the beamline optics, however, does not absorb in the Cu region almost no difference between the sample current and the divided spectra was apparent. After division, a linear background has been fitted to the pre-edge region (930-934) which was subtracted from the absorption curve (see Fig. 5.15). Finally the spectra have been normalised to the maximum intensity.

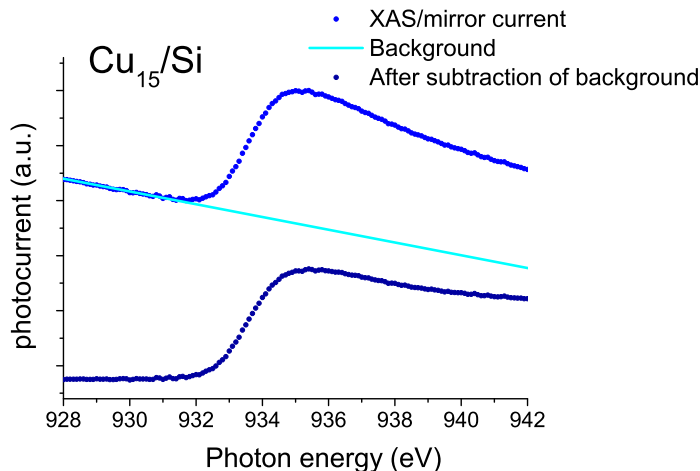


Figure 5.15: Original X-ray absorption spectrum of  $Cu_{15}$  (upper spectrum) and background corrected XAS spectrum (lower spectrum) after subtraction of a linear background.

In all cluster spectra, a step-like function is observed at the  $L_3$  edge which is clearly shifted to a higher absorption energy with respect to the bulk [54]. For the discussion of the near edge features the origin of the energy scale is set at the Fermi level of Cu-bulk. The energy necessary for the transition of an electron from a certain level to the Fermi level is equal to the inflection point of the absorption edge jump, i.e. at 50% of the edge height. At this point the  $2p_{3/2}$  core binding energy [118] and  $L_3$  edge of Cu-bulk are equal. i.e. 932,5 eV, as expected for a metal. As a general trend we observe that the  $L_3$ -absorption energies converge towards the bulk value with increasing cluster size. A maximum blue shift of 1,23 eV is observed for  $Cu_8$  while for  $Cu_{70}$  the absorption edge is very similar to the bulk value. Nevertheless, the shift cannot be scaled by any law but scatters in a non-scalable manner from one cluster to the next as seen in the compilation

plot of all clusters (Fig. 5.16). For small clusters the edge scattering is arbitrary and much more pronounced (between 0,5 eV and 1 eV) than for bigger sizes. For smaller sizes, in fact, each atom counts and the particular geometric structure of each cluster has a strong effect on the electron energy levels. Generally, the blue shift can be explained by a reduced final-state screening [89] due to a lower atomic coordination number and a missing metallicity of the Cu-clusters. The missing metallicity can be verified by the presence of a semiconducting HOMO-LUMO gap which has been measured for free Cu-clusters by laser photodetachment [44] (see Chapter 2). The HOMO-LUMO gap for the deposited clusters is discussed in paragraph 5.3.2.

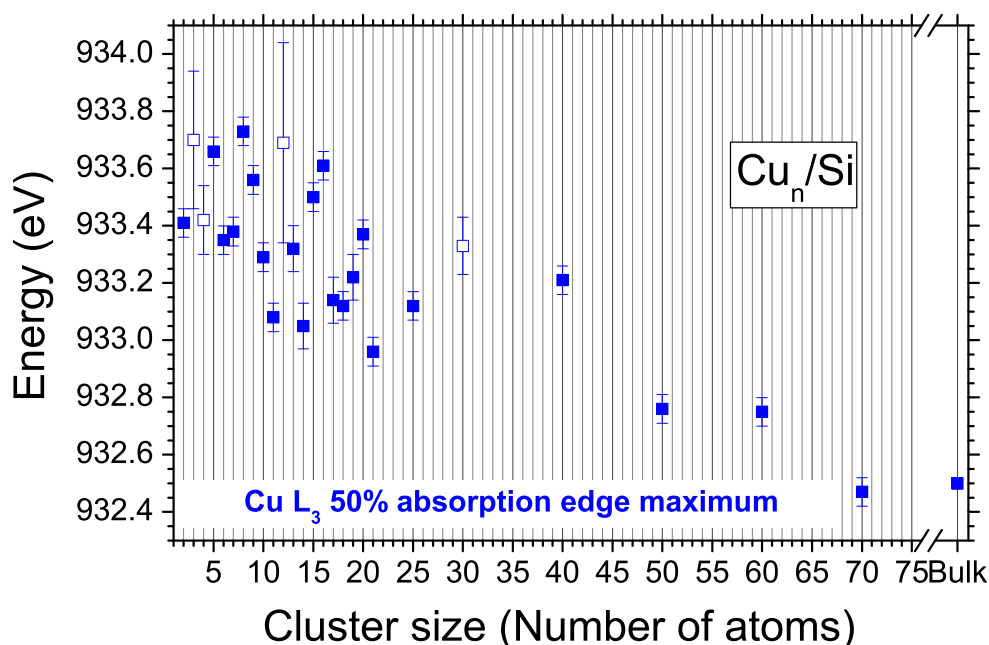


Figure 5.16:  $L_3$  absorption energy for all measured clusters (energy taken at 50% absorption edge height). With increasing cluster size the  $L_3$  absorption energy is approaching the one of Cu-bulk. The empty squares indicate mean values of two independent measurements. The error bars are derived from error propagation.

In contrast to the  $L$ -absorption spectra of transition metal clusters such as Ni, Pt and Fe no sharp “white line” is observed for the Cu clusters and Cu-bulk. Generally, the absorption spectra of open  $d$  shell metals, like Ni ( $d^8s^2$ ) [127] or Pt ( $d^9s^1$ ) reveal a sharp absorption maximum below the XPS ionisation threshold (“white line”) which indicate the presence of  $d$  vacancies. Instead, the absorption

edge of the Cu cluster is rather step-like. From this, we conclude that the clusters have a nominal closed  $3d$ -shell, similar to the bulk. Though a nominal closed  $d$ -shell is discussed for Cu bulk, the  $L_3$  absorption edge is nevertheless governed by a  $2p \rightarrow 3d$  transition, due to a residual hybridisation between the  $3d$  and  $4s$  orbitals [121] and a fairly enhanced cross section of the  $d$ -orbitals with respect to the empty  $4s$  level ( $3d/4s \approx 400$ ).

Similar to the XPS spectrum the  $L_3$  and  $L_2$  absorption edges of the Cu clusters are separated by  $\sim 20$  eV. The splitting arises by spin orbit coupling, i.e.  $2p_{1/2} \rightarrow 3d_{3/2}$  and  $2p_{3/2} \rightarrow 3d_{5/2}$ , respectively. Representative for all clusters a full  $L$ -edge absorption spectrum of  $Cu_{10}$  is shown in Fig. 5.17.

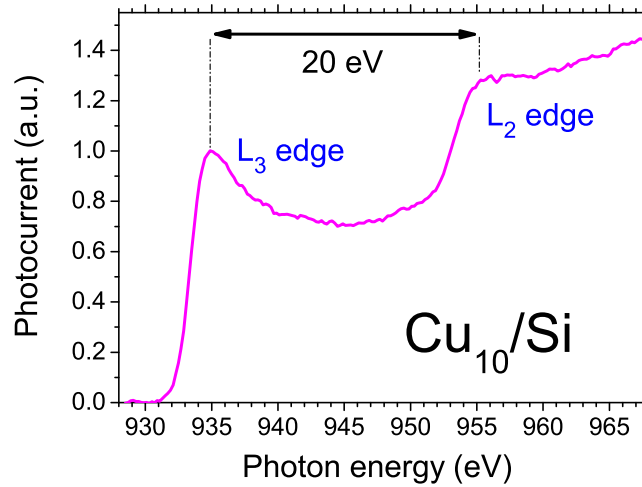


Figure 5.17:  $L_2$  and  $L_3$  absorption edges measured for deposited  $Cu_{10}$ . The energy difference between the two spin-orbit split absorption edges is 20 eV.

Not only the  $L$ -edge threshold energy of the clusters is different but also the fine structure behind the absorption edge shows clear differences with respect to the bulk.

Fig. 5.18 shows the measured absorption spectra of deposited  $Cu_3$ ,  $Cu_{50}$ ,  $Cu_{60}$ ,  $Cu_{70}$ . The bulk spectrum (black dotted) reveals two additional absorption features beyond the  $L_3$  absorption edge (at 938 and 942 eV). These post near edge features strongly depends on the crystal structure as described in paragraph 2.7. The multi-scattering double feature seen in Fig. 5.18 is characteristic for the crystal structure "fcc" of Cu-bulk [59].

Generally, the post-edge features can be explained by multi-scattering of the

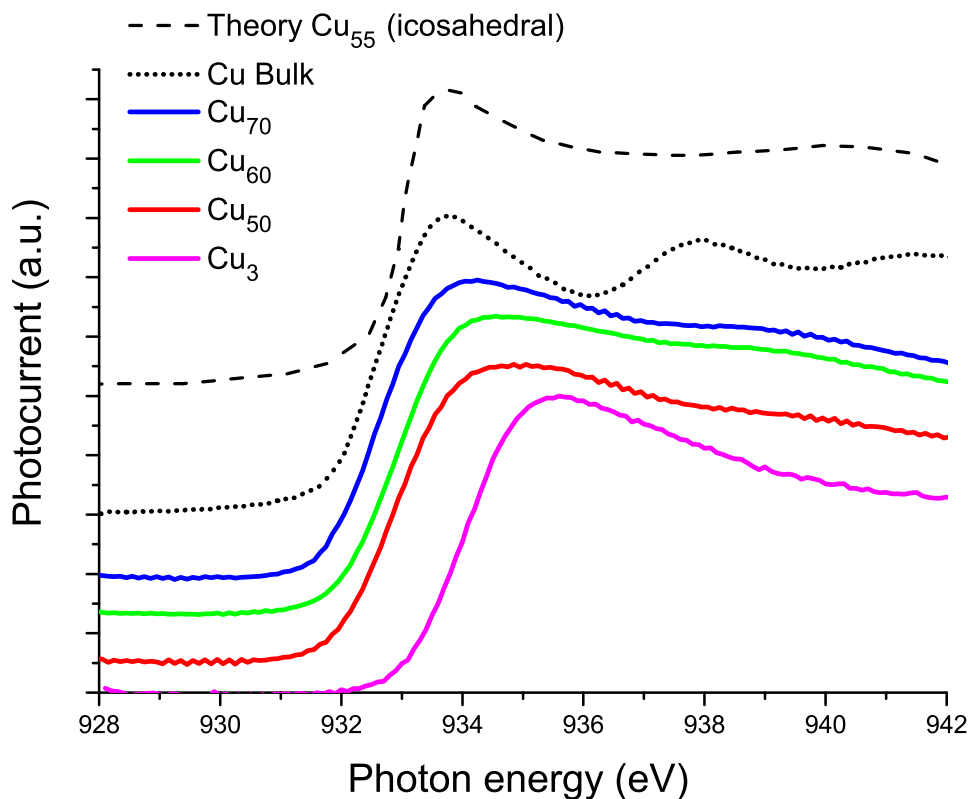


Figure 5.18: XANES of deposited  $Cu_3$ ,  $Cu_{50}$ ,  $Cu_{60}$  and  $Cu_{70}$  in comparison with  $Cu$ -bulk (the simulated spectra of  $Cu_{55}$  in Argon has been reproduced from the PhD thesis of Adam [58]). The spectra of the bigger clusters present a bump at  $\sim 938$  eV. These spectra are closer in appearance to the  $Cu_{55}$  calculated spectrum (icosahedral structure) than to fcc  $Cu$ .

escaping photoelectron and therefore depends on the atomic structure. For very small clusters ( $<10$  atoms) no post-edge feature is observed while a single bump is clearly observed for larger clusters (e.g.  $Cu_{50}$ ,  $Cu_{60}$ ,  $Cu_{70}$ )  $\sim 5$  eV above the  $L_3$  edge. We attribute the multi-scattering feature at  $\sim 939$  eV to a most-likely three dimensional structure of the bigger clusters. Indeed, the single post-edge feature resembles the theoretical calculated spectrum for  $Cu_{55}$  with an icosahedral geometry [58]. For free  $Cu_{60}$  and  $Cu_{70}$  an icosahedral-like five-fold symmetry is predicted while a closed-packed structure is calculated for  $Cu_{50}$  [128]. From the similarity of the spectra of  $Cu_{50}$ ,  $Cu_{60}$  and  $Cu_{70}$  we argue that the five-fold

symmetry of supported  $Cu_{60}$  and  $Cu_{70}$  is kept when the clusters are deposited on the Si-surface and that supported  $Cu_{50}$  has a five-fold symmetry instead of the closed-packed structure predicted for the gas phase ground state geometry.

Fig. 5.19 displays three  $L_3$  absorption spectra of an oxidised  $Cu_{10}$  sample as function of time. The spectra have been taken subsequently, each one for about 20 minutes. The sample was oxidised in air as pure oxygen ( $\sim 1$  Langmuir) did not show any change of the spectrum at room temperature.

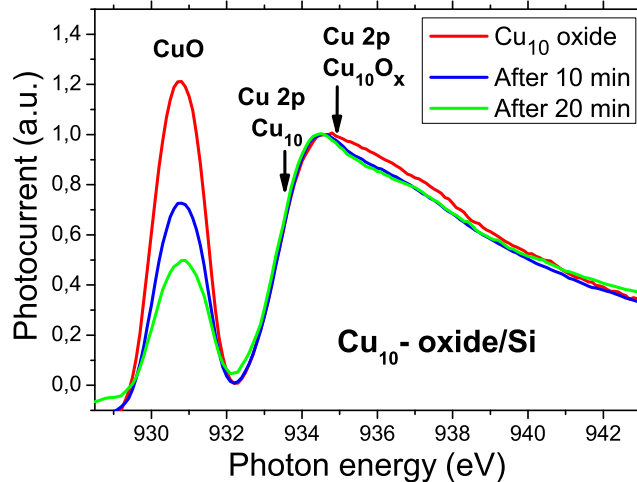


Figure 5.19: X-ray absorption spectra of an oxidised  $Cu_{10}$  sample. The pre-edge feature at 930,8 eV is attributed to the transition from the 2p to an empty 3d orbital with the formation of a "core exciton". This feature appears at lower energy with respect to the XPS threshold which is indicated with an arrow for both pure ( $Cu_{10}$ ) and oxidised copper ( $Cu_{10}O_x$ ). Due to beam photoreduction the low energy peak at 930,8 eV decreases with the exposure time.

With respect to the absorption spectra of the pure cluster a strong pre-edge peak (white line) appears for the oxidised sample at 930,8 eV. The two arrows in Fig. 5.19 indicate the binding energy of the XPS  $2p_{3/2}$  ionisation threshold of pure ( $Cu_{10}$ ) and oxidised  $Cu_{10}$  ( $Cu_{10}O_x$ ). As is clearly evident, the pre-edge peak appears at an energy of  $\sim 4$  eV lower than the XPS threshold of  $Cu_{10}O_x$ . The pre-edge feature is attributed to the excitation of a  $Cu$  2p electron into an empty 3d-orbital of oxidised copper. The narrow "white line" hints at a strongly localised state which implies that the pre-edge feature is not representing the density of states but an excitonic state. Note that with increasing X-ray exposure

time the sample is subject to beam damage, i.e. photoreduction to pristine  $Cu_{10}$  occurs, as the pre-edge peak decreases with time. The pre-edge feature, which is explained by charge transfer from Cu to oxygen is located at a similar energy as in  $CuO$  bulk having a  $Cu^{2+}$  ionic state [62]. Additionally, for  $Cu_{10}O_x$  a positive XPS binding energy shift is observed ( $\sim 1.5$  eV with respect to pristine  $Cu_{10}$ ) due to charge transfer from Cu towards oxygen (initial state effect), i.e.  $Cu3d \rightarrow O2p$ .

Comparing the oxidised cluster spectra of Fig. 5.19 with the spectra of pristine clusters it clearly turns out that our measured clusters are not oxidised. In the absorption spectra of the pure Cu-clusters no excitonic peak appears in front of the XPS threshold that would give evidence to the presence of an open  $d$  shells ( $(Ar)3d^94s^0$ ) as in the  $Cu_{10} - oxide$  case.

Fig. 5.20 shows the  $L_3$  absorption spectra of  $Cu_3$  deposited on a Ag-film.

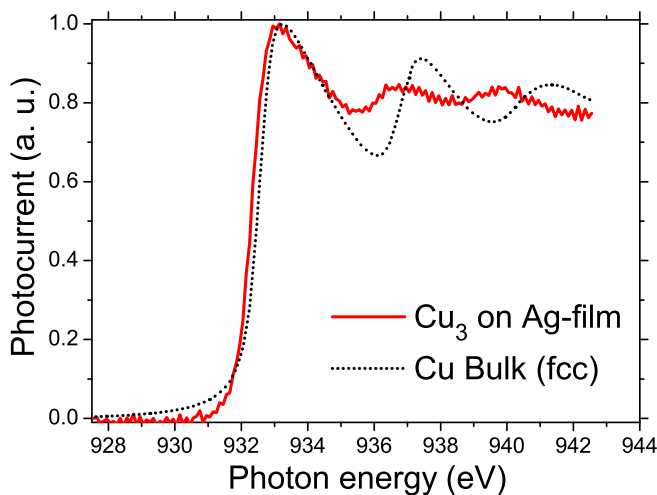


Figure 5.20: *X-ray absorption spectrum of  $Cu_3$  on silver compared with Cu-bulk. The absence of a shift towards higher binding energy and the presence of fine structures similar to the one of the fcc metal indicate the formation of Cu-island on the metal surface.*

This sample has been prepared under the same conditions as used for deposition on Si. The  $Cu_3$  edge does not show any significant shift with respect to the position of the bulk absorption edge. Moreover a double post-edge fine structure is also present for the cluster spectrum. From the very bulk-like spectrum we conclude that  $Cu_3$ -clusters are highly mobile on the Ag surface and that they form *fcc*-islands. The mobility of metal clusters on Ag substrate has also been

observed by Wen *et al.* [3] using a scanning tunneling microscope (STM). They observed that small islands tend to disappear while larger islands grow.

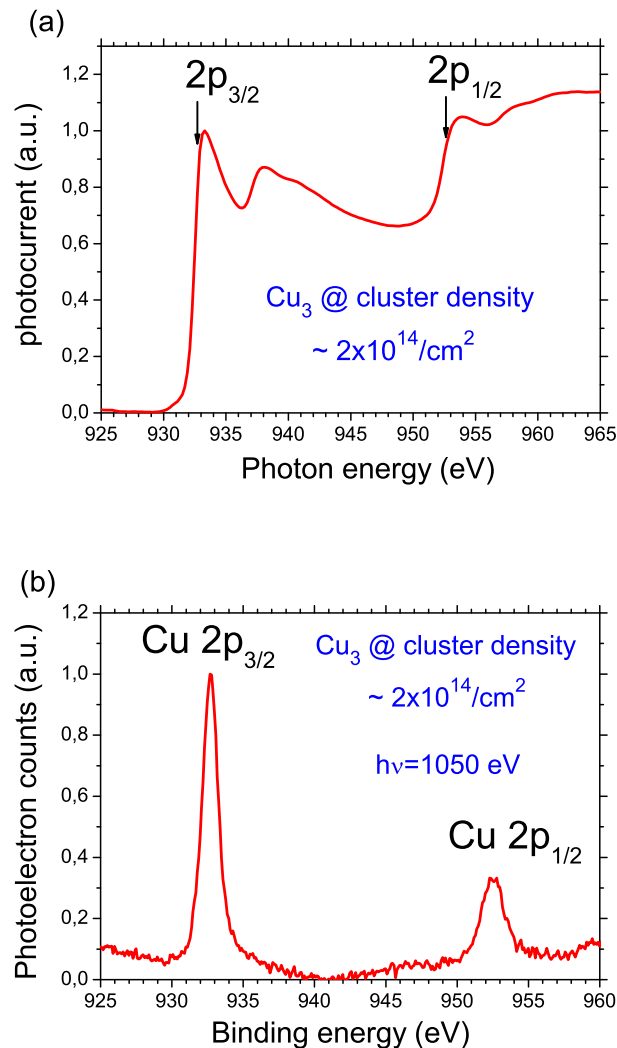


Figure 5.21: XANES (a) and XPS (b) spectra of  $\text{Cu}_3$  on Si at a coverage of  $> 10^{14} \text{ cm}^{-2}$ . The spectra of  $\text{Cu}_3$  resemble that of Cu-bulk for the fcc structure. The arrow in Fig. 5.21 (a) marks the XPS threshold as taken from Fig. 5.21 (b).

In contrast to deposition on Ag, we observe a clear positive X-ray absorption energy shift in the case of cluster deposition on silicon. Moreover the fine structure beyond the absorption edge is absent for small clusters on Si and for bigger sizes the post-edge structure is clearly different with respect to the X-ray absorption

fine structure of *fcc* Cu-bulk. We conclude that on silicon the copper clusters do not agglomerate and that they show individual X-ray absorption spectra which are clearly different from the bulk crystal structure.

### Higher coverage density

Generally, the individual character of the cluster spectra at a cluster coverage of  $\sim 10^{12} - 10^{13} \text{ cm}^{-2}$  verifies that the Cu-clusters were softly landed onto the Si-substrate without fracturing and that the clusters do not agglomerate into islands. This is not the case if a cluster coverage of  $> 10^{14} \text{ cm}^{-2}$  is prepared on Si. In Fig. 5.21 *a*) and *b*) the XPS and XANES spectra of  $\text{Cu}_3$  are shown, respectively. The XANES spectrum of  $\text{Cu}_3$  appears very bulk-like (Fig. 5.21 *a*)) and resembles that of Cu-bulk (see Fig. 2.7). Not only the *L*-edge appears at the same energy as Cu-bulk but also a crystalline-like fine structure [59–61, 129] above the  $L_3$  and  $L_2$  edge appears which is not observed for  $\text{Cu}_3$  at a coverage of  $\approx 10^{12} \text{ cm}^{-2}$  (see Fig. 5.21 *a*)). Furthermore, the  $2p$  core orbital binding energy is identical to the one of Cu-bulk, namely 932,7 and 952,5 eV, respectively. Thus the XANES and XPS spectra in Fig. 5.21 reveal that the clusters on Si agglomerate to islands at a coverage of  $> 10^{14} \text{ cm}^{-2}$  as the X-ray spectra resemble almost perfectly those of the bulk.

### 5.3.2 Band gap approximation

A criterion to study the conductivity of clusters is the analysis of the band gap. Fig. 5.23 shows a single particle energy level diagram for core electronic transition (XPS, XAS) in a metal and cluster. In both the XPS and XAS experiment an electron is ejected from the 2p core level. In XPS the electron is ejected with high kinetic energy into the vacuum (1h final state) while for a XAS transition the excited core electron is bound in an empty state (1h1e final state). For a metal the transitions at threshold are to the unfilled portion of the conduction band lying just above the Fermi level  $\varepsilon_F$ . In the clusters, considered herein all as semiconductors, a band gap  $\Delta E$  occurs between the filled valence and unfilled conduction bands with the Fermi level near the centre of the gap. As typical for semiconductors the core hole is incompletely screened from the excited electron and a core exciton final state may be formed, lowering the excitation energy by  $\Delta_{Exciton}$  [130]. In a rigid band model the "excitonic band gap" can now be estimated with the help of our measured XPS, XAS and UPS data as shown in Fig. 5.23.

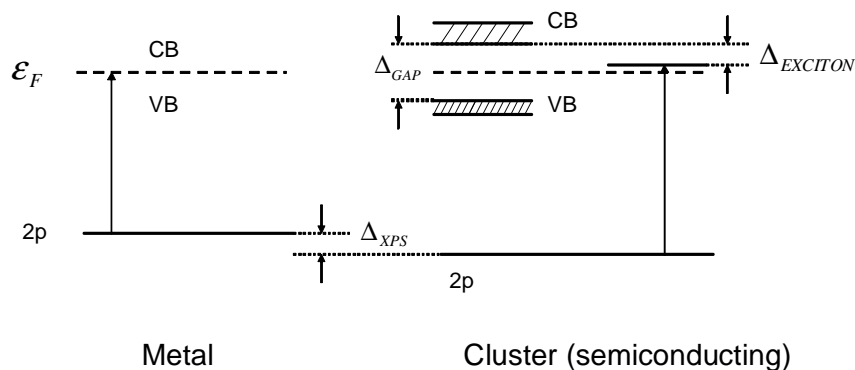


Figure 5.22: *Single particle energy level diagram for core electronic transition (XPS, XAS) in a metal and semiconducting cluster. The diagram shows the relation between ESCA chemical shift  $\Delta_{XPS}$  and the difference in XAS threshold energies between a metal and a semiconducting cluster. The latter depend also on the band gap  $\Delta_{GAP}$  and the core exciton shift  $\Delta_{Exciton}$  [130].*

The distance between the Fermi level and the upper valence band edge is given

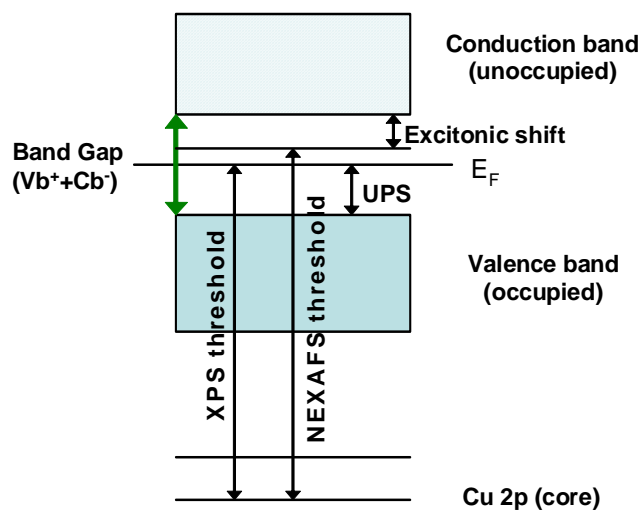


Figure 5.23: *Rigid band model of the band structure of a semiconductor.*

by the difference between the Fermi level and upper 4s-band edge as revealed from UPS. To this difference value we added the difference between the *Cu 2p* binding energy (XPS) and the  $L_3$  threshold energy (XAS) in order to evaluate the "excitonic band gap". Note that the "excitonic band gap" represents the cluster band gap reduced by the excitonic shift.

Fig. 5.24 displays the energy difference between the XAS and XPS data. The XPS and XAS data have been taken from Fig. 5.5 and 5.16. The difference values scatter between -0,5 and +0,5 around  $E_F$ . Positive values (Cluster sizes: 3, 8, 9, 12, 13, 15, 16, 20, 30, 40) show a semiconducting-like energy gap above  $E_F$  while negative values, i.e. excitations to states below  $E_F$ , identifies these excitations as non-density of state features. This can be explained by a localised core exciton which leads to a lowering of the excitation energy in the clusters (2, 5, 6, 7, 10, 11, 14, 21). This excitonic levels is a clear indication of the semiconducting nature of these clusters. The excitonic shift is certainly also the reason that some of the clusters (4, 17, 18, 19, 25, 50, 60, 70) have, within the error bars, a zero gap between  $E_F$  and the conduction band minimum like Cu-metal. However, these clusters are mostly likely not metal-like but should still be considered as semiconductors. The non-metallicity of small Cu-clusters is also confirmed by a post-collision energy shift as recently revealed from photon energy dependent

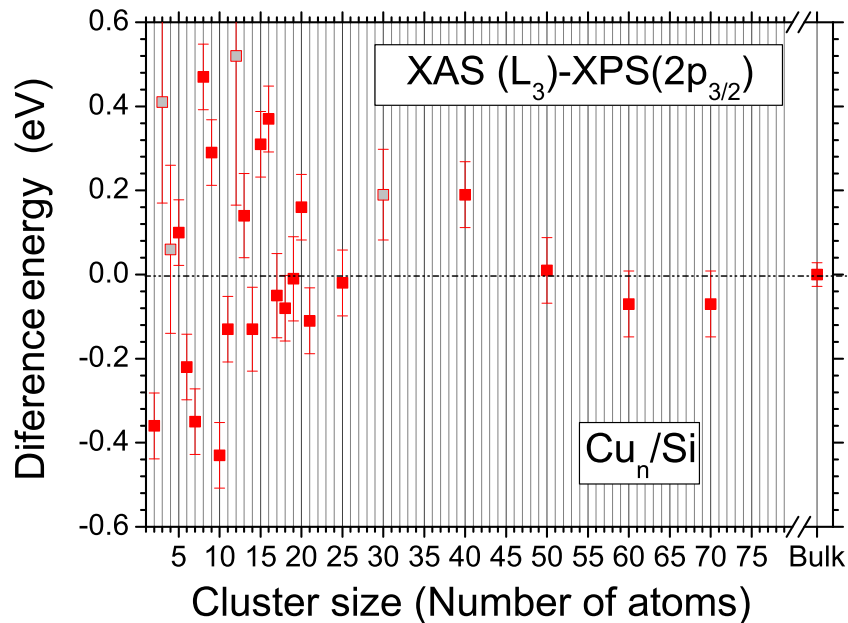


Figure 5.24: Energy difference between the  $L_3$  absorption edge and the  $Cu\ 2p_{3/2}$  binding energy.

Auger measurement [131].

To compare with the HOMO-LUMO gap of free isolated clusters, which have been measured by photodetachment [22,26], the energy gap between the valence band maximum and  $E_F$  has to be added to the difference between the XAS and XPS data (for  $\Delta E > 0$ ). The difference between the valence band maximum and  $E_F$  has been evaluated from the UPS spectra of the clusters. This is exemplarily shown for  $Cu_{40}$  in Fig. 5.25 a) (red). The top of the 4s-valence band of  $Cu_{40}$  is clearly distinguishable from the Si support.  $E_F$  marks the Fermi level of copper bulk. Fig. 5.25 b) shows the difference between the valence band spectrum of  $Cu_{40}$  and Si from which the valence band top has been deduced ("upper VB edge"). The energy of the "upper VB edge" is shown for all other clusters in Fig. 5.26.

Fig. 5.27 compares the band gap of deposited (red) and free Cu-clusters (black, blue) which all show a semiconducting HOMO-LUMO band gap. From the comparison it is obvious that the gap values for the deposited cluster are generally smaller with respect to free clusters. We attribute this band gap low-

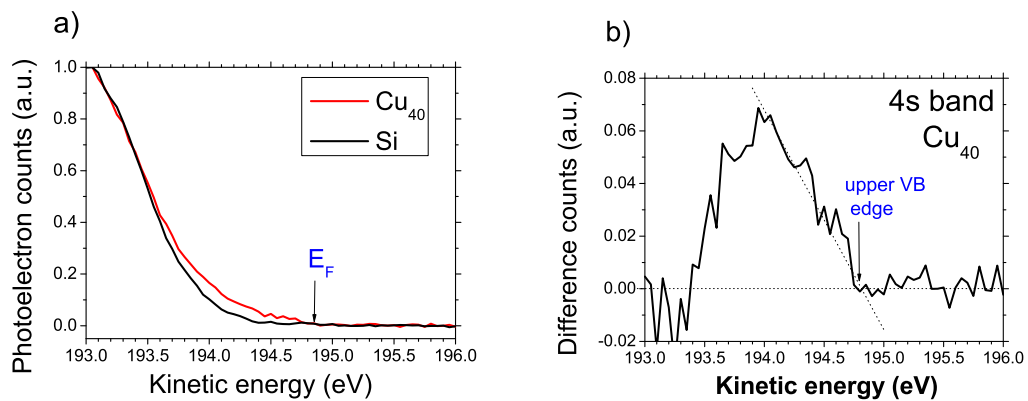


Figure 5.25: a): Upper valence band of  $\text{Cu}_{40}$  and the Si substrate. The Fermi level of Cu-bulk is marked by  $E_F$ . b): Difference between the 4s-“band” onset of  $\text{Cu}_{40}$  and the one of the Si substrate. From this, the top of valence band is deduced.

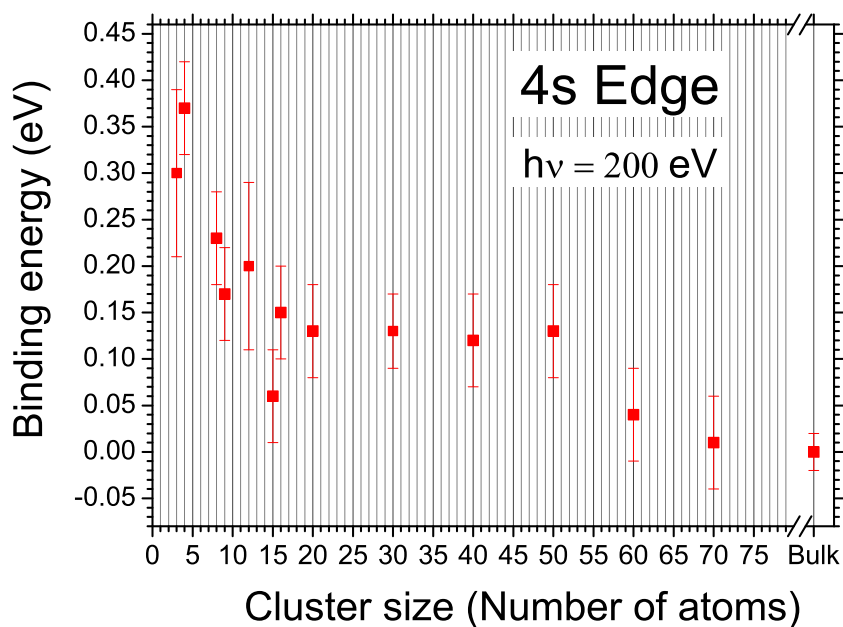


Figure 5.26: Binding energy values of the 4s-valence band top.

ering to the interaction with the substrate and the strong excitonic shift. The trend of the deposited clusters is smooth and converges slowly towards the bulk value with increasing cluster size.  $Cu_8$  does not present a particularly large band gap and the HOMO-LUMO gap of  $Cu_{16}$  is not particularly small as in the free cluster. The band gap of  $Cu_{50}$  is still three time larger then  $2kT$  at room temperature (see paragraph 2.2). Within the error bars the band gap of  $Cu_{60}$  and  $Cu_{70}$  reaches this of Cu bulk. However we believe this to be caused by an excitonic shift rather than by a nonmetal-to-metal transition. As general result we point out that the semiconducting nature of free Cu-clusters is maintained even when the clusters are in contact with a Si-substrate. The HOMO-LUMO gap of the deposited clusters is generally smaller and does not show an even-odd alternation.

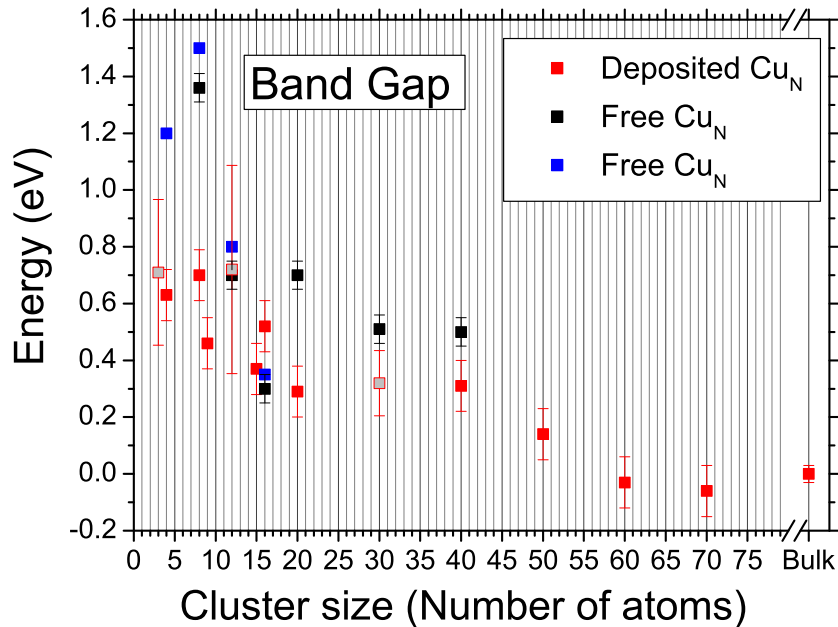


Figure 5.27: Evaluated band gap for deposited Cu clusters on Si (red) and for free Cu clusters from Pettiette et al. [26] (black) and Ganteför et al. [22] (blue). The grey filled squares show the mean value of two distinct measurements on two different samples.

## 5.4 Auger

### 5.4.1 Auger parameter

The binding energy of a particular orbital depends on both initial state and final state effects. The initial state is intrinsically related to the cluster before photoionisation, i.e. it is related to the ground state properties such as electronic structure, geometry, hybridisation, charge transfer, and interaction with the substrate. Final state effects are related to the photoemission event itself, i.e. changes due to ionisation. It includes basically two main phenomena: one is the electrostatic interaction between the photoionised cluster and the outgoing electron. This contribution is for an isolated metallic sphere of radius  $R$  proportional to  $e^2/2R$  [120] (see paragraph 5.2.6) while it should be smaller if the cluster is in electrical contact with a conducting surface. The other effect is the screening ability of the remaining core hole, internally (screening by the ionised atom itself) and externally (screening by the surrounding atoms). In a metal, the final state relaxation term, which lowers the binding energy, arises largely from the screening of the core hole by the conduction electrons. In general the screening should be smaller by both decreasing coordination and decreasing metallicity, e.g. upon size reduction of the clusters. Thus different reasons can account for the observed blue shift of the cluster's binding energy. Photoemission data alone are not sufficient to distinguish between initial and final state effects and the interpretation of the core hole shift is controversial.

Mason *et al.* [89], for example, suggested that the core-level shift is, for any kind of substrate, exclusively due to initial state effects. Similarly, Di Nardo *et al.* [4], who measured Cu clusters on polycrystalline graphite, neglected particle charging and related the different binding energy shift of the core levels,  $3d$  states and Fermi edge to an orbital dependent interaction between Cu and C (initial state). Instead, Wertheim *et al.* [74,120,132] asserted that in the case of metallic clusters supported on a poorly conducting substrate the cluster charge is not necessarily compensated by the substrate. An unscreened charge should remain on the cluster which increases the binding energy of a factor  $e^2/2R$ .

In order to separate between initial and final state effects, we therefore performed Auger measurements to discriminate between both effects by the Auger parameter concept.

The so-called Auger parameter  $\alpha$  [89,120,133,134] is defined as the sum of the binding energy of a particular core level peak and the kinetic energy of the corresponding Auger transition:

$$\alpha = KE + BE \quad (5.10)$$

The Auger parameter has been used as tool to characterise the chemical states of elements in different chemical environments, particularly where sample charging or small binding energy shifts present problems. This use is possible because work function and charging corrections cancel each other during the calculation of  $\Delta\alpha$ . Thus the latter is a direct measure of the energy shift caused by the sum of final state effects such as screening relaxation and final state charging.

The core electron binding-energy shift  $\Delta BE$  measured in a cluster relative to a reference state, typically the bulk material ( $\Delta BE = BE_{cluster} - BE_{bulk}$ ), can be expressed as [120]

$$\Delta BE = \Delta\varepsilon - \Delta E_{final} \quad (5.11)$$

$$\Delta E_{final} = \Delta R - E_{Coul} \quad (5.12)$$

or

$$\Delta BE = \Delta\varepsilon - \Delta R + E_{Coul} \quad (5.13)$$

where  $\Delta\varepsilon$  is the core level chemical shift, i.e. the change in initial-state energy.  $\Delta E_f$  is the final state energy change given by the difference between the change in final-state relaxation energy  $\Delta R$  and Coulomb energy  $E_{Coul}$  [76,120]. This latter term comes from the interaction between the positive charged cluster and the outgoing photoelectron. The Coulomb charging is expected to be dominant on insulating substrates but is minimised on conducting surfaces. The corresponding expression for the shift in Auger kinetic energy,  $\Delta KE$ , is obtained as the difference between the energy of the Auger initial and final state respectively. The initial state of the Auger process is equal to the XPS final state, with the same shift as the core-electron binding energy which is  $\Delta E_{Auger,initial} = \Delta\varepsilon - \Delta R + E_{Coul}$ . The final state is a two-hole state, with energy shift  $\Delta E_{Auger,final} = \Delta\varepsilon_{Auger} - \Delta R_{Auger} + \Delta E_{corr} + 4E_{Coul}$ . Note that both the initial state and relaxation terms of the two-hole Auger final state refer to different orbitals with respect to the photoemission final state, so in this case it is used the subscript "Auger". The Auger relaxation term contains the changes in extra-atomic relaxation (intra atomic relaxation cancels upon calculation of  $\Delta\alpha$ ) for the two-hole final state.  $\Delta E_{corr}$  is the change in the repulsion between the two final-state holes, defined as Coulomb correlation energy. The electrostatic Coulomb energy of a sphere is proportional to the square of number of charges on the cluster, i.e.  $(Ze)^2/2R$  [133]. Therefore

the Coulomb term is four times that of the Auger initial state as in the Auger final two holes appear, i.e.  $Z=2$ . The Auger shift is given by the difference between the initial- and final-state Auger energies, i.e.  $\Delta KE = \Delta E_{Auger,initial} - \Delta E_{Auger,final}$

$$\Delta KE = \Delta\varepsilon - \Delta\varepsilon_{Auger} + \Delta R_{Auger} - \Delta R - \Delta E_{corr} - 3E_{Coul} \quad (5.14)$$

The difference in the Auger parameter for the same element in two distinct chemical states will be given by adding Eqs. 5.13 and 5.14:

$$\Delta\alpha = 2\Delta\varepsilon - \Delta\varepsilon_{Auger} - 2\Delta R + \Delta R_{Auger} - \Delta E_{corr} - 2E_{Coul} \quad (5.15)$$

This formula can be simplified by assuming that  $\Delta\varepsilon_{Auger} \approx 2\Delta\varepsilon$ , that the relaxation energy for a two hole state is four times  $\Delta R$  (from classical electrostatic, the potential energy by a point charge is proportional to the square number of charges), and that effects due to changes in the Coulomb correlation energy are negligible when the delocalisation of the holes in the Auger between cluster and bulk does not change. The equation for  $\Delta\alpha$  then simplifies to [120]

$$\Delta\alpha = \Delta BE + \Delta KE \simeq 2\Delta R - 2E_{Coul}. \quad (5.16)$$

Thus  $\Delta\alpha$  is approximately equal only to final state effects such as the external relaxation and Coulomb charging of the clusters.

Consequently,

$$\frac{\Delta\alpha}{2} = \Delta E_{final} = \Delta R - E_{Coul} \quad (5.17)$$

and the initial state shift is equal to

$$\Delta\varepsilon = \Delta BE + \Delta\alpha/2. \quad (5.18)$$

### 5.4.2 Initial and final state effects

To separate the binding energy shift in initial and final state effects by equation 5.11, the *Cu*  $L_3M_{4,5}M_{4,5}$  Auger spectrum have been recorded at  $\nu=1010$  eV, i.e well above the  $2p_{3/2}$  threshold energy, with an analyser  $E_{pass}$  of 50 eV ( $\Delta E_{kin}=50$  meV). A fully opened exit slit was used for recording this sudden limit Auger spectrum as the monochromator resolution does not effect the Auger line width. The spectra for  $Cu_4$  and  $Cu_{30}$  are shown in Fig. 5.28 in comparison

with the bulk Auger spectrum. The Auger spectrum of Cu-bulk has been interpreted by [119]. The Auger maximum at 914.4 eV corresponds to the  $^1G_4$  Auger final state of Cu-bulk. Common to all clusters is that the measured Auger energy is clearly shifted to smaller kinetic energies by more than 1 eV with respect to the bulk.

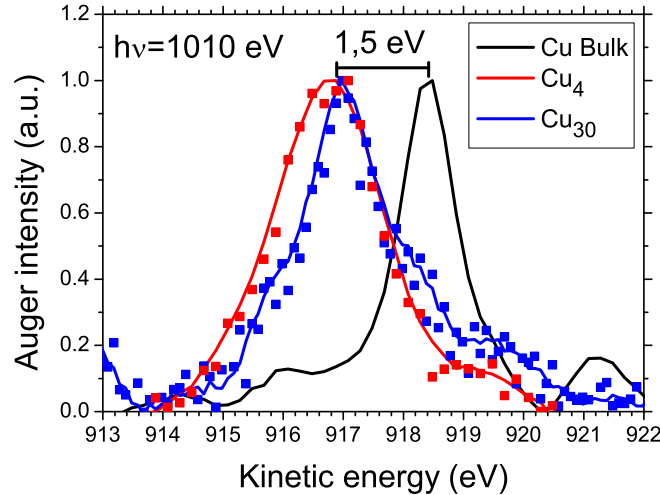


Figure 5.28:  $Cu L_3M_{4,5}M_{4,5}$  Auger spectrum of  $Cu_4$  and  $Cu_{30}$ , respectively, taken at a photon energy of 1010 eV. The dots represent the experimental data while the colored lines results from data smoothing. The Auger spectrum of Cu-bulk is shown as black line.

The net negative shift of the Auger energy directly shows that the 3d valence shift must be larger than 1/2 of the ESCA shift of the core hole as the Auger energy is the difference between the core hole initial and double hole valence final state as shown in Fig. 5.29 (assuming for the moment a negligible shift of the hole-hole interaction energy in the Auger final state, see next paragraph 5.4.3). Thus, within a single particle approximation, the Auger difference between bulk and cluster is given by subtracting the core binding energy shift (initial state shift) from twice the valence energy shift (two-hole final state). For example, for  $Cu_4$  an Auger energy shift of  $0,9 - 2 \times 1,4 \text{ eV} = -1,9 \text{ eV}$  results within the single particle picture and for  $Cu_{30}$  of  $-1,8 \text{ eV}$ . The experimental shift, however, is somewhat smaller which hints to a lowering of the correlation energy in the Auger final state of the supported cluster with respect to the bulk as quantitatively shown in paragraph 5.4.3.

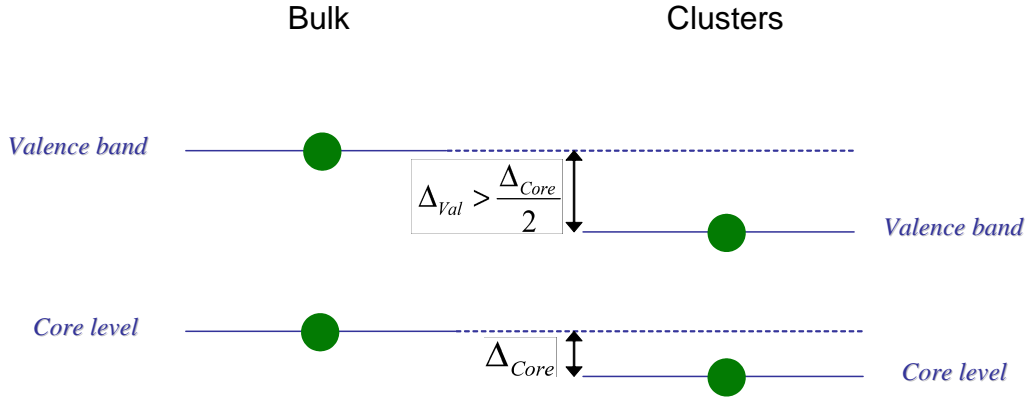


Figure 5.29: Sketch of the relative energy of the core and valence levels for the bulk and clusters. The ESCA shift of the valence levels in clusters is bigger than  $1/2$  the core level ESCA shift. Therefore a red shift of the Auger energy results.

From the XPS peak maximum ( $2p_{3/2}$ ) and the Auger maximum ( $L_3M_{4,5}M_{4,5}$ ), the Auger parameter has been calculated. Using the Auger parameter, the initial ( $\Delta\varepsilon$ ) and final state energy ( $\frac{\Delta\alpha}{2}$ ) are revealed for each cluster as shown in Fig. 5.30. As seen from this figure the predominant contribution to the binding energy shift results from final state effects, i.e. the sum of screening relaxation energy and electron-hole Coulomb interaction. The final state energy is negative for our measured clusters which means that it causes a blue shift of the binding energy. The initial state effects are rather small with respect to the final state effects.

### 5.4.3 Hole-hole interaction in Auger final state

As discussed in the preceding paragraph, the hole-hole interaction within the Auger final state can be approximated by the independently measured Auger, XPS and  $3d$  valence energies. The kinetic energy of the Auger electron  $E_k$  is given by

$$E_k = E_c - E_{v1} - E_{v2} - U(V_1, V_2) \quad (5.19)$$

where  $E_c$ ,  $E_{v1}$ ,  $E_{v2}$  are the binding energy of the  $2p$  and  $3d$  electrons, respectively.  $U(V_1, V_2)$  is the Coulomb interaction of the two holes in the  $3d$  Auger final state. As  $E_k$ ,  $E_c$ ,  $E_{v1}$ ,  $E_{v2}$  have been measured the hole-hole interaction follows straightforwardly from eq. 5.19.

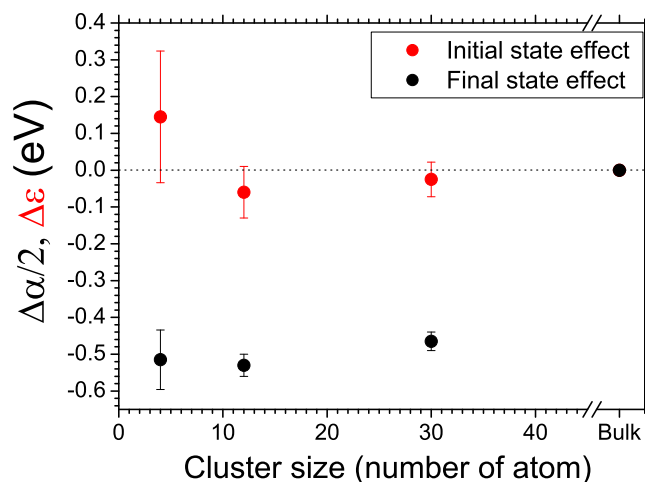


Figure 5.30: *Initial  $\Delta\varepsilon$  (red) and final state (black) energy  $\frac{\Delta\alpha}{2}$  for the clusters  $Cu_4$ ,  $Cu_{12}$ ,  $Cu_{30}$  and  $Cu$ -bulk. The dots represent mean values of two independent measurements. The error bars are derived from error propagation.*

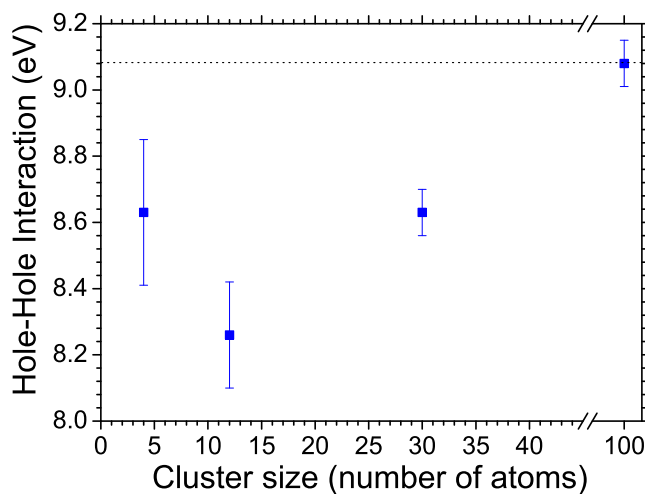


Figure 5.31: *Hole-hole interaction energy between two 3d holes for the clusters  $Cu_4$ ,  $Cu_{12}$ ,  $Cu_{30}$  and  $Cu$ -bulk. The dots represent mean values of two independent measurements. The error bars are derived from error propagation.*

It turns out that  $U(V_1, V_2)$  for copper bulk is 9.1 eV (see Fig. 5.31). This large  $3d$ - $3d$  interaction energy is in reasonable agreement with Sawatzky *et al.* [135] who received a value of 8 eV. This large on-site Coulomb interaction energy indicates a relatively localised  $3d$ -band of Cu. This is directly associated with the completely filled  $d$ -band of Cu in distinct contrast to the preceding  $3d$ -metals such as the itinerant magnetic elements Ni, Co and Fe which have an onsite Coulomb energy of  $<4$  eV [119]. The value of the Cu clusters is similar high as this of the metal. This supports the interpretation made from the NEXAFS spectra that the  $3d$  orbitals of the clusters are completely filled and that electron correlation are expected to be of high importance in Cu clusters, i.e. they might be considered as size-dependent Mott-Hubbard materials. The slightly lower  $U(V_1, V_2)$  values with respect to the bulk as obvious from Fig. 5.31 can be explained by hybridisation with substrate orbitals which leads to a slightly smaller localisation of the  $3d$  orbitals with respect to Cu-bulk.



# Chapter 6

## Summary and outlook

In this work a systematic study of X-ray photoionisation spectroscopy on mass selected supported clusters has been performed. To study the development of the electronic structure with cluster size and to get informations on the geometry of the clusters a combination of X-ray photoelectron (XPS, UPS), X-ray absorption (XANES) and Auger electron spectroscopy has been used.

An existing cluster beam machine has been updated and heavily improved in order to perform a high cluster output for a non destructive deposition of mass selected clusters. With this machine copper cluster ions up to 70 atoms have been softly deposited on a silicon substrate at low ion kinetic energy. Inserting new electrostatic focusing lenses and an ion current monitor, a cluster coverage density of  $10^{12} - 10^{13} \text{ cm}^{-2}$  has been reached in a reasonable time, which allowed synchrotron X-ray studies on individual, non agglomerated supported metal clusters.

With XPS and UPS the core levels  $2p$  and  $3p$  as well as the  $3d$  have been investigated at a low cluster coverage density ( $< 10^{13}/\text{cm}^2$ ). For all clusters a blue shift and a continuous trend towards the bulk value with increasing cluster size has been observed.

The measured binding energies at low coverage density have been compared with the binding energies deduced from the liquid drop model as function of  $1/R$ . A clear size dependence is observed. The  $3d$  valence band fits rather well to the model except for very small cluster sizes ( $\leq 13$  atoms). Instead, the  $2p$  and  $3p$  core levels show a significantly lower binding energy ( $\sim 1,4 \text{ eV}$ ) with respect to the liquid drop model which is explained by strong core hole screening and the interaction with the substrate. The decreasing blue shift of the XPS binding energy with cluster size is attributed to arise mainly from final state effects according to an analysis of the Auger parameter concept.

The XANES spectrum shows that the  $L$ -shell absorption edges of the Cu clus-

ters are blue shifted with respect to the bulk. The characteristic multi-scattering fine structure beyond the  $L$  edge of  $fcc$  Cu-bulk does not show up in any cluster spectrum. Instead, some clusters (e.g.  $Cu_{50}$ ,  $Cu_{60}$ ,  $Cu_{70}$ ) reveal a single bump  $\sim 5$  eV beyond the absorption edge. This fine structure might indicate an icosahedral symmetry. The absorption spectrum of an oxidised cluster sample appears to be significantly different to the spectra of the pristine deposited clusters. The pre-edge excitonic "white line" of oxidised  $Cu_{10}$  indicates the presence of an open  $d$  shell due to oxidation.

The HOMO-LUMO band gap has been approximated for some clusters in a rigid band model by combining XPS, XANES and UPS data. Excitonic levels indicate a semiconducting nature of the deposited clusters. In contrast to the gas phase the band gap does not show even-odd alternation and magic cluster behaviour. Even for  $Cu_{70}$  the evaluated gap is still larger than the Kubo gap at room temperature, indicating that all analysed clusters are semiconducting.

The kinetic energy of the  $LMM$  Auger electron shows a red shift with respect to the bulk value. This is in agreement with the fact that the measured  $Cu$   $3d$  shift is bigger than half the  $Cu$   $2p$  shift. The Coulomb interaction within the Auger final state has been evaluated by the measured Auger kinetic energy and  $Cu$   $2p$  and  $3d$  binding energies. The experimentally derived value of  $\sim 8$  eV indicates that the  $3d$  orbitals of the clusters are rather localised and completely filled. With respect to the bulk the Coulomb correlation is somewhat weakened.

As outlook bigger clusters should be studied, i.e. up to 200 atoms. An important aim is to detect the change from semiconductors to metallic behaviour of the copper clusters by photon dependent Auger spectra. Of particular interest is the measurement of copper clusters deposited on a less interacting material (e.g.  $MgO$ ,  $SiO_2$ ), in order to compare the influence of the binding energy by the substrate. The chemical reactivity of the deposited copper clusters as a function of cluster size, as for example the chemical reactivity towards  $O_2$ ,  $H_2O$  and  $N_2$  should be studied to see the stability against ambient air compounds. EXAFS study at the Cu K-shell would be of particular interest to receive informations on the internuclear Cu-Cu distances of the clusters.

# Bibliography

- [1] R. P. Feynman. *Eng. Sci.* **23**, 22 (1960)
- [2] C. M. Whelan, C. J. Barnes. *Appl. Surf. Sci.* **119**, 288 (1997)
- [3] J. M. Wen, S. L. Chang, J. W. Burnett, J. W. Evans, P. A. Thiel. *Phys. Rev. Lett.* **73**, 2591 (1994)
- [4] S. D. Nardo, L. Lozzi, M. Passacantando, P. Picozzi, S. Santucci, M. D. Crescenzi. *Surf. Sci.* **307-309**, 922 (1994)
- [5] W. F. Egelhoff, Jr., G. G. Tibbetts. *Solid State Commun.* **29**, 53 (1979)
- [6] V. Vijayakrishnan, C. Rao. *Surf. Sci. Lett.* **255**, L516 (1991)
- [7] R. E. Palmer, S. Pratontep, H. G. Boyen. *Nature Materials* **2**, 443 (2003)
- [8] S. B. DiCenzo, S. D. Berry, J. E. H. Hartford. *Phys. Rev. B.* **38**, 8465 (1988)
- [9] H. Yasumatsu, T. Hayakawa, S. Koizumi, T. Kondow. *J. Chem. Phys.* **123**, 124709 (2005)
- [10] H.-V. Roy, P. Fayet, F. Patthey, W.-D. Schneider, B. Delley, C. Mossobrio. *Phys. Rev. B* **49**, 5611 (1994)
- [11] P. Fayet, F. Granzer, G. Hegenbart, E. Moisar, B. Pischel, L. Wöste. *Phys. Rev. Lett.* **55**, 3002 (1985)
- [12] U. Heiz, F. Vanolli, L. Trento, W. D. Schneider. *Rev. Sci. Instrum.* **68**, 1986 (1997)
- [13] W. D. Knight, K. Clemenger, W. A. de Heer, W. A. Saunders, M. Y. Chou, M. L. Cohen. *Phys. Rev. Lett.* **52**, 2141 (1984)
- [14] W. A. de Heer. *Rev. Mod. Phys.* **65**, 611 (1993)

- [15] W. Ekard. Phys. Rev. B **29**, 1558 (1984)
- [16] P. S. Bechthold, M. Neeb. *Vorlesungsmanuskripte - Physik der Nanostrukturen*. Forschungszentrum Juelich (1998)
- [17] K. J. Taylor, C. L. Pettiette-Hall, O. Cheshnovsky, R. E. Smalley. J. Chem. Phys. **96**, 3319 (1992)
- [18] C. Cha, G. Ganteför, W. Eberhardt. J. Chem. Phys. **99**, 6308 (1993)
- [19] J. Morenzin, H. Kietzmann, P. S. Bechtold, G. Ganteför, W. Eberhardt. Pure Appl. Chem. **72**, 2149 (2000)
- [20] O. Kostko, N. Morgner, M. A. Hoffmann, B. von Issendorff. Eur. Phys. J. D **34**, 133 (2005)
- [21] H. Kietzmann, J. Morenzin, P. S. Bechthold, G. Ganteför, W. Eberhardt. Phys. Rev. Lett. **77**, 4528 (1996)
- [22] G. Ganteför, C.-Y. Cha, H. Handschuh, G. S. Icking-Konert, B. Kessler, O. Gunnarsson, W. Eberhardt. J. Electr. Spectr. Rel. Phenom. **76**, 37 (1995)
- [23] H. Fröhlich. Physica **4**, 406 (1937)
- [24] R. Kubo. J. Phys. Soc. Jpn. **17**, 975 (1962)
- [25] R. L. Johnston. Phil. Trans. R. Soc. Lond. A **356**, 211 (1998)
- [26] C. L. Pettiette, S. H. Yang, M. J. Craycraft, J. Conceicao, R. T. Laaksonen, O. Cheshnovsky, R. E. Smalley. J. Chem. Phys. **88**, 5377 (1988)
- [27] J. Jortner. Z. Phys. D **24**, 247 (1992)
- [28] S. Halas. Chem. Phys. Lett. **370**, 300 (2003)
- [29] G. Makov, A. Nitzan, L. E. Brus. J. Chem. Phys. **88**, 5076 (1988)
- [30] G. Makov, A. Nitzan. J. Chem. Phys. **95**, 9024 (1991)
- [31] K. H. M. Broer. *Metal Clusters at Surfaces*. Springer (2000)
- [32] A. Antonelli, S. N. Khanna, P. Jena. Phys. Rev. B **48**, 8263 (1993)
- [33] *Atomic and molecular clusters*. Taylor and Francis (2002)

- [34] G. Pacchioni, N. Lopez, F. Illas. *Faraday Discuss.* **114**, 209 (1999)
- [35] M. Adam. *Spectroscopic investigation of deposited InP nanocrystals and small Cu clusters*. Ph.D. thesis, Universität Hamburg (2004)
- [36] H. Hsieh, R. S. Averback, H. Sellers, C. P. Flynn. *Phys. Rev. B* **45**, 4417 (1992)
- [37] J. Li, X. Li, H.-J. Zhai, L. Wang. *Science* **299**, 864 (2003)
- [38] H. Häkkinen, B. Yoon, U. Landmann, X. Li, H.-J. Zhai, L.-S. Wang. *J. Phys. Chem. A* **107**, 6168 (2003)
- [39] A. Sanchez, S. Abbet, U. Heiz, W. Schneider, H. Häkkinen, R. Barnett, U. Landmann. *J. Phys. Chem. A* **103**, 9573 (1999)
- [40] L. Peyser, A. Vinson, A. Bartko, R. Dickson. *Science* **291**, 103 (2001)
- [41] R. W. Mayer, M. Melzer, M. Hävecker, A. Knop-Gericke, J. Urban, H. J. Freund, R. Schlögl. *Cat. Lett.* **86**, 245 (2003)
- [42] K. Judai, S. Abbet, A. S. Wörz, A. M. Ferrari, L. Giordano, G. Pacchioni, U. Heiz. *J. Mol. Cat. A* **199**, 103 (2003)
- [43] G. Guvelioglu, P. Ma, X. He, R. Forrey, H. Cheng. *Phys. Rev. Lett.* **94**, 026103 (2005)
- [44] O. Cheshnovsky, K. Taylor, J. Conceicao, R. Smalley. *Phys. Rev. Lett.* **64**, 1785 (1990)
- [45] P. Calaminici, A. M. Köster, N. Russo, D. R. Salahub. *J. Chem. Phys.* **105**, 9546 (1996)
- [46] C. Massobrio, A. Pasquarello, A. dal Corso. *J. Chem. Phys.* **109**, 6626 (1998)
- [47] K. Jug, B. Zimmermann, P. Calaminici, A. M. Köster. *J. Chem. Phys.* **116**, 4497 (2002)
- [48] M. Kabir, A. Mookerjee, A. K. Bhattacharya. *Phys. Rev. A* **69**, 43203 (2004)
- [49] M. O. Aboelfotoh, B. G. Svensson. *Semicond. Sci. Technol.* **6**, 647 (1991)

- [50] N. Benouattas, A. Mosser, D. Raiser, J. Faerber, A. Bouabellou. Appl. Surf. Sci. **153**, 79 (2000)
- [51] L. Magagnin, R. Maboudian, C. Carraro. Thin Solid Films **434**, 100 (2003)
- [52] M. D. Upward, B. N. Cotier, P. Moriarty, P. H. Beton, S. H. Baker, C. Binns, K. Edmonds. J. Vac. Sci. Technol. B **18**, 2646 (2000)
- [53] M. D. Upward, P. Moriarty, P. H. Beton, S. H. Baker, C. Binns, K. Edmonds. Appl. Phys. Lett. **70**, 2114 (1997)
- [54] M. Grioni, J. Goedkoop, R. Schoorl, F. de Groot, J. Fuggle, F. Schäfers, E. Koch, G. Rossi, J. M. Esteva, R. Karnatak. Phys. Rev. B **39**, 1541 (1989)
- [55] M. Hirsimäki, M. Lampimäki, K. Lahtonen, I. Chorkendorff, M. Valden. Surf. Sci. **583**, 157 (2005)
- [56] M. Escher, N. Weber, M. Merkel, B. Krömker, D. Funnemann, S. Schmidt, F. Reinert, F. Forster, S. Hüfner, P. Berndard, C. Ziethen, H. Elmers, G. Schönhense. J. Electron Spectrosc. Relat. Phenom. **144**, 1179 (2005)
- [57] U. Arp, K. Iemura, G. Kutluk, M. Meyer, T. Nagata, M. Sacchi, B. Sonntag, S. Yagi, A. Yagishita. J. Phys. B **27**, 3389 (1994)
- [58] M. S. Adam. *Spectroscopic investigation of deposited InP nanocrystals and small Cu clusters*. Ph.D. thesis, Universitaet Hamburg (2004)
- [59] H. Ebert, J. Stöhr, S. S. P. Parkin, M. Samant, A. Nilsson. Phys. Rev. B **53**, 16067 (1996)
- [60] T. Tiedje, J. R. Dahn, Y. Gao, K. M. Colbow, E. D. Crozier, D. T. Jiang, W. Eberhardt. Solid State Commun. **85**, 161 (1993)
- [61] S. I. Zabinsky, J. J. Rehr, A. Ankudinov, R. C. Albers, M. J. Eller. Phys. Rev. B **52**, 2995 (1995)
- [62] M. Grioni, J. F. van Acker, M. T. Czyzyk, J. C. Fuggle. Phys. Rev. B **45**, 3309 (1992)
- [63] A. Knop, B. Wassermann, E. Rühl. Physical Review Letters **80**, 2302 (1998)
- [64] O. Bjoernehlm, F. Federmann, F. Fössig, T. Moeller. Phys. Rev. Lett. **744**, 3017 (1995)

- [65] F. Federmann, O. Björneholm, A. Beutler, T. Möller. *Phys. Rev. Lett.* **73**, 1549 (1994)
- [66] R. Feifel, M. Tchapyguine, G. Öhrwall, M. Salonen, M. Lundwall, R. R. T. Marinho, M. Gisselbrecht, S. L. Sorensen, A. N. de Brito, L. Karlsson, N. Martensson, S. Svensson, O. Björneholm. *Eur. Phys. J. D* **30**, 343 (2004)
- [67] M. Tchapyguine, R. Feifel, R. R. T. Marinho, M. Gisselbrecht, S. L. Sorensen, A. N. de Brito, N. Martensson, S. Svensson, O. Björneholm. *Chem. Phys.* **289**, 3 (2003)
- [68] P. Piseri, T. Mazza, G. Bongiorno, C. Lenardi, L. Ravagnan, F. della Foglia, F. diFonzo, M. Coreno, M. D. Simone, K. C. Prince, P. Milani. *New J. Phys.* **8**, 136 (2006)
- [69] J. T. Lau, J. Rittmann, V. Zamudio-Bayer, M. Vogel, K. Hirsch, P. Klar, F. Lofink, T. Möller, B. v. Issendorf. *submitted to Phys. Rev. Lett.*
- [70] M. G. Mason, L. J. Gerenser, S. T. Lee. *Phys. Rev. Lett* **39**, 288 (1977)
- [71] M. D. Crescenzi, M. Diociaiuti, L. Lozzi, P. Picozzi, S. Santucci. *Solid State Commun.* **74**, 115 (1988)
- [72] S. Andersson, P. A. Brühwiler, A. Sandell, M. Frank, J. Libuda, A. Giertz, B. Brena, A. J. Maxwell, M. Bäumer, H.-J. Freund, N. Martensson. *Surf. Sci.* **442**, L964 (1999)
- [73] Z. Pászti, G. Petö, Z. E. Horváth, A. Karacs, L. Guzzi. *J. Phys. Chem. B* **101**, 2109 (1997)
- [74] G. K. Wertheim, S. B. DiCenzo, S. E. Youngquist. *Phys. Rev. Lett.* **51**, 2310 (1983)
- [75] W. Eberhardt, P. Fayet, D. M. Cox, Z. Fu, A. Kaldor, R. Sherwood, D. Sondericker. *Phys. Rev. Lett.* **64**, 780 (1990)
- [76] I. Jirka. *Surf. Sci.* **232**, 307 (1990)
- [77] P. Montano, G. K. Shenoy, E. E. Alp. *Phys. Rev. Lett.* **56**, 2079 (1986)
- [78] J. O'Shea, J. Schnadt, S. Andersson, L. Patthey, S. Rost, A. Giertz, B. Brena, J.-O. Forsell, A. Sandell, O. Björneholm, P. A. Brühwiler, N. Martensson. *J. Chem. Phys.* **113**, 9233 (2000)

- [79] H. R. Siekmann, B. Wrenger, E. Holub-Krappe, C. Pettenkofer, K. H. Meiwes-Broer. Supplement to Z. Phys. D. **26**, 54 (1993)
- [80] D. C. Lim, R. Dietsche, M. Bubek, G. Ganteför, Y. D. Kim. Chem. Phys. Chem. **7**, 1909 (2006)
- [81] D. C. Lim, R. Dietsche, M. Bubek, T. Ketterer, G. Ganteför, Y. D. Kim. Chem. Phys. Lett. **439**, 364 (2007)
- [82] J. T. Lau, W. Wurth, H. U. Ehrke, A. Achleitner. Low Temp. Phys. **29**, 223 (2003)
- [83] J. T. Lau, A. Föhlisch, R. Nietubyc, M. Reif, W. Wurth. Phys. Rev. Lett. **89**, 057201 (2002)
- [84] W. F. Egelhoff, Jr., G. G. Tibbetts. Phys. Rev. B **19**, 5028 (1979)
- [85] D. Q. Yang, E. Sacher. Appl. Surf. Sci. **195**, 187 (2002)
- [86] X. C. Lai, M. A. Pushkin, V. I. Troyan. Surf. Interface Anal. **36**, 1199 (2004)
- [87] V. Senz, P. Oelßner, J. Tiggesbäumer, K.-H. Meiweis-Broer, T. Fischer, G. Ganteför, J. Stanzel, M. Neeb, W. Eberhardt, C. Bostedt, H. Thomas, T. Möller, M. Schöffler, R. Dörner, H. Schmidt-Böcking, M. Martins, W. Wurth, J. Neville, E. Rühl, R. Treusch, P. Radcliffe. To be published
- [88] K. Siegbahn, C. N. Nordling, A. Fahlman, R. Nordberg, K. Hamrin, J. hedman, G. Johansson, T. Bermark, S. E. Karlsson, I. Lindgren, B. Lindberg. *ESCA: atomic, Molecular and Solid State Strucrure Studied by means of Electron Spectroscopy*. Almqvist and Wiksells, Uppsala (1967)
- [89] M. G. Mason. Phys. Rev. B **27**, 748 (1983)
- [90] F. Parmigiani, E. Kay, P. S. Bagus, C. J. Nelin. J. of electron spectrosc. and relat. Phenom. **36**, 257 (1985)
- [91] H. Haberland. *Clusters of Atoms and Molecules II*. Springer-Verlag
- [92] K. Siegbahn, *et al.* *Nova Acta Regiae Soc. Sci. Upsal., Ser. IV 20* (1967)
- [93] H. Hertz. Ann. Physik **31**, 983 (1887)
- [94] A. Einstein. Ann. Phys. **17**, 132 (1905)

- [95] T. A. Carlson. *Photoelectron and Auger Spectroscopy*. Plenum Press, New York (1975)
- [96] E. E. Koch. *Handbook of Synchrotron Radiation, Vol I*. North-Holland Publishing Company (1983)
- [97] D. Briggs, M. P. Seah. *Practical Surface Analysis*. John Wiley and Sons (1983)
- [98] D. P. Woodruff, T. A. Delchar. *Modern techniques of surface science..* Cambridge University Press (1994)
- [99] J. J. Rehr, R. C. Albers. *Rev. Mod. Phys.* **72**, 621 (2000)
- [100] <http://de.wikipedia.org/wiki/NEXAFS>
- [101] *X-ray Absorption Near Edge Spectroscopy*. American Scientific Publishers (2004)
- [102] H. A. Kramers, W. Heisenberg. *Z. Phys.* **31**, 681 (1925)
- [103] R. Klingeler, P. S. Bechthold, M. Neeb, W. Eberhardt. *Rev. Sci. Inst.* **31**, 1803 (2002)
- [104] B. Balkaya. *Aufbau einer Magnetronclusterquelle*. Master's thesis, Technische Universität Berlin + BESSY mbH (2005)
- [105] H. Haberland, M. Mall, M. Moseler, Y. Qiang, T. Reiners, Y. Thurner. *J. Vac. Sci. Technol. A* **12**, 2925 (1994)
- [106] <http://www.soleras.com/magntrn/enhance.htm>
- [107] H. Haberland, M. K. M. Mall, Y. Thurner. *J. Vac. Sci. Technol. A* **10**, 3266 (1992)
- [108] P. Milani, S. Iannotta. *Cluster Beam Synthesis of Nanostructured Materials*. Springer (1999)
- [109] H. Hensel, P. Klein, H. M. Urbassek, T. Frauenheim. *Phys. Rev. B* **53**, 16497 (1996)
- [110] *Constructed by A. Vollmer*
- [111] Manual. *SCIENTA SES 100 Electron spectrometer* (2002)
- [112] M. P. Seah, W. A. Dench. *Surface and interface analysis* **1**, 2 (1979)

- [113] *Photoemission in solids I: general Principles*. Springer-Verlag, Berlin (1978)
- [114] <http://www.webelements.com/webelements/elements/text/Si/bind.html>
- [115] F. J. Himpsel, F. R. McFeely, A. Taleb-Ibrahimi, J. A. Yarmoff. *Phys. Rev. B* **38**, 6084 (1988)
- [116] G. Comtet, K. Bobrov, L. Hellner, G. Dujardin. *Phys. Rev. B* **69**, 155315 (2004)
- [117] V. P. Zakaznova-Herzog, H. W. Nesbitt, G. M. Bancroft, J. S. Tse, X. Gao, W. Skinner. *Phys. Rev. B* **72**, 205113 (2005)
- [118] J. C. Fuggle, N. Martensson. *J. Electron Spectrosc. Relat. Phenom.* **21**, 275 (1980)
- [119] E. Antonides, E. C. Janse, G. A. Sawatzky. *Phys. Rev. B* **15**, 4596 (1977)
- [120] G. K. Wertheim. *Phys. Rev. B* **36**, 9559 (1987)
- [121] M. Sancrotti, M. Sacchi, O. Sakho, G. Rossi. *Phys. Rev. B* **44**, 1958 (1991)
- [122] A. T. et al. *X-ray data booklet*. Lawrence Berkeley National Laboratory (2001)
- [123] B. von Issendorff, O. Cheshnovsky. *Annu. Rev. Phys. Chem.* **56**, 549 (2005)
- [124] C. Bréchnignac, P. Cahuzac, F. Carlier, J. Leygnier. *Phys. Rev. Lett.* **63**, 1368 (1989)
- [125] D. M. Wood. *Phys. Rev. Lett.* **46**, 749 (1981)
- [126] H. Yamauchi. *Phys. Rev. B* **31**, 7688 (1985)
- [127] S. S. Lee, J. H. Kim, S. C. Wi, G. Kim, J. S. Kang, Y. J. Shin, S. W. Han, K. H. Kim, H. J. Song, H. J. Shin. *J. Appl. Phys.* **97**, 10A309 (2005)
- [128] J. P. K. Doye, D. J. Wales. *New J. Chem.* 733 (1998)
- [129] A. I. Nesvizhskii, J. J. Rehr. *J. Synchr. Rad.* **6**, 315 (1999)
- [130] R. D. Leapman, L. A. Grunes, P. Fejes. *Phys. Rev. B* **26**, 614 (1982)
- [131] B. Balkaya, N. Ferretti, M. Neeb., W. Eberhardt. Submitted

- 
- [132] G. K. Wertheim, S. B. DiCenzo. *Phys. Rev. B* **37**, 844 (1988)
- [133] C. D. Wagner. *Faraday Discuss. Chem. Soc.* **60**, 291 (1975)
- [134] T. D. Thomas. *J. Electron Spectrosc. Relat. Phenom.* **20**, 117 (1980)
- [135] G. A. Sawatzky, E. Antonides. *J. Phys. (Paris) Suppl.* **37**, c4 (1976)



# Appendix A

## List of publications

1. N. Ferretti, B. Balkaya, A. Vollmer, M. Neeb, W. Eberhardt, *Inner-shell photoelectron spectroscopy of size-selected Cu-clusters on Si*, Journal of Electron Spectroscopy and Related Phenomena 156-158 (2007) 124, proceedings of Int. Conference on Electronic Spectroscopy and Structure ICES 10.
2. B. Balkaya, N. Ferretti, M. Neeb. W. Eberhardt *PCI in supported Cu clusters as proof of non-metallicity of deposited Cu clusters*, submitted to Phys. Rev. Lett..
3. N. Ferretti, B. Balkaya, M. Neeb. W. Eberhardt *X-ray spectroscopy on mass-selected supported Cu-clusters on Si*, in preparation.
4. F. Boscherini, N. Ferretti, B. Bonanni, D. Orani, S. Rubini, M. Piccin, and A. Franciosi *Silicon clustering in Si-GaAs -doped layers and superlattices*, Applied Physics Letters 81 (2002) 1639.
5. S. Spiga, R. Mantovan, M. Fanciulli, N. Ferretti, F. Boscherini, F. D'Acapito, and B. Schmidt, *Formation and local structure of Sn and Sb nanoclusters in thin SiO<sub>2</sub> films*, Nuclear Instrum. Methods B 200 (2003) 171, proceedings of E-MRS Spring Meeting 2002.
6. S. Spiga, R. Mantovan, M. Fanciulli, N. Ferretti, F. Boscherini, and F. D'Acapito, , *Formation and local structure of Sn and Sb nanoclusters in thin SiO<sub>2</sub> films: X-ray absorption, Moessbauer spectroscopy and electron microscopy*, Physical Review B.